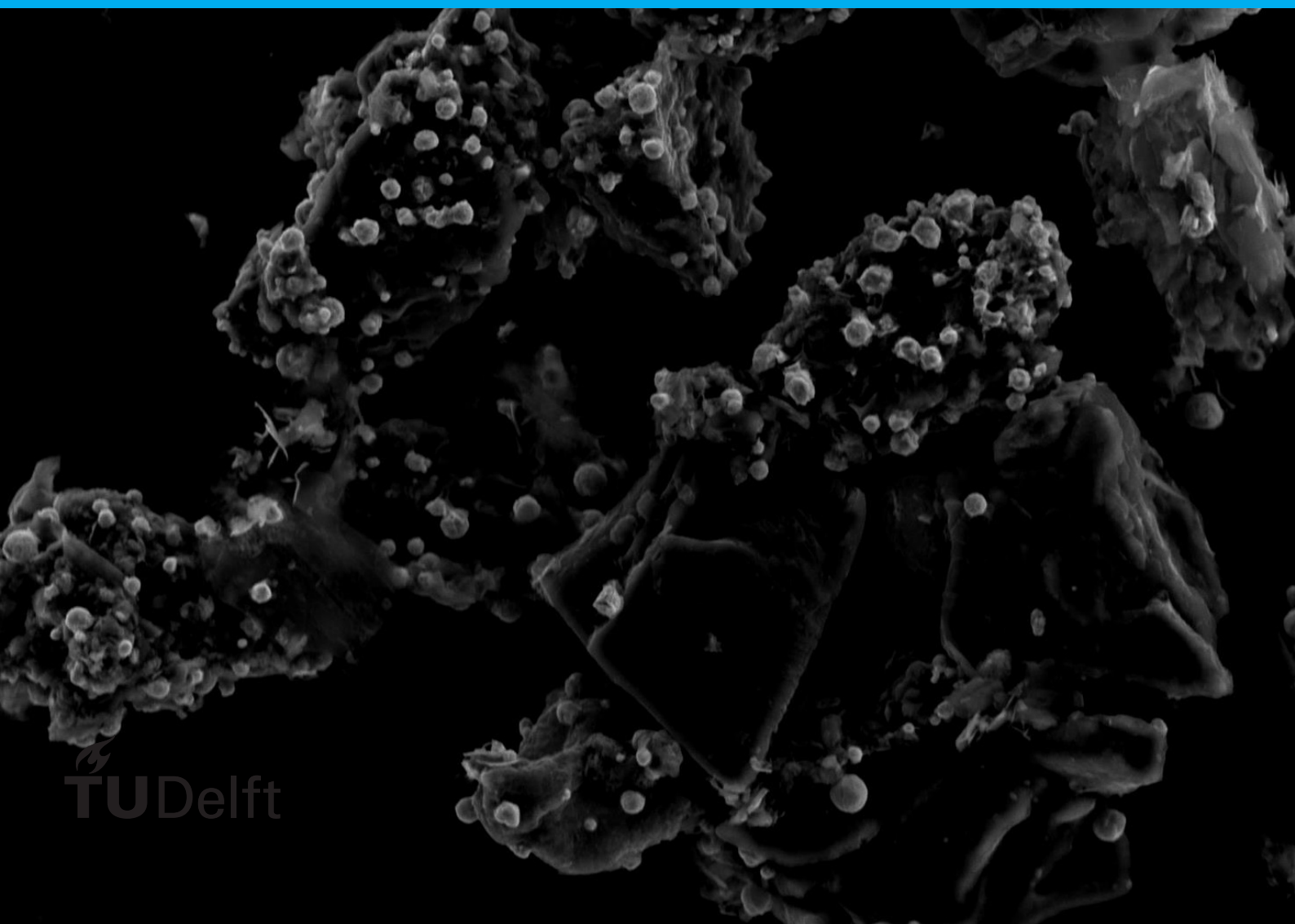


Carbonization of 3D- and 2D-
MOFs for electrochemical carbon
dioxide reduction.

J. Coppen



Carbonization of 3D- and 2D-MOFs for electrochemical carbon dioxide reduction.

by

J. Coppen

to obtain the degree of Master of Science
at the Delft University of Technology,
to be defended publicly on Friday April 14, 2023 at 9:30 AM.

Student number: 4362284

Finalized on: April 6, 2023

Committee: Dr. P. Taheri, TU Delft, supervisor
Msc. K. Roohi, TU Delft, supervisor
Dr. M. Ramdin, TU Delft
Dr. P. Gonugunta, TU Delft

Abstract

Due to global warming, there is a rising demand for green energy storage and green fuels. CO_2 reduction can help mitigate these demands by storing energy in chemical bonds, thereby creating fuels that are relatively easy to use and store. In this way, a new carbon cycle can be created. Catalyst materials play a key role in improving the selectivity, productivity and stability of the CO_2 reduction reaction (CO_2RR). MOFs are an interesting catalyst material for this, as their porosity enables large surface areas and their structure allows for tunable selectivity. 2D-MOFs are especially beneficial due to their higher conductivity and mass permeability compared to 3D-MOFs. Carbonization can be used to improve the limited conductivity and stability of MOFs making them more suitable for CO_2RR . This is why this study investigates the effects of carbonization on the catalytic capabilities of 3D and 2D-MOFs for the CO_2RR . Therefore, Cu-BTC was carbonized using different parameters. The resulting materials were investigated via a multitude of electrochemical techniques to further understand their catalytic capabilities. The 2D-MOFs Cu-THQ and Cu-HAB were then carbonized and the CO_2RR products of the resulting catalysts were investigated. The analysis of the CO_2RR products created by the different MOF derived catalysts shows that the main influence on the selectivity of these catalyst materials is the size and distribution of the Cu-cluster formed during carbonization. Since SEM and EDS results showed that the Cu-cluster formation is influenced by the applied carbonization parameters, this shows that these parameters can affect the selectivity of the resulting catalyst. A reasoning for why the Cu-clusters influence selectivity is discussed, however this remains to be proven by future work.

Acknowledgements

Few things in life are performed by a single person without any support. The same is true for this Thesis. During the entirety of the project I received support and advice from a number of people. Here I would like to take the opportunity to thank them for all the time and energy they attributed to helping me. I could never have included the same amount of measurements and insights without any of their support.

First, I would like to thank my supervisors Peyman Taheri and Khatereh Roohi. Peyman I would like to thank you for introducing me to the thesis topic and providing me with the opportunity to find a project matching my own interests within this topic. Besides this, I thank you for your guidance and advice during the project.

As my daily supervisor, I especially want to thank Khatereh Roohi. I would like to thank you for always being available for support when I needed it during my lab work, ensuring that my measurements could be performed on time. Due to your positive attitude and helpful insights during our weekly meetings, I was provided with inspiration on how to progress further in the project every time. Also, the many hours spent reading through and providing feedback on my thesis and presentations are much appreciated. As my daily supervisor, you helped me through both the easy and the tough times. You were everything that a daily supervisor should be in my opinion.

I also want to thank Hans Brouwer, for the many carbonizations and thermal analyses you supported me with. Without your inspiration the fast carbonization methods applied would never have been realized. Besides this, many measurements in this report could not have been performed without you. Thus, I would like to thank you for all your supplied time, advice and interesting conversations.

I would like to thank Agnieszka Kooijman for introducing me to the rules and workings of a lab. Besides this you provided vital support when measurement equipment was not working properly, saving weeks of time and energy.

Then I would like to thank Prasad Gonugunta for your time reading the entirety of my thesis and providing me with multiple rounds of extensive feedback which ensured an improved quality of the report.

Furthermore, I want to thank everybody in the research group: Eszter Mádai, Mahsa Amiri, Mohammad Soleimani, Prasaanth Ravi Anusuyadevi, Songyan Liu and Yu Bi. All of you have provided me with advice and help at some point. Moreover, I want to thank you for making me feel welcome in the research group from day one.

Finally, I would like to thank my friends and family for their continued support and motivation throughout the entire project. You provided me with the motivation and energy required to complete a thesis as well as suffering through all the times I complained about my worries. Thank you for providing me with happiness.

*J. Coppen
Delft, April 2023*

Contents

1	Introduction	1
2	Literature Review	3
2.1	Basics of CO_2 Electrochemical Reduction	3
2.1.1	Limitations of CO_2RR	4
2.1.2	Performance indicators for CO_2RR Catalysts	5
2.2	Catalyst Material for CO_2RR	7
2.2.1	State of the Art 2D-Materials	7
2.2.2	Metal-Organic Frameworks	9
2.2.3	2D-MOFs	10
2.3	Carbonization	12
2.3.1	Carbonization Basics	13
2.3.2	Carbonization of Cu-BTC	13
2.3.3	Carbonization of 2D-MOFs	16
2.4	Effects of Nitrogen	16
2.5	Inference	19
3	Objectives of the Research	21
4	Experimental	23
4.1	Materials	23
4.1.1	Material and Parameter Selection	23
4.1.2	Material Description	27
4.2	Thermal Gravimetric Analysis (TGA)	31
4.3	Mass Spectroscopy (MS)	31
4.4	Scanning Electron Microscopy (SEM)	32
4.5	Energy Dispersive Spectroscopy (EDS)	34
4.6	Electrochemistry	34
4.6.1	Cyclic Voltammetry (CV)	36
4.6.2	Linear Sweep Voltammetry (LSV)	37
4.6.3	Electrochemical Impedance Spectroscopy (EIS)	37
4.6.4	Amperometry	39
4.7	Gas Chromatography (GC)	39
4.8	High-Performance Liquid Chromatography (HPLC)	40
4.9	Nuclear Magnetic Resonance Spectroscopy (NMR)	41
5	Results and Discussion	43
5.1	Characterization	43
5.1.1	Thermal Characterization	43
5.1.2	Surface Characterization	45

5.2 Electrochemical Measurements	53
5.3 Reaction Products	58
6 Conclusions	63
7 Recommendations	65
A Calibration Curves	67
B Additional Measurements	71

1

Introduction

Carbon dioxide (CO_2) is one of the atmospheric gasses of our planet. Traditionally, most living organisms exhale additional CO_2 into the atmosphere. Most plants use it in the photosynthesis process, which results in a natural removal process of this additional CO_2 [1]. Thus, it can be said that nature has kept the CO_2 content in the atmosphere in balance for millennia. However, recent industrial activities has started producing an additional 30 gigatons of CO_2 in various processes [2]. This additional CO_2 can no longer be removed by the natural carbon cycle, leading to an increased CO_2 concentration in the atmosphere [3]. This has caused a global rise in temperatures [4], resulting in droughts, floods and other extreme weather conditions around the planet [5]. To help mitigate these issues attempts are being made to find energy production processes with less CO_2 emission. So-called green energy production.

Besides this, new ways of energy production may have other advantages. The fossil fuels which are currently used are often only found at specific locations. This creates a difference in the availability of these resources for different countries, which causes political difficulties due to countries' dependency on each other [6, 7]. Moreover, any local and political changes in sites where fossil fuels are found can have a large impact on the prices of these resources. This can in turn impact energy prices [8] as well as the global economy [9]. Since green energy sources are often less site dependent, this can help mitigate these issues [10].

Even though solar and wind power are the fastest-growing green energy producers [11, 12], their energy production is irregular due to their dependency on the weather. Thus, the supply of energy has difficulty meeting the demand, especially because it remains difficult to store this energy [12]. One solution to this is by storing energy in chemical bonds [13]. This can be done by using renewable electricity to enable an electrochemical reaction to occur. During this reaction new molecules are created, containing bonds with higher energetic values than the ones present in the source reactants. A common electrochemical reaction for instance is electrolysis of water to hydrogen gas. However, H_2 is difficult to store and incompatible with most of the current engines [14–16]. An alternative method is using electrolysis to convert CO_2 into fuels and chemicals. CO_2 reduction reaction (CO_2RR) can create hydrocarbons,

carboxylic acids, etc. These fuels are easier to store and easily made compatible with currently used engines [17]. This is especially useful for applications where changing to other fuels is deemed impractical. Additionally, other CO_2RR products such as carbon monoxide can be used for the creation of feedstock for the chemical industry. Many of which are currently being produced using fossil fuels. Thus providing an environmentally friendly way of producing these materials can be also beneficial [18].

Eventually CO_2 reduction can be used to create an alternative carbon-neutral cycle, in which captured CO_2 is used to make synthetic fuels[19]. These fuels are then burned, at which point the CO_2 is released back into the atmosphere as shown in Figure 1.1. By transforming the CO_2 into fuels it is removed from the atmosphere, at least until the fuels are burned. Thus a part of the CO_2 in the air is temporarily stored in these fuels, slightly reducing the amount of CO_2 in the atmosphere. Both CO_2 capture and the making of fuel from CO_2 reduction are already decently developed. Thus the main item to be improved upon is the CO_2 reduction itself [19].

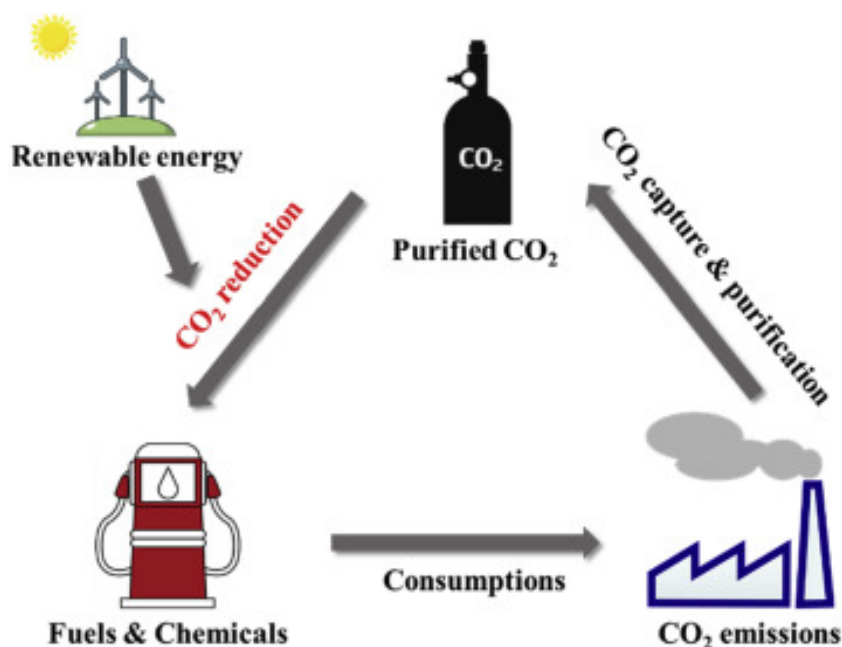


Figure 1.1: Schematic showing a simplified overview of the desired carbon cycle. Reproduced from [19].

Of the different factors which can be altered to improve the CO_2RR , the most influential one is the catalyst material [19]. Thus, this research study aims to find a suitable catalyst material for CO_2RR and then to investigate whether it can be improved upon further. To this end first, a literature review is conducted to identify a suitable catalyst material and a suitable way in which it can be improved. Then the objective of the research is further specified followed by an explanation of how this will be investigated. The materials used and the measurement techniques applied are discussed. In the conclusion, the findings relevant to the research objectives are summarized. Finally, possibilities for further research are discussed.

Literature Review

2.1. Basics of CO_2 Electrochemical Reduction

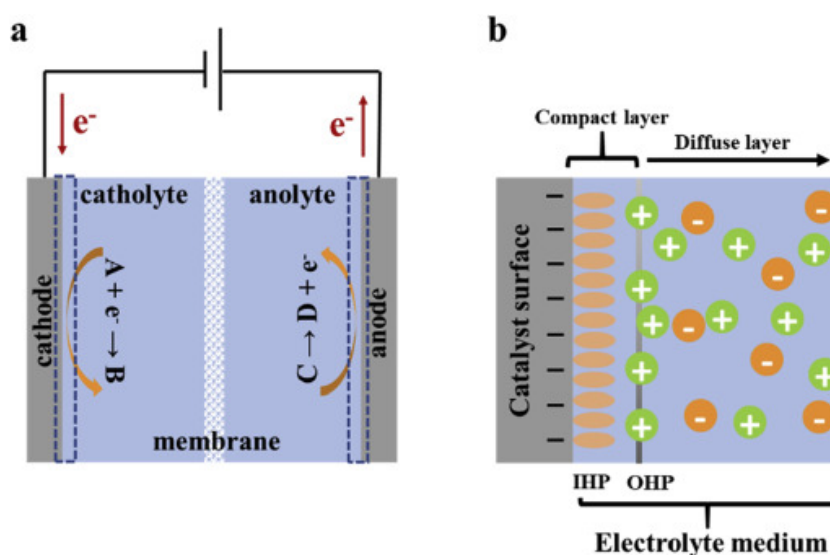


Figure 2.1: Schematic overview of (a) a standard two-chamber catalytic reaction cell and (b) a zoom-in of the area around the cathode, showing the different layers and ions. Reproduced from [19].

Figure 2.1a shows a schematic of a basic electrocatalytic cell. The cell consists of 2 chambers filled with a salted liquid that has ionic conductivity called electrolyte. An externally applied voltage over the cell drives electrons to the surface between the so-called cathode and the electrolyte. At the cathode, a reduction reaction occurs which involves electron transfer from the electrode to the chemical species dissolved in electrolyte such as CO_2RR . Therefore, the electrical energy is converted into chemical energy by forming new molecular bonds in the reacting species. The charge difference between the two electrodes creates a flow of ions from the cathode to the anode. The deficit of electrons is then compensated for at the other side of the cell where an anodic counter reaction occurs on the surface of the electrode. This supplies new electrons to the system, closing the loop. The two chambers are separated by an ion conductive membrane in order to prevent the products from the anodic and

cathodic reactions to get mixed [19].

In terms of CO_2 reduction reaction, the interface of the cathode and catholyte is where the CO_2RR happens. Due to the negative charge applied to the cathode, local positively charged ions are attracted to the surface resulting in the formation of the inner Helmholtz plane (IHP), outer Helmholtz plane (OHP) and a diffuse layer, as can be seen in Figure 2.1b. The IHP contains charged ions, reaction products, intermediate reaction products, adsorbed reactants and electrolyte. The OHP mainly consists of solvated ions of the opposite charge. These ions only interact with the cathode via long-distance electrostatic forces. Due to being filled with ions, the OHP and IHP together are called the compact layer. More mobile ions travel between the OHP and the bulk material through the diffuse layer [19].

2.1.1. Limitations of CO_2RR

	$E^{0'}$
$CO_2 + e^- \longrightarrow CO_2^{\cdot -}$	-1.90 V
$CO_2 + 2 H^+ + 2 e^- \longrightarrow HCOOH$	-0.61 V
$CO_2 + 2 H^+ + 2 e^- \longrightarrow CO + H_2O$	-0.52V
$CO_2 + 4 H^+ + 4 e^- \longrightarrow HCHO + H_2O$	-0.48 V
$CO_2 + 6 H^+ + 6 e^- \longrightarrow CH_3OH + H_2O$	-0.38 V
$CO_2 + 8 H^+ + 8 e^- \longrightarrow CH_4 + 2H_2O$	-0.24 V
$2 H^+ + 2 e^- \longrightarrow H_2$	-0.41 V

Figure 2.2: The half-reactions of the most common products produced through CO_2RR vs. SHE at pH 7. Reproduced from [20].

The half-reactions of common products of CO_2RR as shown in Figure 2.2. By looking at these, the first challenge for electrochemical CO_2 reduction can be identified to be the selectivity of the reaction. Since the potential of the different half-reactions lie close to each other, there are many difficulties in targeting a specific product to form. Aside from this, it can be seen that the potential for hydrogen production is reasonably close to the others. Since CO_2 reduction reaction commonly takes place in aqueous environment, this leads to consumption of energy in the hydrogen formation process. Thereby leaving less energy for the creation of the intended products. It seems positive that the minimum potentials that allow these reactions are reasonably low. However, the slow kinetics of the CO_2RR mean that actual potentials required are significantly higher in practice [19]. This difference between the predicted half-reaction potential and the potential required in practice is called the overpotential.

Another problem is the high energy barrier of -1.9 V for the formation of the initial CO_2^* anion on surfaces. It is not beneficial that this step is highly unfavorable, in part due to its geometric arrangement going from linear to bent [21].

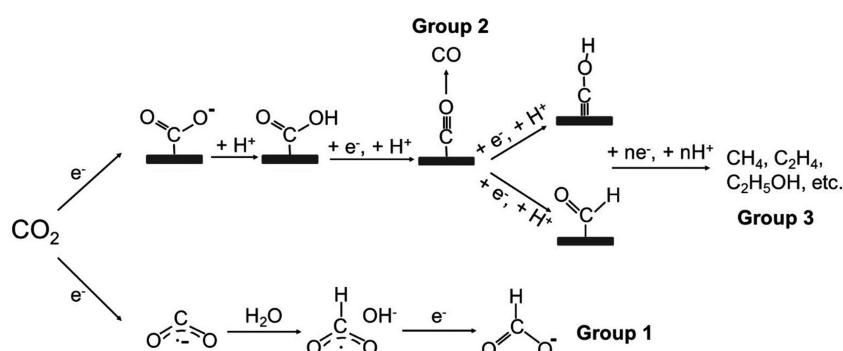


Figure 2.3: Schematic showing a simplified version of the reaction steps required for the main products produced in CO_2RR . Reproduced from [22].

Figure 2.3 shows a simplified schematic of the steps involved in the formation of different products from CO_2 . Here it can clearly be seen that for the formation of both CO as well as hydrocarbons, the first step is the creation of the CO^* anion. This indicates that the high potential required for this step is an issue. Figure 2.4 shows the theoretically proposed reaction steps when a carbonized metal oxide framework is used instead. It can be seen that the first step remains the same.

A good catalyst can speed up the reaction kinetics and lower the energy barrier for this first step [19, 21]. Furthermore, catalyst design can be used to improve the selectivity [20, 24]. For CO and formic acid a number of catalysts have managed to reach high selectivities, this remains difficult for more electron-intensive reaction products however [25]. Thus, good catalyst design can mitigate most of the current limitations of CO_2RR . The desired properties a material must have to be a good CO_2RR catalyst are good chemical stability, conductivity, high catalytic surface area and good mass permeability if it is porous [26].

2.1.2. Performance indicators for CO_2RR Catalysts

To determine the catalytic activity towards CO_2RR , it is useful to understand the indicators used to quantify the performance of catalyst materials.

Due to the complexity of the reaction pathways and variety of the products, one of the most important indicators of an efficient CO_2RR catalyst is product selectivity. Higher selectivity towards a specific product leads to a lower cost of post-separation techniques giving a low production cost [27]. Selectivity is related to the Faradaic efficiency (FE)[28]. FE is calculated using equation 2.1, in which n is the number of electrons theoretically required to make one mole of generated product according to its half-reaction, F is the Faraday constant, N is the actual obtained amount of moles of product through the electrolysis, and Q is the actual total charge consumed by the

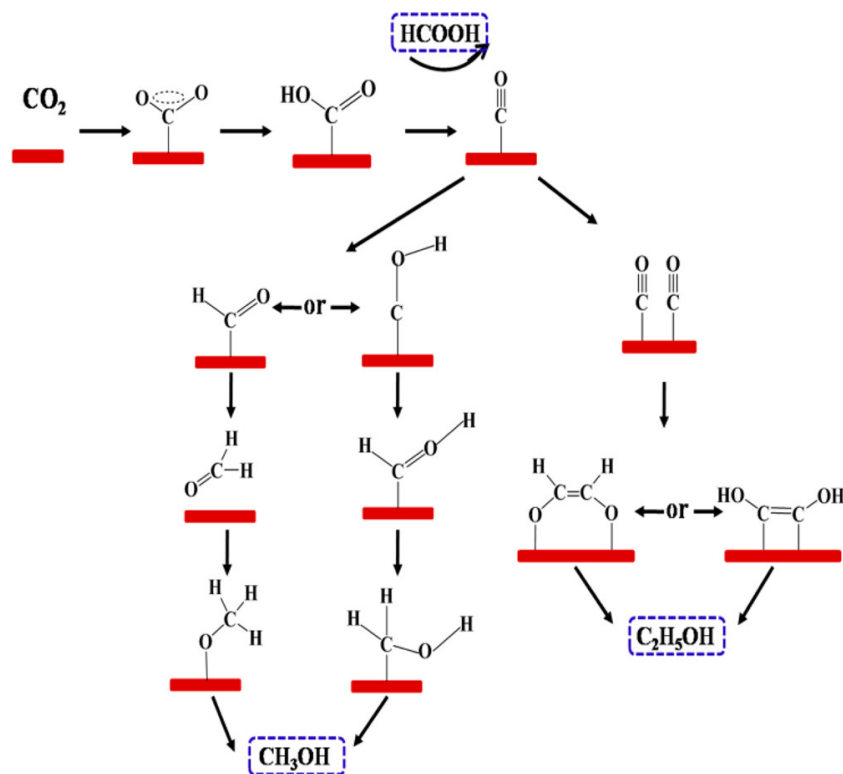


Figure 2.4: Proposed reaction steps for CO₂RR on copper(II)-benzene-1,3,5-tricarboxylate (Cu-BTC) derived Cu/C. It was carbonized at 1000 °C for 6 h under Ar atmosphere. Reproduced from [23].

electrolysis reaction [19].

$$FE = \frac{nFN}{Q} \cdot 100\% \quad (2.1)$$

Although FE indicates the efficiency of creating a certain reaction product, it is unable to provide any information on the rate of production per time scale. Faster production rates means less electrolysis equipment is required to obtain the same product production rate, thus lowering capital cost [27]. Hence, it is important to investigate the catalytic activity as well as selectivity. Due to difficulties in quantifying the exact number of catalytic sites, the catalytic current density is used to indicate the average activity of the catalyst. This can be calculated by normalizing the catalytic current by the electrode surface area. For practical simplicity, the geometric active surface area is usually taken as electrode area [29]. By dividing the current density by the FE of a specific product, the partial current density for that specific product can be obtained [19].

As it is important for a catalyst to have good selectivity and a good rate of production simultaneously, the performance indicators for these materials are sometimes combined. By multiplying the FE by the current density, the amount of current density used to form a specific product is found. This is called the partial current density and it shows the production rate for a specific product [30, 31].

As explained before, overpotential is also related to the kinetics of the CO_2RR . Thus it is essential to consider the overpotential required to achieve a certain current density. Alternatively, similar current densities can be compared and the difference in the overpotential required for them can be considered [29]. The overpotential can be calculated by taking the absolute value of the difference between the applied potential and the equilibrium potential of the appropriate CO_2RR half reaction [19]. A low overpotential is desired since this helps reduce operating costs of the CO_2RR [27].

Another important aspect is the stability of a catalyst material. This is usually tested by performing electrolysis over a longer time and measuring both current density and FE. It is important that both are measured to give conclusive evidence on the stability of a catalyst material for performing CO_2RR [19].

2.2. Catalyst Material for CO_2RR

As discussed in the previous chapter, an engineered catalyst can mitigate most of the CO_2RR limitations. Bulk metals were the first catalyst materials investigated for this purpose. Of these, Cu was shown to be unique in its ability to create multicarbon products such as hydrocarbons. However, at some point the limit of bulk metals was reached. This gave rise to investigations of a number of different catalyst materials, amongst which metal-oxides, carbon materials, metal alloys, etc. [25].

Even though this led to many new catalyst options [32–34], it became clear that bulk materials are limited since only their surface area can be used as catalytic active area. Thus, to increase the catalytic surface area of catalysts it is important to scale down the material to nano-size [35]. For example, R. Kas et al. [36] created nanoparticles from Cu_2O sheets with different orientations. They achieved FE of 43 % for ethylene production with a current density of 14 mA/cm^2 at -1.1 V vs. RHE in $0.1\text{ M KHC}O_3$ electrolyte. More recently, C. Kim et al. [37] made a Cu/Cu_2O porous aerogel network for use as a CO_2RR catalyst. They achieved a FE of 41.2 % for ethanol with a partial current density of 32.55 mA/cm^2 at -1.1 V vs RHE using 0.1 M KCl electrolyte.

A kind of catalyst material that combines the large surface areas of nano-structured materials with the added benefit of adapted electronic properties are 2-dimensional materials. This means the material consists of a few atom thick sheets, which are either stacked or arranged in a flower-like pattern. The edges of these sheets often have beneficial electronic properties, due to quantum confinement [38, 39].

2.2.1. State of the Art 2D-Materials

Since metals were known to work as catalysts, early investigations looked into making 2D-metal materials. $Cu/Ni(OH)_2$ nanosheets were created by L. Dai et al. [40]. Because of the Cu(0)-enriched surface, atomically thick stable Cu nanosheets were present resulting in a CO production of 92 % at -0.91 V vs. SHE with a current density

of 4.3 mA/cm^2 . The effectiveness of such catalysts led to investigations into a large amount of different 2D materials being investigated. In this section, recent developments of 2D-materials for CO_2RR are discussed and examples of the results obtained with these catalysts are provided.

Doped carbon

As a cost-efficient and well known 2D-material, graphene was one of the first 2D-materials investigated for CO_2RR . While pure graphene is chemically inert and a bad catalyst, doping it with heteroatoms like B or N has been shown to change these properties and make it capable of CO_2RR [41].

Wu et al. [42] for instance, doped carbon with nitrogen. For the sample with the highest amount of pyridinic N, they achieved a FE of 85 % for CO formation at -0.58 V vs RHE with a current density of -1.8 mA/cm^2 .

Group-VA elements

Aside from Carbon groups-VA elements like P, As, Sb and Bi are able to form layered structures similar to graphite. For the aforementioned examples, few-layered nano-sheets were created out of these structures. Recently these materials have been tested for use as CO_2RR catalysts.

Especially bismuth has shown to be suitable for formate production, being tested as early as 2014 [43]. In 2018, through optimizing the interlayer bond length He et al. [44] was able to achieve FE for formate of 95 %, with a high current density of 57 mA/cm^2 at -1.16 V vs RHE.

Transition Metal Oxides

Transition metal oxides (TMOs) have been widely used as catalyst materials due to their ability to form different product distributions compared to bulk metals [45]. This makes them interesting candidates for increasing the efficiency of a catalyst to produce a certain product. Since 2D-TMOs are expected to increase electrical conductivity as well as the number of active sites, attempts have been made at producing 2D-TMO catalysts for CO_2RR .

In order to investigate the effect of oxygen vacancies within TMOs on their ability to perform CO_2RR , S. Gao et al. [46] created atomic layer Co_3O_4 with and without oxygen vacancies. Experimental observation as well as density functional theory (DFT) calculations led to the conclusion that the oxygen vacancies in 2D- Co_3O_4 are able to stabilize the rate-limiting HCOO^* intermediate. Thus, slightly lowers the onset potential. Using this catalyst, a FE of 87.6 % for formate at -0.87 V vs. SCE was observed, with a current density of 2.7 mA/cm^2 . This was a better performance than the earlier tested 2D- Co_3O_4 catalysts [47].

Transition Metal Dichalcogenides

Transition metal dichalcogenides (TMD) like MoS_2 and WS_2 have been investigated as catalytic materials for CO_2 reduction for some time. It was discovered that the metal-terminated edges are responsible for their catalytic activity. By making these materials 2D, the number of available electrons at the edges can be significantly increased. This has led to a wide range of research in the catalytic effects of 2D-TMDs

[41].

M. Asadi et al. [48] confirmed this by vertically aligning MoS_2 nanoflakes resulting in a FE of 98 % for CO at -0.764 V vs. RHE with a current density of 65 mA/cm^2 .

MoS_2 was recently combined with Cu in order to create different products than CO [49]. A microwave hydrothermal method was used to create flower-like MoS_2 with 13.14 wt% nanosized Cu particles attached to it. This was shown to increase the specific surface area of the material. Cu-doped MoS_2 showed FEs of 38.6 % for CO, 10.8 % for CH_4 and 3.45 % for C_2H_4 at -1.4 V vs SCE, with a current density of -3.2 mA/cm^2 . It can be concluded that the added copper has an effect on the FE of the reaction products.

Transition Metal Carbides (MXenes)

A recently discovered potential 2D-catalyst material is Transition Metal Carbide (MX-ene). This is a 2D-metal carbide or nitride with a chemical formula of $M_n + 1X_nTx$, in which M is a transition metal, X nitride or carbide, n a number in the range 1-4 and Tx represents the surface termination groups [50]. Their catalytic activity originates from gas capture through their surface metal atoms with empty d-orbitals, as well as accelerated electron transfer due to their intrinsic metal properties [41]. DFT calculations predicted that MXenes were capable of allowing hydrocarbon product, with selectivity towards CH_4 . Cr_3C_2 and Mo_3C_2 were suspected to be the most promising candidates [51].

Moreover, experimental research by Attanayake et al. [52] has shown that both Ti-carbides and Mo-carbides are suitable for creating CO as well as formic acid. MoC_2 was used to create CO with an efficiency of 90 % at -0.77 V vs. SHE and a current density of 0.1 mA/cm^2 . In comparison, Ti_3C could also produce CO with an efficiency of 65 % at -1.17 V vs. SHE with a current density of -4.4 mA/cm^2 .

Ti_2CTx with additional surface -F was shown to reduce CO_2 with a FE of 56 % to formic acid at -1.76 V vs SHE with a current density of -0.3 mA/cm^2 , whereas M_2CTx reduced CO_2 to formic acid with a FE of 33 % at -1.23 V vs SHE with a current density of -0.6 mA/cm^2 . A current density of -2.57 mA/cm^2 was achieved at -1.7 V vs. SHE, but this caused a reduction in FE of formic acid to 20 % [50].

As can be seen from the above examples high FEs can be obtained for CO and formate production. However, the production of carbon hydroxides and other multi-carbon products is still less selective than desired. Thus investigating catalysts that are selective for these products may remain interesting.

2.2.2. Metal-Organic Frameworks

A relatively young possible catalyst material group being investigated for CO_2RR is metal-organic frameworks (MOFs). These materials consist of atomically sized metal centers surrounded by organic linkers. The metal centers coordinate the linkers in such a way that a 3D-structure is formed resulting in a nanoporous material as can be seen in Figure 2.5.

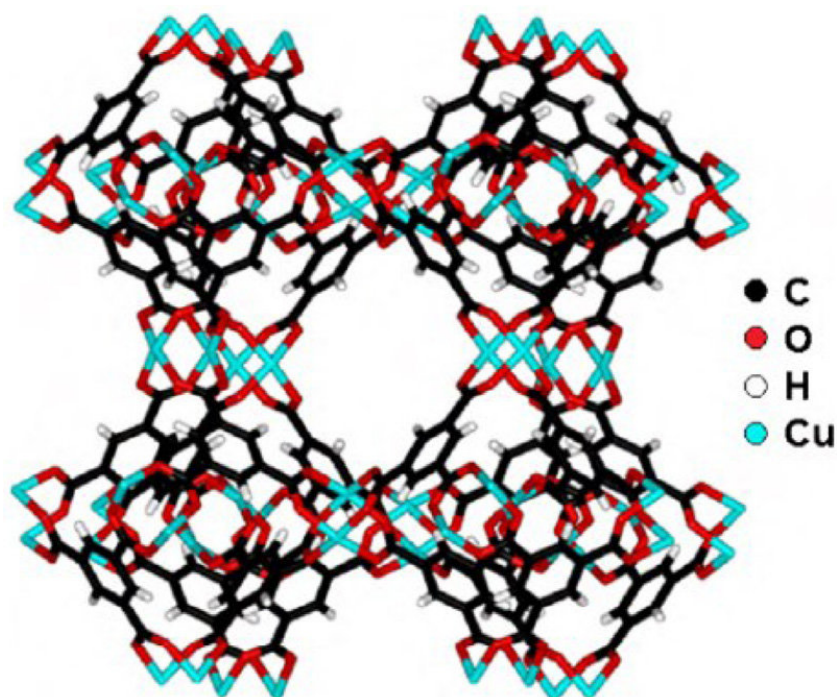


Figure 2.5: Structure of the commonly used MOF: Cu-BTC. Reproduced from [53].

Their elemental composition in combination with their structure gives MOFs certain advantages for CO_2RR . The metal center is often able to act as the catalytic site. However, the organic linkers themselves can also engage in the reaction as a catalytic active site. MOFs inherent nanoporosity allows reactants to reach these catalytic sites giving it a large catalytic surface area [54]. Because there is a large number of different suitable metal centers and linkers, suitable catalytic sites can easily be selected. Besides this, the different distances between catalytic sites can adapt the product selectivity [55, 56]. The combination of these properties make MOFs potential candidates for the selective production of CO_2 to specific products [57].

MOFs with different metal centers have been tested over the years. Fe [58], Co, Zn and Cu-MOFs [59–62] have all been investigated. Cu-MOFs stand apart from these due to their unique ability to create hydrocarbons [63]. Since hydrocarbons are a useful fuel [13], Cu-MOFs have been of interest to many researchers for some time.

MOFs are not without their flaws however. They generally have problems with their conductivity, stability and mass permeability. Improving the conductivity and the mass permeability should increase MOFs performance towards CO_2RR . Whereas good stability is required for practical applications [57].

2.2.3. 2D-MOFs

Recently a new type of conductive MOF has been developed, the so-called 2D-MOF. Instead of the 3D-structure that traditional MOFs form, the possible coordination options of the ligands around the metal centers make sure these MOFs form 2D-plates stacked on top of each other instead. The space between these plates gives

2D-MOFs higher mass permeability than traditional MOFs. Besides this they generally have higher conductivity, because their 2D-structure allows through-plane and through-space pathways [64].

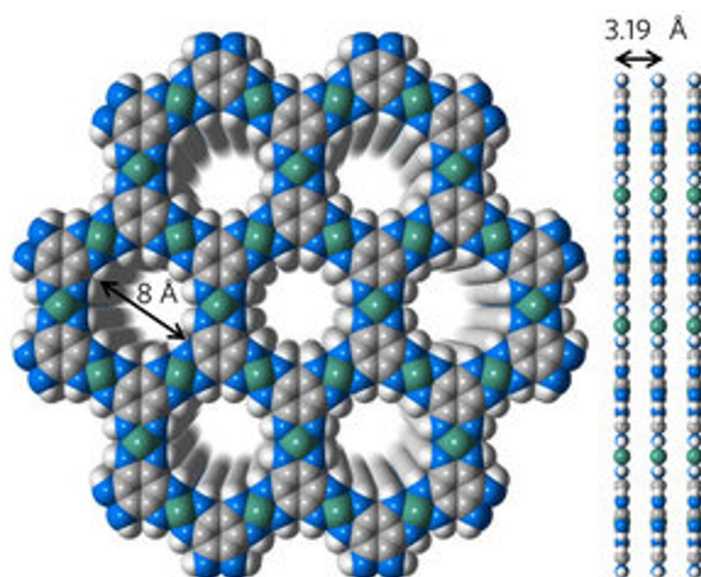


Figure 2.6: Structure of a 2D-MOF made from HAB. The Blue orbs are N, grey is C, green is Ni and white is H. Reproduced from [65].

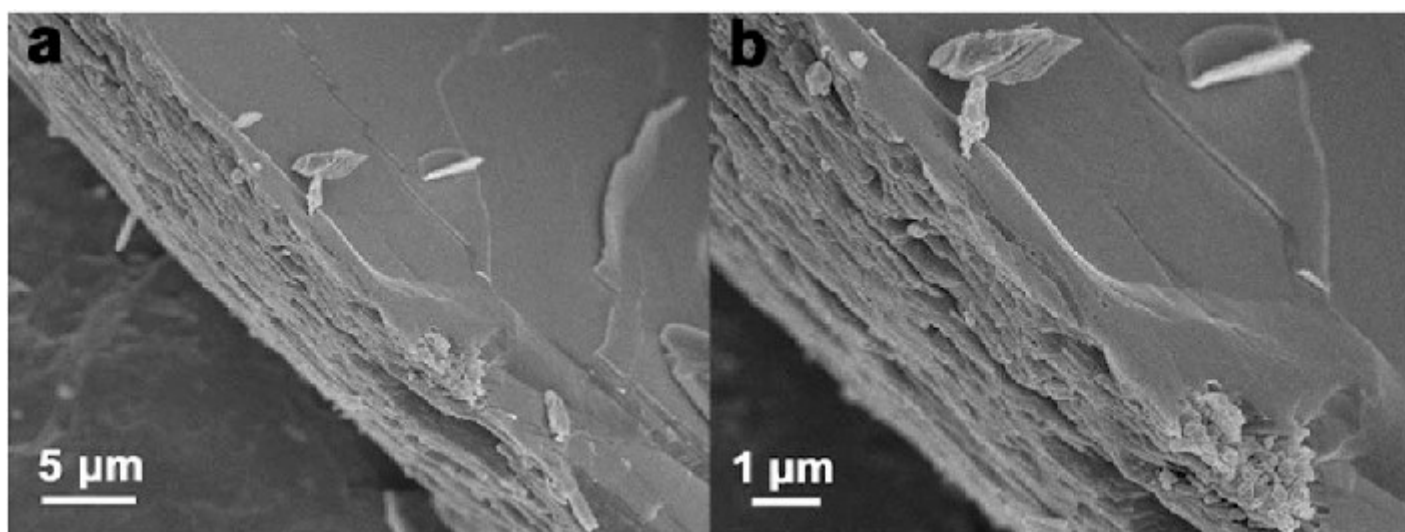


Figure 2.7: SEM image of 2D layer stacking in a Ni 2D-MOF. Reproduced from [66].

Figure 2.6 shows the atomic structure typical for a 2D-MOF. This structure forms stacks of 2D-platelets, which allows for better mass transport than for 3D-MOFs. The Scanning Electron microscope (SEM) images in Figure 2.7 show an example of this 2D-stacking in a Ni-2D-MOF. This 2D-morphology also gives 2D-MOFs different methods for electrical conductivity. Through-space conductivity due to Pi-Pi stacking allows for conductivity parallel to the nano-platelets whereas through-plane conductivity allows for conductivity along the platelets. 3D-MOFs usually use through bond pathways

as method for conductivity. This difference in conductivity methods allows 2D-MOFs to generally have higher conductivity than 3D-MOFs [64].

L. Majidi et al. [67] used the 2D-MOF Cu-THQ as a catalyst for CO_2RR . Liquid phase exfoliation was used to form Cu-THQ nanoflakes. 200 mg of these flakes were deposited on 1 cm^2 of gas diffusion electrode. This was then placed in a standard two-compartment electrochemical cell with electrolyte consisting of 1 M choline chloride and 1 M of KOH. This resulted in an average FE for CO production of 91 % between -0.135 V and -0.43 V vs. RHE.

F. Yang et al. [68] made use of Cull/adeninato/carboxylato metal-biomolecule frameworks to convert CO_2 to hydrocarbons. electrolyte 0.1 M $KHCO_3$. After obtaining a nano-sheet variation of the material it was added to an ink containing Nafion and ethanol. This was then drop cast onto a glassy carbon electrode. The electrochemical measurements were performed in an H-type cell. A Nafion membrane separated the two chambers of this cell. This resulted in a FE of 35 % at -1.4 V vs. RHE for C_2H_4 and a FE of 50 % at -1.6 V vs RHE for CH_4 .

L. Jingjuan et al. [69] used $Cu_3(HHTQ)_2$, $Ni_3(HHTQ)_2$ and $Cu_3(HHTP)_2$ in order to create CH_3OH . Using $Cu_3(HHTQ)_2$ resulted in the highest FE for CH_3OH of 53.6 % at -0.4 V vs RHE, at this potential the current density remained low at about -0.5 mA/cm^2 . $Ni_3(HHTQ)_2$ and $Cu_3(HHTP)_2$ did about 100 times worse with a FE for CH_3OH of 5.4 % and 1.9 % at -0.3 V vs RHE respectively. The electrode was prepared by mixing an ink containing $Cu_3(HHTQ)_2$, isopropanol and Nafion. This was then deposited onto carbon paper. The electrochemical measurements were conducted in an H-type cell using 0.1 M $KHCO_3$ as the electrolyte. The interesting difference between these materials is that only the $Cu_3(HHTQ)_2$ contains both Cu sites as well as nitrogen sites within the tricycloquinazoline cores of the ligand, showing the power of good interplay between ligand and metal center.

Even though this shows that the improved mass permeability and conductivity of 2D-MOFs can make them beneficial CO_2RR catalysts, their conductivity and stability remain lower than ideal. Thus it remains interesting to investigate ways to further improve these materials [70].

2.3. Carbonization

There have been multiple attempts on improving the conductivity of MOFs, such as introducing conductive ions into the MOF structure [71, 72]. However, this can decrease the amount of surface area and porosity in the material [72]. Alternatively, defect and grain boundary engineering can be used for MOF improvement. The effect of reducing grain boundaries on conductivity has been shown through the testing of single crystal MOFs [73, 74], although producing these single crystals remains difficult. Unfortunately, there is a limited number of research on the effect of defects on MOF conductivity [64]. Another way to improve MOF conductivity is by using them as a basis to derive a nanoporous carbon structure. This is done through carbonization.

2.3.1. Carbonization Basics

Carbonization is a process that is commonly used in the production of carbon rods and other carbon nano-sized materials. During the process, an organic material is placed in an oven under inert atmosphere. By increasing the temperature, existing bonds between carbon and the other elements present in the organic precursor break. As these elements leave the material, carbon creates bonds with the other carbon atoms in its vicinity. Eventually, a material made of pure carbon is formed [75].

In the case of Cu-MOFs, the linkers are organic materials, thus when carbonized at high enough temperatures, they will be converted into pure carbon. The Cu center does not evaporate resulting in the final material being a mixture of C and Cu. Since pure carbon-based structures have significantly higher electrical conductivity than organic linkers, the resulting Cu-doped nanoporous carbons tend to have higher conductivity than the pristine MOF. Moreover, nanoporous carbons are known for being chemically stable [76].

To make sure that the right elements are able to exit the material while obtaining an appropriate material structure, the right carbonization settings are required. The ramp-up speed, the temperature at which carbonization should take place, the duration of the process, and the flow of the inert gas have been named as factors influencing the resulting product [77]. Of these options, the holding temperature has been mentioned as being the most influential [77]. Thus, a number of different holding temperatures were investigated by researchers.

2.3.2. Carbonization of Cu-BTC

K. Zhao et al. [23] carbonized Cu-BTC at 900 °C, 1000 °C and 1100 °C. The results showed that the 1000 °C sample has a FE of about 45 % for CH_3OH and 27 % for C_2H_5OH at a potential of -0,3 V vs SHE. The electrode used to achieve these results was made with an ink containing active material, high-purity water and Nafion deposited on commercial carbon paper using a spin coating technique. A two-compartment electrolysis cell was filled with 0.1 M $KHCO_3$ electrolyte and equipped with a Nafion membrane for ion transport. They also found that with increasing temperature, the pore size and thus the specific surface area decreases. Nevertheless, the 1000 °C sample performed better for CO_2RR than the 900 °C one. This was attributed to the lower charge transfer resistance of the 1000 °C sample, Showing that the specific surface area is not the only important factor to consider for a CO_2RR catalyst.

L. Junyu et al. [78] used significantly lower holding temperatures of 300 °C, 350 °C, 400 °C and 500 °C to carbonize Cu-BTC. For a holding time of 300 °C, they also tried different heating rates. 1 °C/min, 5 °C/min, 10 °C/min and 20 °C/min were applied. Figure 2.8 shows the impact these settings have on the current density of the catalyst during CO_2RR . Using this and other results they concluded that higher heating rates combined with a 300 °C holding temperature lead to the formation of more Cu^+ sites originating from Cu_2O . This increased number of Cu^+ sites is considered to be linked to an increased CO_2RR activity of the materials. Using the catalyst carbonized at 300 °C with a 20 °C/min heating rate results in a FE of 43.8 % for CO production at -0.76

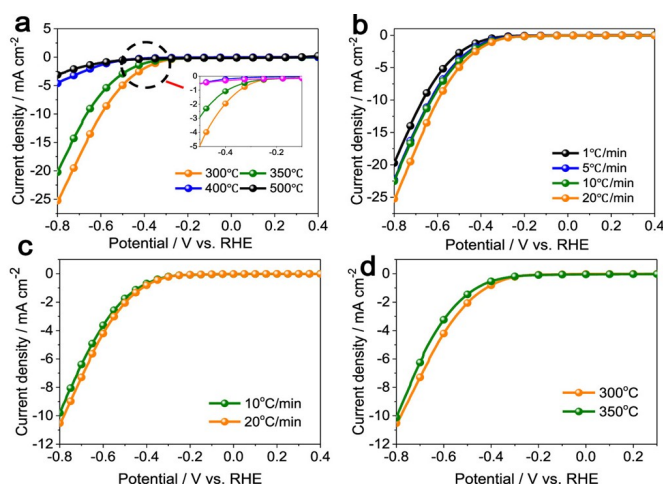


Figure 2.8: The effect of changing the holding temperature (a and d) and heating rate (b and c) on the current density of carbonized Cu-BTC for CO_2RR . Reproduced from [78].

V vs. RHE. The experiments were conducted using an H-type cell. The electrode was made by coating ink containing Nafion, active material and isopropanol onto carbon paper. The electrolyte used during the electrolysis was 0.5 M $KHCO_3$.

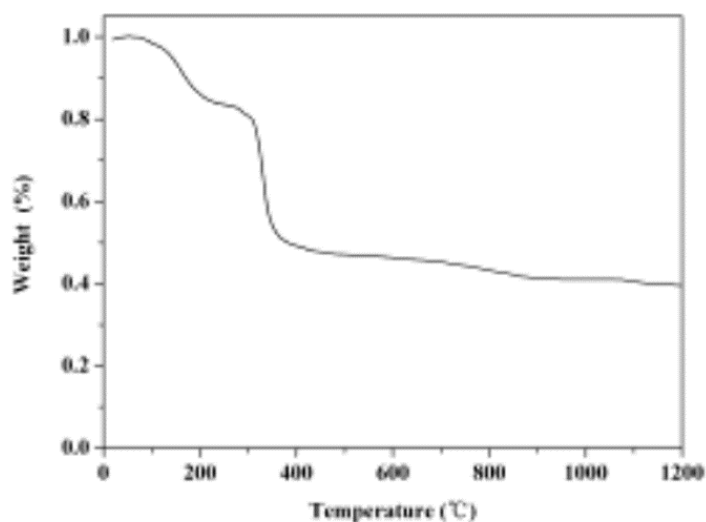


Figure 2.9: TGA analysis of Cu-BTC. The three main weight loss steps were attributed to loss of volatile solvent, loss of trapped water molecules and the largest loss around 300 $^{\circ}C$ to 400 $^{\circ}C$ due to decomposition of the linkers. Reproduced from [23].

Figure 2.9 shows a thermal gravimetric analysis (TGA) of Cu-BTC. It can be seen that there is a steep decline in mass between 300 $^{\circ}C$ and 400 $^{\circ}C$. This sudden change in mass was attributed to the main decomposition of the organic linkers. This means that during carbonization below 300 $^{\circ}C$, most of the oxygen in the material will be retained. When performed above 400 $^{\circ}C$ most of the oxygen will leave the material. Because full carbonization would mean only carbon and metal are retained, the amount of oxygen indicates the amount of carbonization that has occurred. If oxygen is retained this means that only part of the linkers has been carbonized, while others

retain their organic properties.

C. Wei et al. [79] also further investigated the carbonization of Cu-BTC, for use as a glucose detector. Different holding temperatures of 400 °C, 600 °C, 800 °C were investigated in this study. Figure 2.10 shows SEM images of the carbonized 400 °C and 800 °C, the original pyramidal structure of Cu-BTC can be recognized in black, whereas newly formed copper agglomerations show as white area. The results indicate that with increasing holding temperature the size of the Cu-particles on the surface grows. Moreover, with increased temperature, a decrease in micropores was observed as the original Cu-BTC channels collapsed. This leads to a decreased surface area. While at the same time, an increase in Cu-particle agglomeration results in a larger amount of meso- and macropores forming in the carbon framework due to the gaps left behind by the agglomerated Cu. This leads to an increase in surface area. As such, they found the highest specific surface area for a holding time of 600 °C.

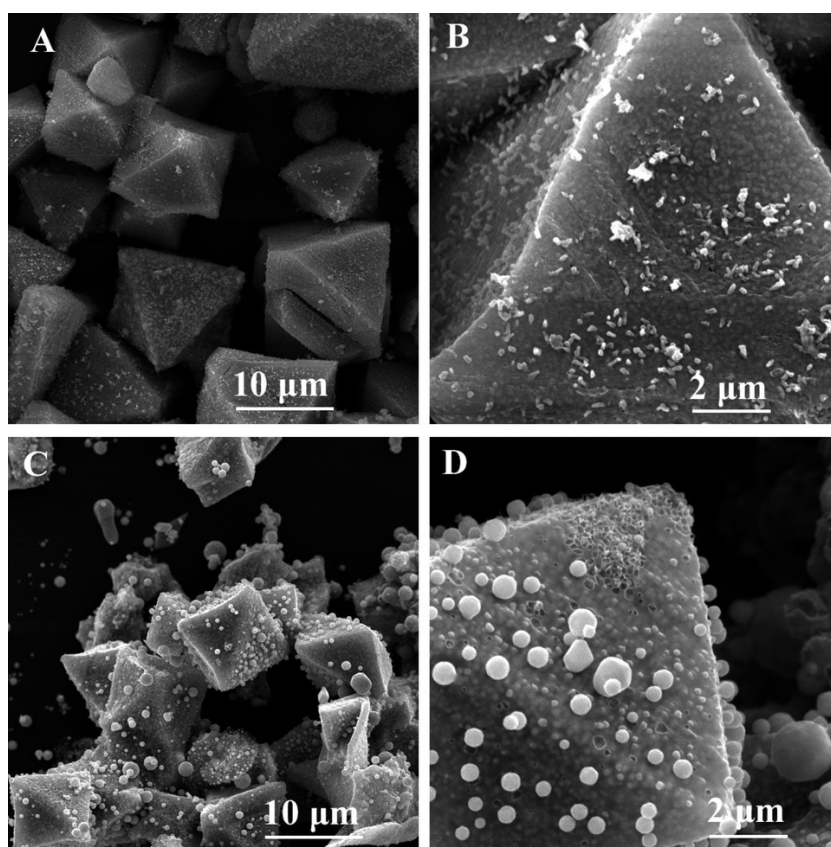


Figure 2.10: SEM images of Cu-BTC carbonized at 400 °C (A and B) and Cu-BTC carbonized at 800 °C (C and D). Different sizes of white Cu formations can be observed. Reproduced from [79].

Additionally, they varied the holding time for the 800 °C sample. 0 h, 2 h and 8 h as holding times were tested. They found that as the holding times increase, the Cu particles have more time to agglomerate, causing a decrease in specific surface area. However, it was also shown that longer carbonization times result in higher chances of micropore reformation, increasing the surface area. This concluded with the 8 h

holding time giving the highest specific surface area, with the 0 h holding time sample having a better specific surface area than the 2 h version.

2.3.3. Carbonization of 2D-MOFs

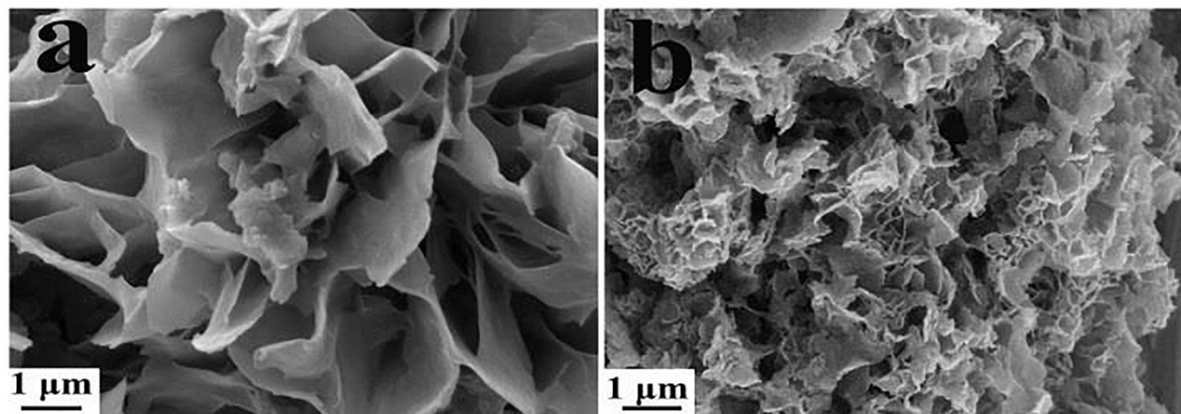


Figure 2.11: SEM image of pristine DUT-8(Ni) (a) and Ni@C obtained through carbonization of DUT-8(Ni) at 700 °C (b). It can be observed that both the size of and the distance between the flower like sheets has decreased. Reproduced from [80].

To the extent of our knowledge, carbonization of a 2D-Cu-MOF has not been investigated in the literature. However Wang, Q et al. [80] looked at the effects carbonization had on a 2D-Ni-MOF. They used the carbonized DUT-8(Ni) as a catalyst in the hydrogen evolution reaction. The carbonized material at 700 °C was found to have a lower distance between the nanosheets than the pristine MOF. In addition to that, the sheets seem to become smaller after carbonization. Figure 2.11 shows SEM images in which these effects can be observed. Some agglomeration of Ni was also observed, indicating that the effect of metal agglomeration also may occur in 2D-MOFs.

As a conclusion to this section, it can be said that carbonization at lower temperatures results in uncompleted carbonization, but can lead to a larger amount of Cu+ sites, especially in combination with fast heating rates. Higher temperature carbonization ensures full carbonization. However, if large Cu particles are formed, a decrease in specific surface area is also expected. Longer holding times may mitigate this effect since it allows micropores to reform. Yet they do lead to the formation of more Cu particles, thus if longer hold times are used they should be sufficiently long. For 2D-MOFs the distance between layers and the size of Nano-sheets may decrease. This provides some ideas of the influences of holding temperature, holding time and heating rate during the carbonization process.

2.4. Effects of Nitrogen

The presence of nitrogen in a pure carbon framework can influence their catalytic activity positively based on extensive studies [81]. As previously discussed, during the carbonization process, the holding temperature influences which elements would remain behind in the material. Thus, research has been conducted into the effect of retaining nitrogen in carbonized MOFs as well [76]. This chapter dives into the litera-

ture focusing on the effects of nitrogen on the CO_2RR capability of Cu-MOFs and their derivatives.

There are two ways in which the carbonization of a MOF can result in a nitrogen-doped system. Either a MOF with N-containing linkers is directly carbonized or a MOF is loaded with nitrogen-containing compounds while being carbonized. Using MOFs that contain N may influence the resulting carbonization product and its catalytic performance in a multitude of ways. For example, it has an effect on the capability for electron transfer between metal and carbon support, allowing for improved conductivity [81].

The mechanics of specific product formation in a carbon structure containing both N and Metals was investigated by A.S. Varela et al. [82]. By processing various Fe or Mn chloride salts they created four different carbon structures:

- one containing just N
- one contained Fe and N
- one containing Mn and N
- one containing Mn, Fe and N

Since these materials contain the same elements as Carbonized MOFs in similar ratios, the CO_2RR mechanisms for them may be comparable to those for MOFs. All the mentioned materials were shown to be effective for CO_2RR , with a FE of about 80 % for CO at -0.5 V vs. a reverse hydrogen electrode (RHE). This indicates that the nitrogen itself could well serve as an active site. However, the samples containing metals had significantly higher partial current densities, showing a significant increase in productivity when metal sites were present in the structure. The only difference between the Mn and Fe containing samples was that the Fe materials allowed for CH_4 formation at higher potentials. This led to the conclusion that although the N sites allowed for CO production, the CO molecules could then attach to the Fe atoms allowing the CO to reduce further into different products.

In an attempt to investigate this effect for Cu-MOFs, C. Yuan-Sheng et al. [83] investigated Cu-BTC both with and without added N into the material. They carbonized the N containing MOF at 200, 300, 350, 400, 600 and 800 °C for 1.5 h under Ar atmosphere. The 400 °C sample was found to be the most suitable for CO_2RR , with a FE of 20 % for CO and 20 % for ethanol at -0.8 V vs. RHE. At -1.1 V vs. RHE FE of formate could reach 12 %. This was attributed to the high contents of pyrrolic-N and Cu-N bonds in the carbon support. They also discovered that excess graphitic-N and oxidized-N atoms promote hydrogen production, which competes with the CO_2RR and thus reduces the catalyst's effectiveness.

L. Da et al. [63] carbonized nitrogen-doped Cu-BTC at 700, 800 and 900 °C for 5 h under Ar atmosphere. The best results were observed for 800 °C sample with a FE of 70.5 % at -0.68 V vs. RHE for formate. Aside from this ethanol was produced with a FE of 22 % at -0.38 V vs. RHE. The electrode was made by brushing an ink containing

active material, isopropyl alcohol and Nafion on a carbon cloth. The electrochemical measurements were performed in an H-type dual chamber cell with a Nafion membrane using 0.1 M $KHCO_3$ as electrolyte. They attributed the high formate FE to the Cu-N-Cu sites present in the material.

As a conclusion, carbonizing a MOF containing nitrogen has a positive effect on the resulting CO_2RR performance. It is interesting that these papers perform very similar experiments with significantly different results for the FE of formate after carbonizing at 800 °C. This could be due to the different carbonization times. Since both studies used different ways of making the nitrogen-doped Cu-BTC this may have impacted the results. Alternatively, both report using an H-type cell but do not specify all dimensions in this cell, nor are the cleaning methods for these cells or their membranes specified. This may result in differences in the measurements as well [84].

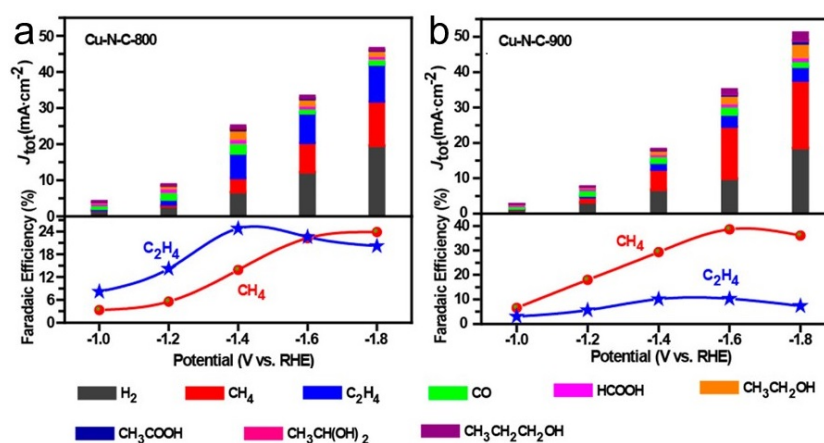


Figure 2.12: Faradaic efficiencies of CH_4 and C_2H_4 and current densities of all products for N doped Cu-BTC derived Cu-C catalysts, carbonized at (a) 800 °C and (b) 900 °C. Reproduced from [55].

Moreover, G. Anxiang et al. [55] investigated the effects of N on a Cu-BTC-derived Cu-C catalyst. Cu-BTC was carbonized together with dicyandiamide at 800 °C, 900 °C, 1000 °C and 1100 °C for 3 h under Ar atmosphere. Then the remaining Cu nanoparticles were etched away. This resulted in a carbon framework containing N-coordinated Cu atoms. By doing this they were able to show that the coordination of Cu by N sites could change the selectivity of the CO_2RR towards hydrocarbons, obtaining a FE of 40 % for Methane and 10 % for ethane at -1.8 V vs RHE. Besides, they were able to obtain different concentrations of Cu-N active sites in the material. 4.9 mol% Cu-N sites lead to the formation of ethanol, whereas 2.4 mol% lead to the formation of CH_4 . An overview of this can be seen in Figure 2.12, in which the Cu-N-C-800 has 2.4 mol% Cu-N sites and Cu-N-C-900 has 4.9 mol%. This shows an interesting relation of distances between active sites with product formation. With larger distances between sites leading to single-carbon products forming, whereas more closely placed active sites lead to multi-carbon products.

2.5. Inference

The most recent advancements in 2D-catalyst options were discussed, leading to the conclusion that successful results have been achieved for the formation of CO and formate, but the FE for hydrocarbon formation remains low. MOFs are an interesting catalyst material because their porosity and potential for different active sites in the same material can lead to a good specific surface area and product selectivity. Cu-MOFs are especially of interest since they have the innate ability to produce hydrocarbons. Unfortunately, they are limited by their low conductivity, stability and mass permeability. Recently discovered Cu-2D-MOFs show better conductivity and mass permeability. However, their conductivity and stability are still less than desired.

3

Objectives of the Research

2D-Cu-MOFs exhibit satisfying potential as CO_2RR electrocatalysts with the possibility to tune selectivity. However, they require further improvement before reaching suitable FEs and current densities. Carbonization is an interesting tool to further their conductivity and stability. Therefore, this research aims to investigate how carbonization can be used to improve the catalytic capabilities of 2D-Cu-MOFs.

As discussed in the literature review, some information on the effects of carbonization of 3D-MOFs catalysts is known. However, some areas remain disputed, while other aspects can be investigated more in-depth. Figure 2.9 shows the linkers of Cu-BTC MOF decompose somewhere in between 300 °C and 400 °C. As seen in the literature review, usually carbonization is performed above linker decomposition temperature (also referred to as full carbonization). However, L. Junyu et al. [78] carbonized Cu-BTC just below this temperature at 300 °C (partial decomposition). This was done in an attempt to obtain more electrochemical active Cu^+ sites. Since it can be difficult to compare electrochemical measurements when different cells are used [84], it is still useful to investigate whether the effects of full decomposition are more beneficial for the CO_2RR catalytic capabilities of MOFs than those for partial decomposition.

Besides this, all research so far uses a bottom-up approach in which different carbonization parameters are tested and the corresponding results are reported upon. However, no research so far has been done regarding a top-down approach in which the reported relations between carbonization parameters and resulting microstructure are used in order to create a more beneficial microstructure for CO_2RR . One way of doing this would be to investigate whether the amount and size of the Cu-clusters formed during carbonization can be limited by changing the holding temperature and time.

Thus, first insight into the effects of carbonization parameters on the catalytic performance of Cu-MOFs is required. To find this the following questions will be answered in this thesis:

- Is carbonization of Cu-MOFs below or above their linker decomposition temperature more beneficial for their catalytic capabilities for CO_2RR ?
- Does the size of Cu-clusters on carbonized Cu-BTC get reduced by changing the carbonization parameters, and does this influence the CO_2RR catalytic performance?

While a depth research on carbonization parameters, might provide us further insight into carbonization effects on the final catalyst, it does not provide further information on the effects that carbonization has on 2D-MOFs catalysts specifically. Since 2D-MOFs have only been applied as CO_2RR catalysts since 2015 [70], no investigation has been performed yet on the effects of carbonization on their catalytic capabilities for CO_2RR . To gain an understanding into these effects the following questions are being investigated:

- How does carbonization affect the catalytic selectivity and reaction rate of 2D-Cu-MOFs?

Moreover, the beneficial aspects of the presence of nitrogen within a MOF structure were discussed in the literature review. To further research the benefits of Metal-nitrogen coordination in a 2D-MOF, a final question will be answered:

- How does the carbonization process affect the catalytic selectivity and reaction rate of nitrogen-containing 2D-Cu-MOFs?

4

Experimental

In this chapter, an overview will be given of the materials and measurement techniques used in this report. First, the main characteristics of each MOF used will be discussed. Then the materials resulting from the different carbonization processes are mentioned, naming the specific parameters that were used to create each material. Finally, the different measurement techniques that were used are explained.

4.1. Materials

4.1.1. Material and Parameter Selection

As discussed in the literature review, it can be difficult to compare different electrochemical studies due to the many factors significantly impacting the results [84]. Thus, it is useful to first establish a baseline with a well-known material for the electrochemical set-up being used. Cu-BTC is the Cu-MOF of which the effects of carbonization on its CO_2RR catalytic capabilities have been most deeply investigated [23, 63, 78, 83] and is thus selected as the benchmark material in the present research. Additionally, pristine Cu-BTC performance towards CO_2RR results using the same set-up as used in this work, are available through our previous work [85].

Cu-BTC as the benchmark material was used to investigate the first two research questions, which have a focus on the parameters of the carbonization process. Due to the relative cheapness and availability of Cu-BTC more experiments could be performed, than if 2D-MOFs were used for investigation.

Partial vs full linker decomposition

To better understand whether carbonization above or below the linker decomposition temperature in Cu-MOFs is more beneficial for CO_2RR , Cu-BTC was carbonized using two different sets of carbonization parameters. One set of parameters attempted to utilize the most beneficial circumstances for partial decomposition, while the other set attempted to achieve a large amount of linker decomposition.

For this reason, the material representing partial linker decomposition was carbonized using the same heating rate, holding time and holding temperature as applied

by Junyu et al. [78]. This was done in order to achieve the same intended effect of an increased amount of Cu^+ sites. The material that resulted from carbonizing Cu-BTC using these parameters was called $Cu@C - (BTC)_{300C}$.

For the material representing complete linker decomposition, Cu-BTC was carbonized using the same heating rate, holding time and holding temperature as applied by K. Zhao et al. [23]. Their high holding temperature of 1000 °C combined with long holding times ensures the full decomposition of the linker. The material that resulted from carbonizing Cu-BTC using these parameters was called $Cu@C - (BTC)_{1000C}$.

Decreasing Cu-cluster size

One of the main effects that carbonization has on the Cu-MOFs is the formation of Cu-clusters. As discussed in the literature review, higher holding temperatures, longer holding times and faster heating rates lead to growth of these Cu-clusters. Larger Cu-clusters means a lower catalytic surface area, as smaller clusters have a larger available surface area relative to their size than larger clusters. Therefore, it is of interest to limit the growth of these particles.

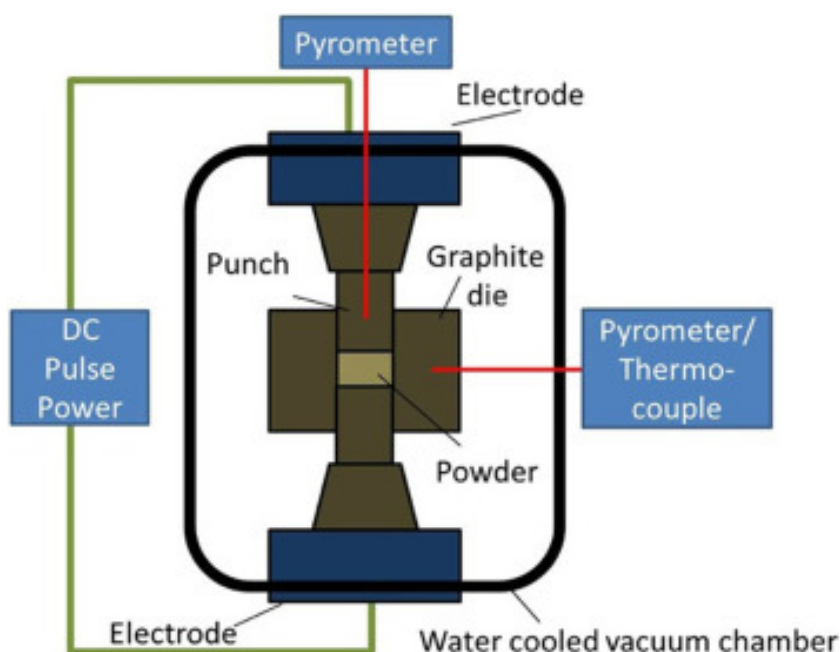


Figure 4.1: Schematic overview of the different components of a Spark Plasma Sintering machine. Reproduced from [86].

In order to limit this growth, a set of synthesis experiments were conducted with holding times reduced to zero and the heating-cooling ramp set as fast as possible. This leads to controlled Cu diffusion to the surface thus, smaller Cu-clusters. Moreover, the holding temperature was selected to be as low as possible. As seen in the previous chapter it is beneficial to remain well above the linker decomposition temperature. Since this temperature lies between 300 °C and 400 °C, a temperature of 500 °C was selected for the initial investigation to ensure that full decomposition could be

achieved.

To achieve very fast heating rates while still being under Ar atmosphere, a Spark Plasma Sintering (SPS) machine was used. As can be seen in Figure 4.1, in an SPS machine powder is placed in a die and put under pressure by two punches. Then, a large DC current is applied to it, which heats up the die through joule heating. In the case of conductive powder samples, the current can also heat up the powder directly. In addition, the small, if any, area in which the powder grains touch each other has to allow the current to pass through. This results in large resistances at these points, which leads to the electric charging of these areas. This energy is then occasionally released as plasma sparks, which heat up the material further. These heating mechanisms allow the SPS machine to achieve very high heating rates [87].

As this machine usually applies pressure to the material the first test was performed under the minimum amount of pressure that the SPS machine was able to apply of 4 MPa. As can be seen in Figure 4.2 this resulted in the MOF grains being squished into a flat shape, losing their beneficial porous structure and large surface area. Appendix B Figure B.7 shows that the resulting material is a close-packed mix of carbon and Cu. It can also be seen that little oxygen is present in the material, showing that the short holding time is enough to decompose the linkers under these conditions. As this has no immediate benefit over using pure Cu, a way needed to be found to use the SPS machine's fast heat-up without applying pressure.

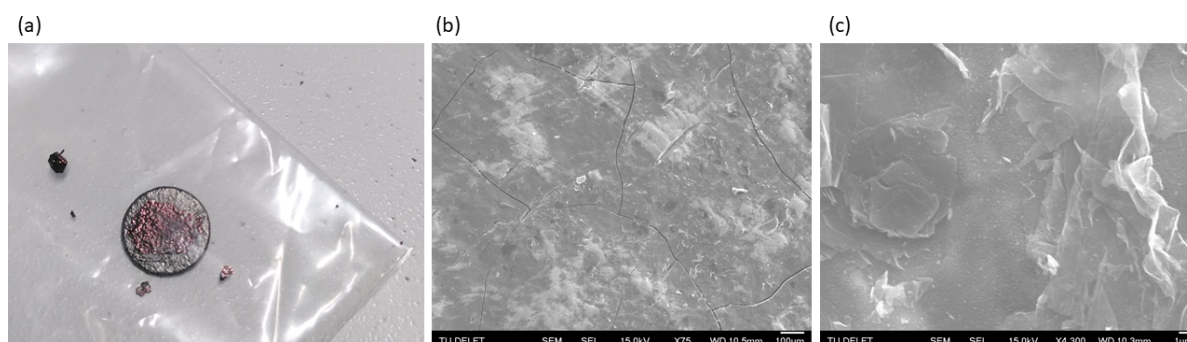


Figure 4.2: Cu-BTC placed in a Spark plasma sintering machine under 4 MPa pressure, heated and cooled down to 500 °C in as little time as possible. (a) resulting sample attached to carbon paper. (b, c) surface of the sample observed through a scanning electron microscope.

In order to limit the pressure a smaller die was placed inside the original larger die. The pressure pistons were then pressed on the walls of this smaller die instead of the sample, ensuring no pressure is applied to the powder. The contact area between particles is directly related to applied pressure. A lower contact area means that the powder will have a higher resistance [88]. Thus a larger part of the current will run through the sample holder walls instead of the powder. The heat is thus mainly produced by the Joule heating of the dies. This makes the SPS machine function more like a traditional furnace, except that it is able to achieve very high heating rates. Using this adapted SPS machine a new run was performed without applying pressure to

the material, resulting in $Cu@C - (BTC)_{500C-SPS}$ being formed.

$Cu@C - (BTC)_{500C-SPS}$ showed promise in its ability to produce CO_2RR products as well as having charge transfer resistance, it has low current densities however. With the aim to increase the current density while retaining the other beneficial aspects of this carbonization method, Cu-BTC was carbonized at 650 °C using the modified SPS machine.

Since $Cu@C - (BTC)_{1000C}$ had the best current density so far, increasing the temperature could lead to an increase in current density. However, to reach this higher temperature more time would need to be spent at elevated temperatures. This combined with the higher peak temperature could lead to more growth of the Cu-clusters. A number of different papers achieved successful CO_2RR properties through using holding times between 600 °C and 800 °C [63, 79, 89]. Therefore, a carbonization temperature within this range could provide higher current densities while still retaining low Cu-cluster growth. As seen for $Cu@C - (BTC)_{500C-SPS}$ in Figure 4.6 the high heating rate resulted in an overshoot of the set peak temperature. Due to this a set temperature peak of 650 °C was selected as this temperature combined with the overshoot results in an actual peak temperature close to 700 °C. Thus enabling a peak temperature right in the middle of the 600 °C and 800 °C range. The resulting material is named $Cu@C - (BTC)_{650C-SPS}$.

The structural composition of all of the differently carbonized versions of Cu-BTC was analyzed. Their catalytic performance for CO_2RR was also investigated. Then, the two materials showing the most potential for CO_2RR were selected to further investigate their selectivity and productivity during CO_2RR .

2D-MOFs

For the first 2D-MOF to be carbonized Cu-THQ was chosen for its comparable properties to Cu-BTC. It has a comparable pore size to Cu-BTC and also uses oxygen atoms as coordination environment. This allowed for better comparison between the 2D-MOF and Cu-BTC.

Since $Cu@C - (BTC)_{1000C}$ resulted in the most beneficial faradaic efficiencies as well as its carbonization parameters ensuring proper decomposition of the linkers, the same parameters were used for carbonization of Cu-THQ material. Besides this, A thermogravimetric analysis (TGA) combined with mass spectrometry measurement (MS) was performed to check whether the linker decomposition temperature was similar to that of Cu-BTC. The material formed through the carbonization of Cu-THQ was named $Cu@C - (THQ)_{1000C}$.

For the nitrogen-containing 2D-MOF, Cu-HAB was chosen. The nitrogen in this MOF is located in the coordination environment of the MOF. This allows for Cu-N-C sites to occur in the material which were mentioned to be influential on selectivity [82]. Also, the FE and current density of pristine Cu-HAB were investigated by Yu Bi [85] using the same electrochemical dual chamber flow cell allowing for a good compar-

isons to be made.

Because the goal was to keep nitrogen within the system, a TGA+MS measurement was performed in order to find a suitable temperature in which linker decomposition has occurred, but as little nitrogen had left the system as possible. This temperature was used as holding temperature, while the holding time and heat up rate were kept the same as for $Cu@C - (BTC)_{1000C}$ and $Cu@C - (THQ)_{1000C}$. The material formed through the carbonization of Cu-THQ was named $Cu@C - (HAB)_{550C}$.

Finally, the selectivity and productivity of the 2D-materials and the selected 3D-materials were investigated.

4.1.2. Material Description

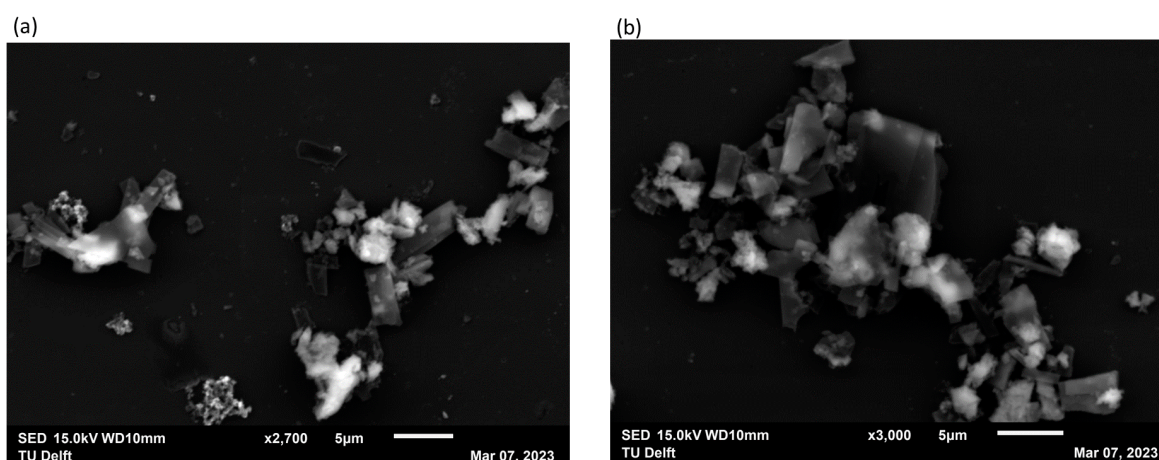


Figure 4.3: SEM images of pristine Cu-THQ grains. (a) multiple platelets spread further apart (b) multiple platelets huddled close together.

Cu-BTC forms pyramidal grains as can be seen in Figure 4.4. It consists of metal centers linked together through benzene-1,3,5-tricarboxylate (BTC) ligands. Oxygen is the binding atom between the Cu and the organic linker. As can be seen in Figure 2.5 its unit cell has cubic symmetry. The central void space has a diameter of nearly 9 Å. Smaller void spaces of about 2 Å and 5.5 Å are found within the octahedral structures at the corner of the unit cell [90]. Cu-BTC was obtained from Merck with a with a Cu-weight% between 27 % and 30 %.

Cu-THQ is a 2D-MOF that uses Cu as coordination centers and tetrahydroxyquinone (THQ) as linkers. This means its coordination environment consists of oxygen atoms. It has a pore size of 11 Å, making this relatively similar to the 9 Å void space of Cu-BTC [91]. It forms 2D-platelets as can be seen in Figure 4.3. Cu-THQ was purchased from CD-bioparticles with <0.1 % sulfur residue reported.

Cu-HAB is a 2D-MOF that uses Cu as coordination centers and Hexaaminobenzene (HAB) as linkers. Its coordination environment consists of nitrogen atoms. It has a pore size of 4 Å and a layer gap of 3.19 Å [92]. It forms stacks of 2D-nanosheets as

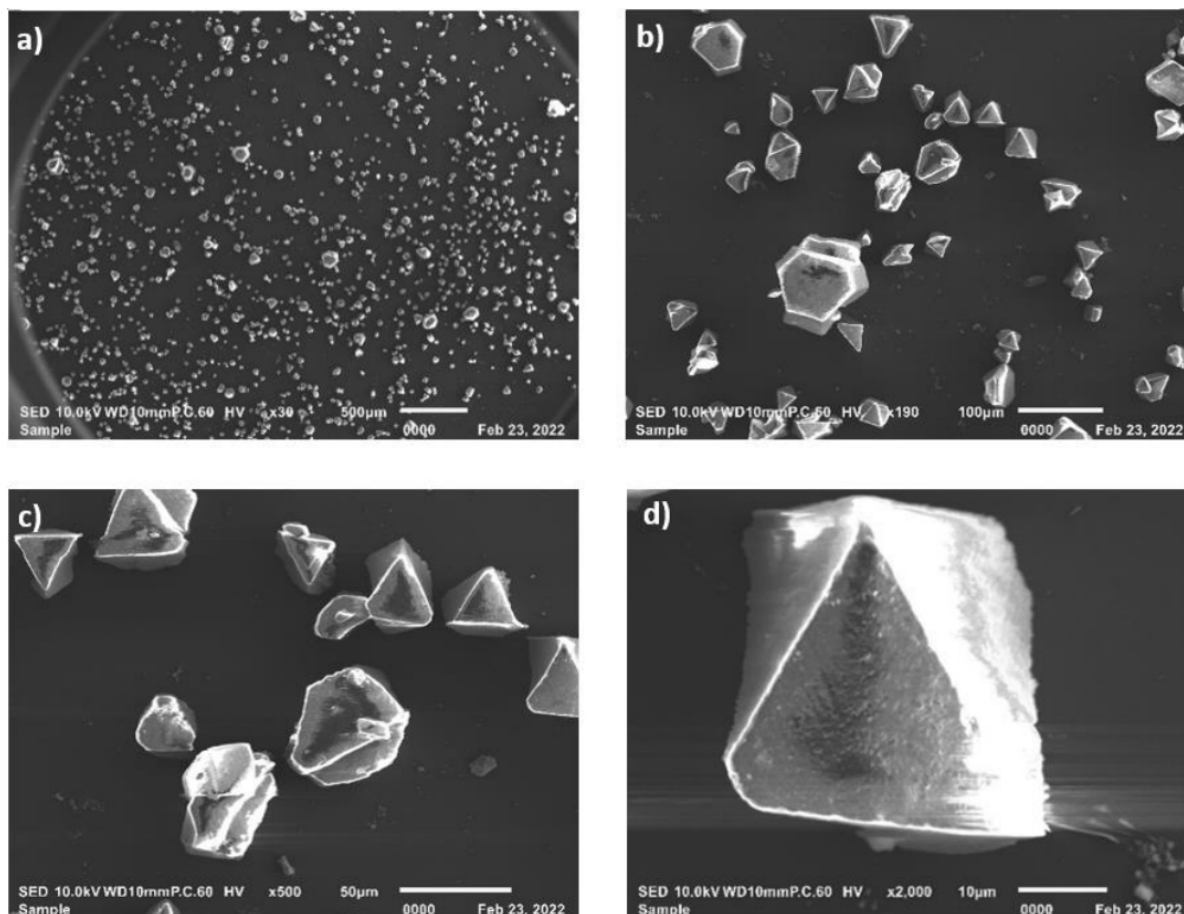


Figure 4.4: SEM images of the pristine Cu-BTC used in this research as obtained by Yu Bi. Reproduced from [85].

can be seen in Figure 4.5. Cu-HAB was synthesized according to the method used by D. Feng et al. [93]. First, 70 mg of copper nitrate hemi(pentahydrate) ($Cu(NO_3)_2 \cdot 2.5H_2O$) was soluted into 5 mL of degassed distilled water (0.060 mmol) mixed with 0.4 mL of concentrated aqueous NH_4OH . This solution was added to a solution of 30 mg $HAB \cdot 3HCL$ in 5 mL distilled water. This was then stirred in an open beaker at room temperature for 2 h. This resulted in a black powder, which was subsequently centrifuged, filtered and washed with distilled water and 6 M NH_4OH at 100 °C. The $HAB \cdot 3HCL$ was purchased from Toronto Research Chemicals with a reported purity of 95 %.

As baseline material, Cu-BTC was used to investigate the effects of changing certain carbonization settings. For this multiple versions of carbonized Cu-BTC were made.

$Cu@C - (BTC)_{300C}$ was made by placing Cu-BTC in a Lenton PTF 16/75/610 Tube furnace under Ar atmosphere. A heating rate of 20 °C/min was used to heat up the furnace to 1000 °C. It was kept at this temperature for 3 h after which the furnace was turned off and the system naturally cooled down.

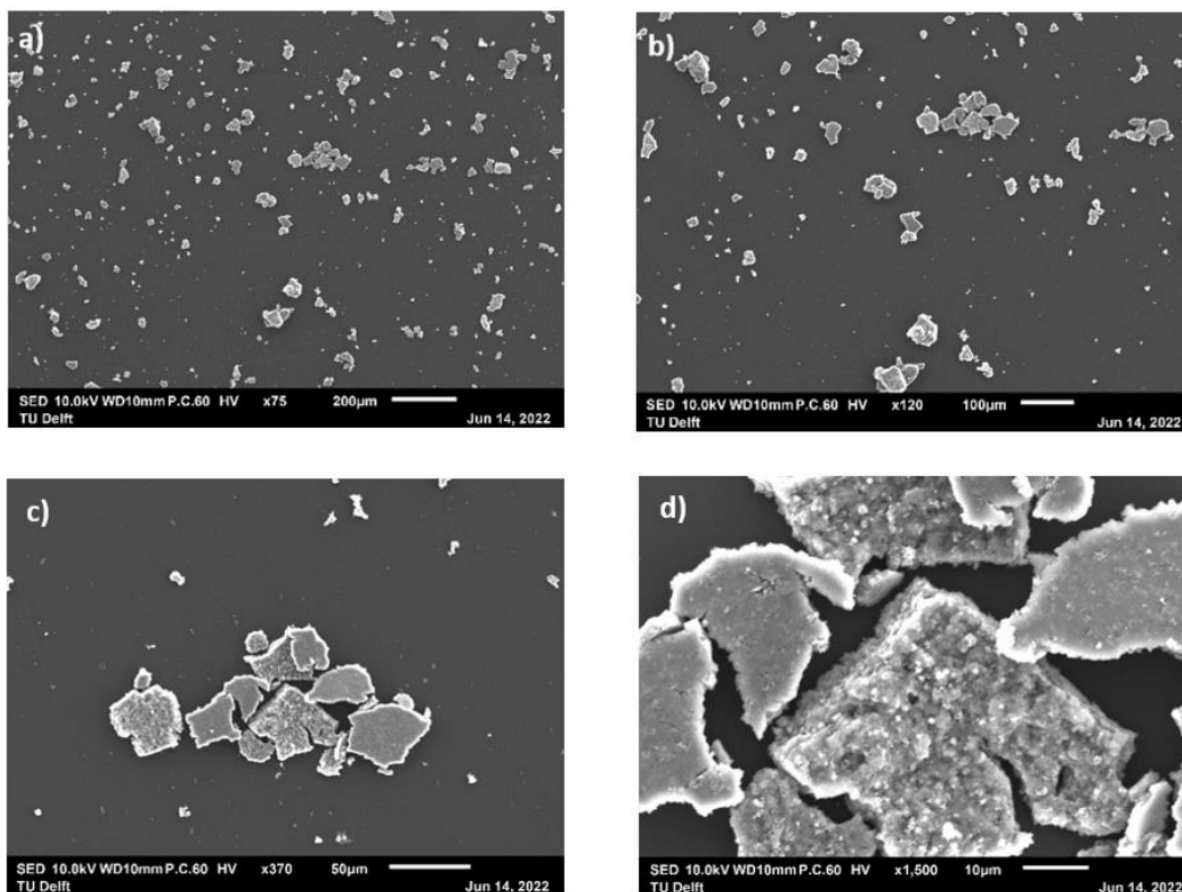


Figure 4.5: SEM images of Cu-HAB particles at different magnifications. (a) x75 magnification (b) x120 magnification (c) x370 magnification (d) x1500 magnification.

$Cu@C - (BTC)_{500C-SPS}$ was made by placing Cu-BTC in a Fischer Scientific HDP 25 Spark Plasma sintering machine under Ar atmosphere. The machine was adapted so no pressure would be applied to the MOF. The system was then programmed to heat up and cool down the material as fast as possible. It was set to heat up to 500 °C within 2 minutes and then cool down within two minutes. As shown in Figure 4.6, the machine was able to apply the heat-up rate as intended with only a slight overshoot in the maximum temperature, reaching 540 °C at its maximum. Cool down took slightly longer than programmed. This resulted in a total time of 4 minutes in which the material was above 300 °C and therefore 4 minutes in which carbonization could occur.

$Cu@C - (BTC)_{650C-SPS}$ was made by placing Cu-BTC in a Fischer Scientific HDP 25 Spark Plasma sintering machine under Ar atmosphere. The machine was adapted so no pressure would be applied to the MOF. The system was then programmed to heat up and cool down the material as fast as possible. It was set to heat up to 650 °C within 2 minutes and then cooled down within two minutes. As shown in Figure 4.7, the machine was able to apply the heat-up rate as intended with only a slight overshoot in the maximum temperature, reaching 679 °C at its maximum. Cool down took slightly longer than programmed. This resulted in a total time of 320 seconds in which the material was above 300 °C and therefore 320 seconds in which carboniza-

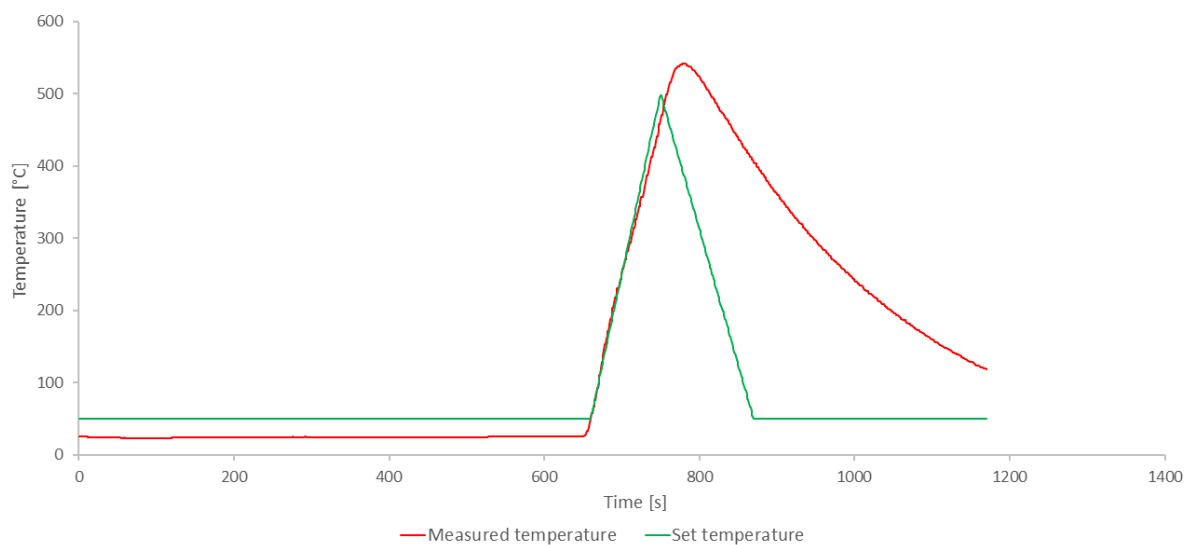


Figure 4.6: Programmed and measured temperatures of the SPS machine while carbonizing Cu-BTC at 500 °C under Ar atmosphere, without pressure being applied to the material. ($Cu@C - (BTC)_{500C-SPS}$).

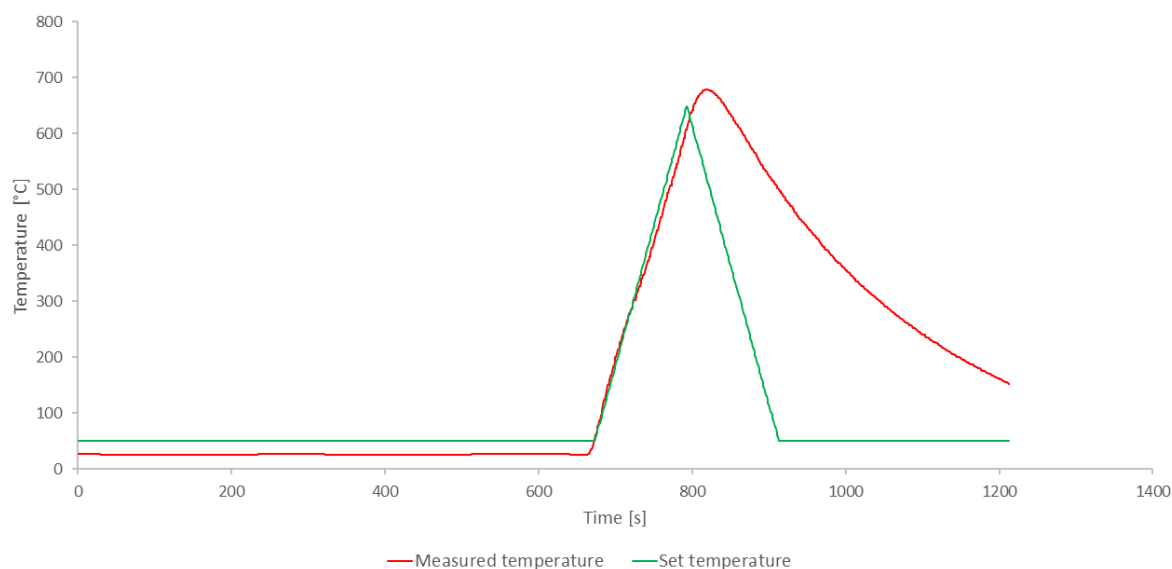


Figure 4.7: Programmed and measured temperatures of the SPS machine while carbonizing Cu-BTC at 650 °C under Ar atmosphere. ($Cu@C - (BTC)_{650C-SPS}$).

tion could occur.

$Cu@C - (BTC)_{1000C}$ was derived from Cu-BTC whereas $Cu@C - (THQ)_{1000C}$ was derived from Cu-THQ. The carbonization procedure for both materials was the same. Their respective MOF was placed in a Lenton PTF 16/75/610 Tube furnace under Ar

atmosphere. A heating rate of 5 °C/min was used to heat up the furnace to 1000 °C. It was kept at this temperature for 6 h after which the furnace was turned off and the system naturally cooled down.

$Cu@C - (HAB)_{550C}$ was derived from Cu-HAB, using the exact same furnace, heating rate and holding time as for $Cu@C - (BTC)_{1000C}$ and $Cu@C - (THQ)_{1000C}$. The only difference was that a holding temperature of 550 °C was applied.

4.2. Thermal Gravimetric Analysis (TGA)

Thermal Gravimetric Analysis (TGA) is a combination of a high-precision scale and a furnace with a temperature controller, as can be seen in the bottom half of Figure 4.8. In order to ensure that the scale itself is not affected by the temperature change it is usually placed above the furnace with an insulating layer in between. The actual sample pan is then hung down from this scale by a thin wire, so it ends up in the furnace. For consistent results, it is important that the height at which this sample hangs is reproducible [94]. Inert gas is flowing through the furnace in order to prevent any reactions between the sample and external gasses from occurring. The furnace is heated according to a pre-set heating rate, up to a pre-set temperature. During this heat up the weight loss is measured. This weight loss can then be linked to processes like loss of stored moisture or loss of material due to degradation [95].

carbonization is a temperature-driven degradation process, therefore TGA can help identify at which temperature this degradation occurs. Aside from this the moisture content inside can be used to get an idea of whether the bought MOFs were properly dried after synthesis. In this study, the machine used for TGA measurements is a TAG 1750 from the company Setaram. An Ar gas environment is used since this is the same environment as used for the carbonization process.

4.3. Mass Spectroscopy (MS)

When using only a TGA, it is hard to determine which one is causing the weight loss at a certain temperature if a lot of different temperature-dependent processes and degradations occur simultaneously. Therefore TGA is often combined with mass spectroscopy (MS) in order to show what gasses leave the sample at a certain temperature.

In the top half of Figure 4.8, it can be seen that when the gas from the TGA enters the MS machine the first step is generating ions from these gasses. This can be done by a multitude of different methods such as through temperature, electric fields or impacting particles. After this, the ions are separated and sorted according to their mass-to-charge ratio. This is achieved by applying magnetic fields or by ensuring a well-defined kinetic energy at the entrance of their flight path through the MS machine. After this separation, a detector is used to measure the amounts of ions received per mass-to-charge ratio. When one has a general idea of the atoms and molecules expected in the results, the mass-to-charge ratio can be used to identify which ion belongs to which detector response [97].

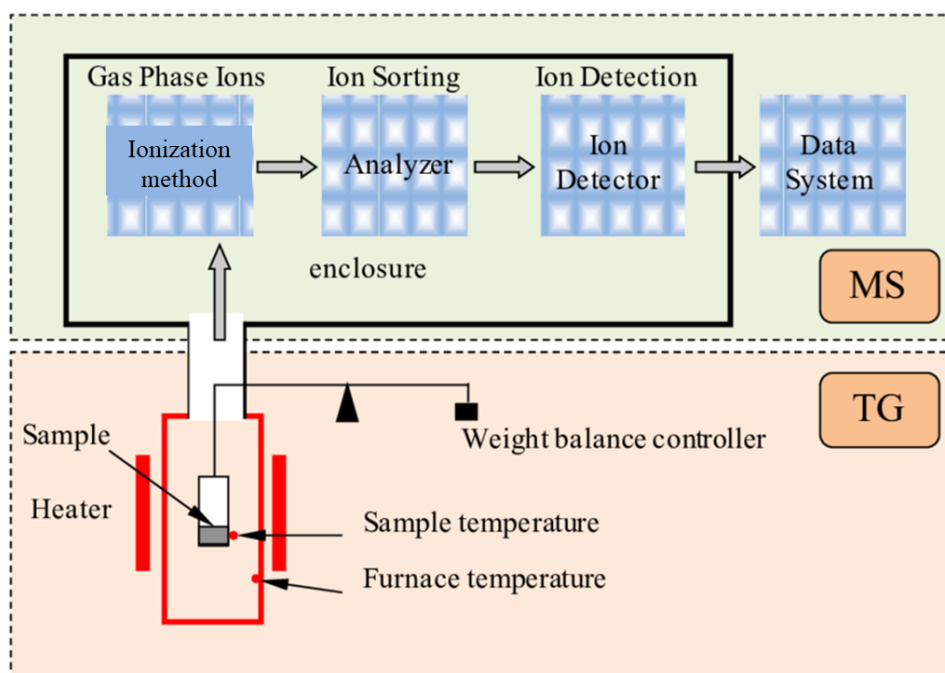


Figure 4.8: Schematic showing how the main components when a TGA (bottom half) is combined with MS (top half). Adapted from [96].

When combined with a TGA, the inert gas within the TGA is used as a carrier gas to bring any gasses leaving the sample to the MS. Since the MS measurement is fast, the temperature at which a certain gas is measured corresponds accurately to the temperature at which it formed [98]. Thus, a more in-depth understanding can be gained of what processes occur at what temperatures.

In this study, MS is used in combination with TGA to be able to get a better understanding of which elements degrade from the MOF structure at which carbonization temperature. To keep costs low this study uses small amounts of material, thus the ability of MS to function even with nanograms of analyte is beneficial when compared to other analysis techniques with similar objectives [97]. A Pfeiffer Vacuum GSD300 Omnistar MS was attached to the TGA machine and used for the combined analysis. This machine uses a hot tungsten filament to generate temperature, which then ionizes the analytes. A quadrupole mass separator alters the electric field in order to sort the different analytes. Ar gas was chosen as carrier gas because it was used as TGA environment and since it is not inherently present in any of the MOFs.

4.4. Scanning Electron Microscopy (SEM)

An electron microscope uses an electron beam to create a magnified image of objects from nano to micro-scale. The small wavelength of the electrons allows the microscope to observe smaller differences than would be possible if visible light was used. In Scanning Electron Microscopy (SEM) specifically, high-energy electrons are shot at a specimen. These high-energy electrons provide energy to atoms they interact with,

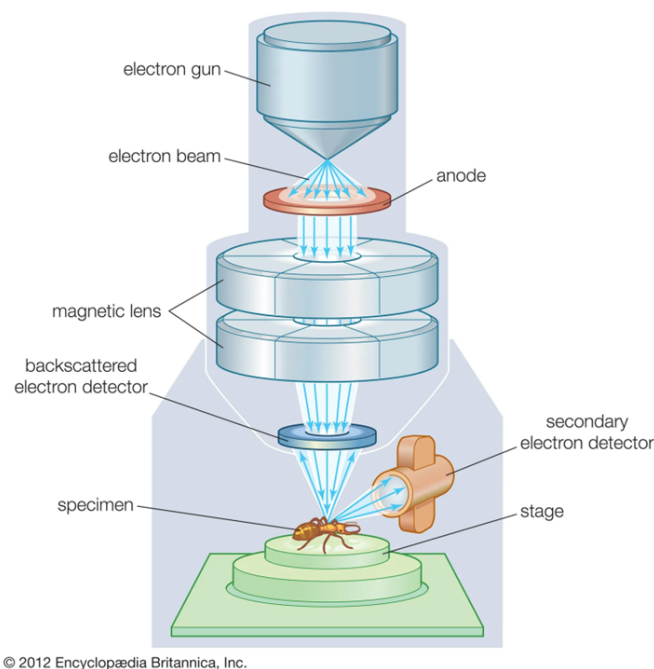


Figure 4.9: Schematic showing the main components of a Scanning Electron Microscope. Reproduced from [99].

which release this energy by emitting secondary electrons (and X-rays). The secondary electrons are then measured resulting in an image that can provide information on surface roughness, topography and morphology. Some SEMs are equipped to measure the emitted X-rays as well [100].

Figure 4.9 shows an overview of the main components of an SEM. On the top part, the high-energy electrons are created either by heating or by applying energy in the range of 1-40 keV. They then travel through a vacuum in order for them not to interact with unintended molecules. Magnetic field lenses and metal slits focus this electron beam to a monochromatic beam with a diameter of 100 nm or less. Scanning coils use magnetism to aim the beam over the specimen surface. In this way, the beam scans over the entire surface to be observed [100].

The penetration of the electrons is limited, so only information about the surface region of the specimen can be obtained. To prevent pile-up of excess electrons at the surface it is important that the surface of the specimen is conductive.

SEM is one of the most used techniques when it comes to making clear high-resolution images on micro to nanoscale [100]. Because it is so widely used, it is often easily accessible. In this research, SEM will be used to obtain information on any changes that occurred in the morphology of the MOFs after carbonization. A JSM-IT100 SEM is used in this study. The working distance is 10 mm with a working voltage of 10 kV.

4.5. Energy Dispersive Spectroscopy (EDS)

Energy Dispersive Spectroscopy (EDS) is often used in combination with SEM. When electrons get ejected from atoms by the SEM electron beam, electrons in higher valence bands can fall back to the now empty lower state. When this occurs x-rays are emitted [101]. These are then captured by an X-ray detector placed in the SEM setup. The energy of these X-rays is characteristic of the atom from which they originated [102]. Thus the surface elemental composition of the specimen can be discovered.

EDS is typically used for qualitative determinations of the elements present in a specimen [102]. In this study, it will be used to verify the removal of oxygen during carbonization. Besides this, it will be used in combination with the SEM images to understand the elemental composition of observed parts of these images. The SEM used in this study is equipped with a JOEL-made X-ray detector for EDS analysis. The settings were the same as for the SEM measurements.

4.6. Electrochemistry

Initially, electrochemical (EC) measurements were performed in a beaker. This beaker setup is shown in Figure 4.10 with the positions of working, counter and reference electrodes being indicated. A glassy carbon with drop casted active material, a platinum mesh and a calomel reference electrode stored in 3 M KCL were used for these respectively. The measured voltages were converted from this standard calomel electrode (SCE) potential to standard hydrogen electrode (SHE) potential after the measurements using the formula $E_{SHE} = E_{SCE} + 0.241$. The beaker is filled with 1 M $KHCO_3^-$ which is either saturated with CO_2 for 20 minutes or emptied of CO_2 by flushing it with N_2 for 20 minutes.

The downside of this setup is that it is difficult to keep the distances between electrodes consistent. And besides this, products of the cathodic and anodic sides cannot be kept separate to allow them to be measured. Luckily a dual chamber flow cell became available after a few months and the latter part of the EC measurements were performed using this flow cell. Figure 4.11 shows the different parts from which the cell was made. The distance between the electrodes and the membrane was 12 mm. 1.8 mL of 1 M $KHCO_3^-$ was injected in each chamber. The electrolyte at the cathodic side was then saturated with CO_2 for approximately 10 minutes using a constant flow of 10 mL/min CO_2 gas through the electrolyte, which was then retained during the experiments. The cell chambers were separated by an anion exchange membrane (AEM) made from FAS-PET-130. A miniature Ag/AgCl electrode and platinum plate were used as the reference and counter electrodes respectively.

All measurements performed for section 5.2 were performed in the beaker setup. All other EC measurements were performed using the flow cell.

The membrane was re-used for about 20 measurements before being replaced. After measurements, it was first rinsed for 2 minutes with distilled water and then

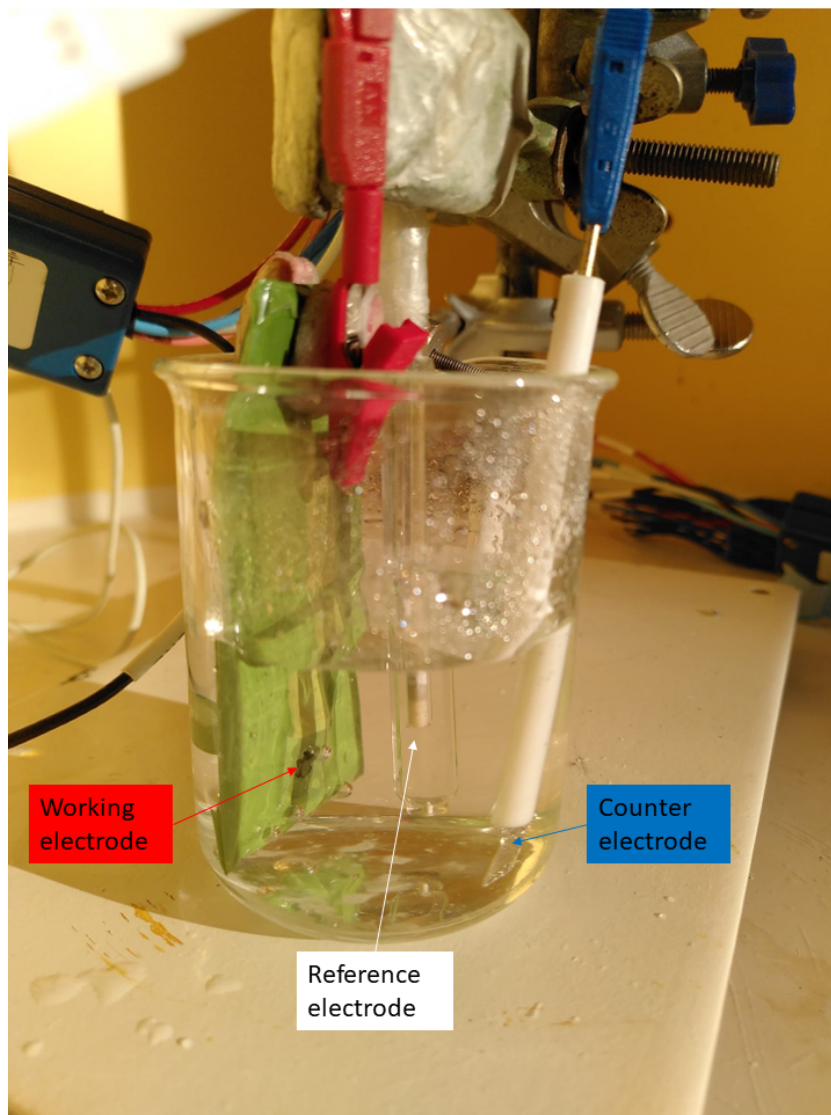


Figure 4.10: Beaker set up for electrochemical measurements, showing the positioning of working, counter and reference electrodes.

stored in fresh distilled water. Besides this, both the reference electrode and the cell were extensively rinsed with distilled water after each experiment. The reference electrode was stored in distilled water in between experiments.

The working electrode was made by drop casting ink on a glassy carbon substrate. This ink contained 5 wt% polyvinyl acetate (PVA), 5 wt% carbon black and 90 wt% active material soluted in 2 mL distilled water. This was then sonicated for 30 minutes before being drop casted. This ink was chosen as it was the same as used by Yu Bi [85], making it the results more comparable to the results achieved in that work.

However, after the initial electrochemical measurements for BTC it was noticed

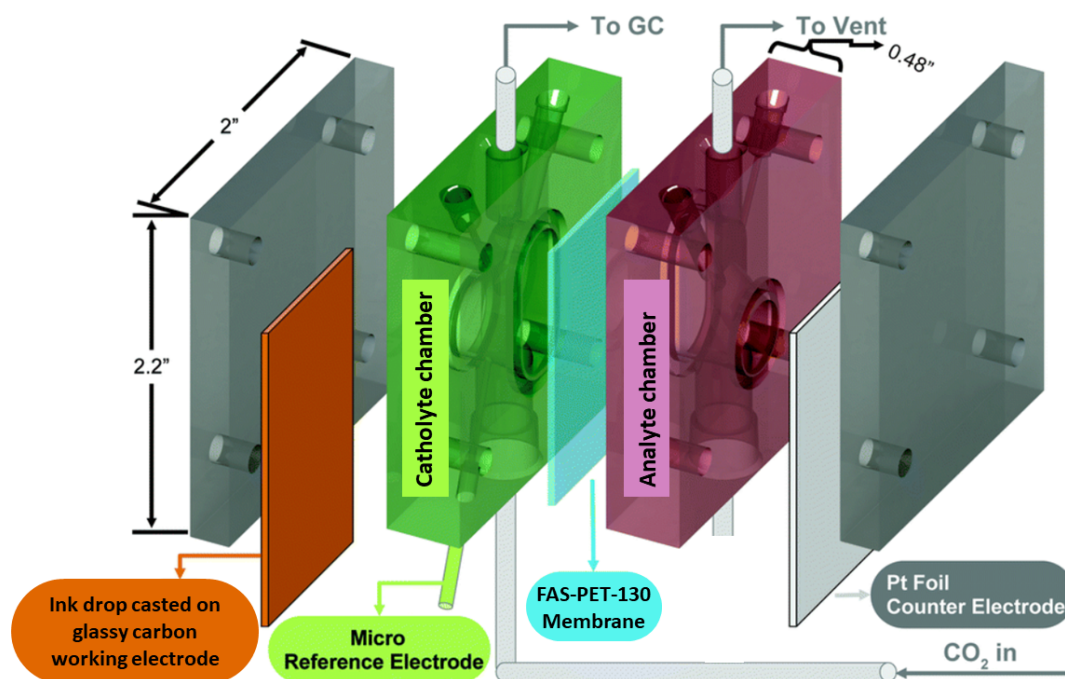


Figure 4.11: Schematic showing the different cell components and their dimensions. Adapted from [103].

that the materials did not solute sufficiently. Therefore, a different ink consisting of 20 wt% polytetrafluoroethylene (PTFE), 5 wt% carbon black and 70 wt% active material soluted in 2.5 mL water and 2.5 mL isopropanol was used for the tests using the flow cell. Since the carbonized MOFs dissolved better in this ink, only 10 minutes of sonification were required before dropcasting.

Usually, before an experiment was conducted an open voltage current test was run for 5 minutes to investigate whether the system was stable. If there was no large drift in the measured voltage the experiment was conducted.

4.6.1. Cyclic Voltammetry (CV)

In cyclic voltammetry, a varying voltage is imposed on the system and the resulting current is measured. As can be seen in Figure 4.12 the imposed current starts at a voltage E_1 and is then linearly increased to voltage E_2 after which it is brought back to E_1 using similar linearity. The voltage at which a certain current is measured is indicative for the ratio of F_c/F_{c^+} concentrations, thus allowing insights into the different reaction products present at a certain voltage. By sweeping the voltage in two directions it can be determined whether the reaction is reversible or not [104]. In this study, a VSP-300 (Biologic) potentiostat was used to apply the potential and measure the current. A scan rate of 5 mV/s was used over a potential range of 0 to -0.5 V vs SCE. If converted to SHE this range becomes 0.241 to -0.259 vs SHE.

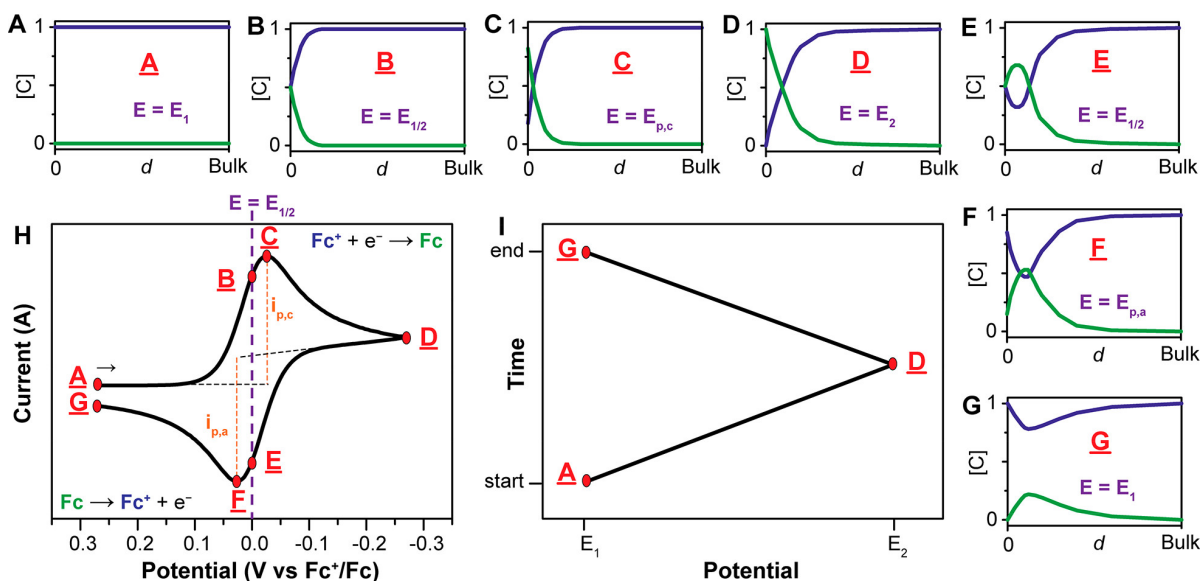


Figure 4.12: Overview of cv characteristics for the imaginary redox-reaction $Fc \rightleftharpoons Fc^+ + e^-$. (A-G) concentration profiles of Fc (blue) and Fc^+ (green). (H) Voltammogram of this reversible reaction using 1mM Fc/Fc^+ and a scan rate of 100mV/s. (I) overview of the imposed voltage over time. Reproduced from [104].

4.6.2. Linear Sweep Voltammetry (LSV)

In Linear Sweep Voltammetry (LSV) the voltage is swept over a certain range, while the resulting current is measured at certain intervals. The applied potential makes an oxidation or reduction reaction happen at the surface of the electrode. This reaction results in a flow of unreacted material toward the catalyst surface and a flow of reaction products away from it. This results in a current, the magnitude of which is determined by the rate of the redox reaction [105]. For CO_2RR LSV can be used to see the possible reaction rate at a certain voltage. Besides this, A sudden rise in current can be used as an indication that a reaction occurs at that potential. If this potential can then be linked to a half-reaction for a certain CO_2RR product this can indicate that the catalyst material has the capacity to form this product. In this study VSP-300 (biologic) potentiostat was used to perform the LSV measurements. A scan rate of 50 mV/s was used over a potential range of 0 to -2 V vs SCE. If converted to SHE this range becomes 0.241 to -1.759 V vs SHE.

4.6.3. Electrochemical Impedance Spectroscopy (EIS)

Electrochemical Impedance Spectroscopy (EIS) measures the charge transfer parameters of a given system [107]. In the case of CO_2RR this can be used to understand the ability of the catalyst to transfer electrons toward the reactants. A sinusoidal potential wave is applied to the system and the resulting current wave is measured. The phase shift (Φ) between these two phases is measured and used to calculate the impedance of the system. By doing this over a range of frequencies for the sinusoidal potential a Nyquist plot can be made. In a Nyquist plot, the real component of the impedance is plotted against its imaginary component. By representing the electrochemical system as a normal electric circuit, the resistance of solution (R_s), double layer capacitance at

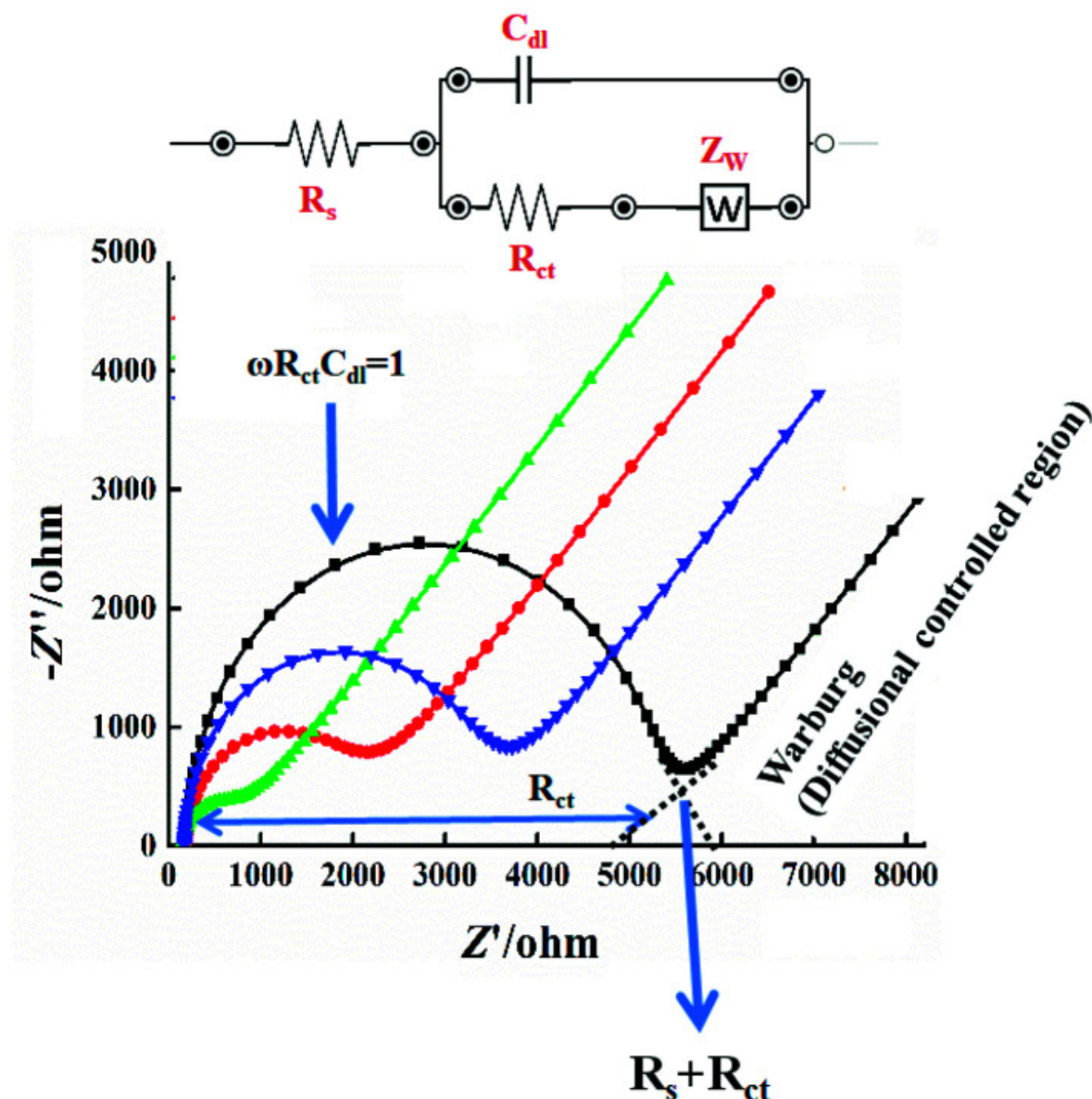


Figure 4.13: Relating the electric properties of the system to a representative electrical system at the top and to a Nyquist plot belonging to such a system (black squares). Other examples of Nyquist plots that could belong to the same representative electrical system can also be seen. Reproduced from [106].

the electrode surface (C_{dl}), charge transfer resistance (R_{ct}) and Warburg resistance (Z_w) can be linked to properties of the Nyquist plot [106]. Figure 4.13 shows which of these parameters relates to what part of the Nyquist plot.

In this study, EIS was mainly used to investigate changes in the R_{ct} , as changes in this resistance can be related to changes in the conductivity of the catalyst. EIS was performed both directly before and after LSV measurements in order to see the impact of the high voltage applied during LSV on the system's properties. A VSP-300 (biologic) potentiostat was used for the EIS measurements, in the frequency range of 100 kHz to 100 mHz. All EIS measurements were performed using the beaker setup.

4.6.4. Amperometry

In amperometry, a fixed voltage is applied and the change in current over time is measured at certain intervals. At the start of an amperometric measurement, when the voltage has just been applied, the electrode's change in potential will push away the ions of its opposing charge present around its surface. Moving ions are indistinguishable from electrons when measuring the current, therefore at the start of an amperometric measurement usually a non-faradaic effect can be seen. After a while, all the ions will have moved away from the electrode and the system should start to show more faradaic behavior [108].

In this study, amperometry was used in combination with gas chromatography (GC). The amperometric measurement applied a potential over the electrochemical flow cell to drive the CO_2RR . This created gaseous products which were then immediately measured by GC. The electrolyte in the cell was extracted after the complete amperometry cycle and the liquid products contained within were analyzed by high-performance liquid chromatography (HPLC) and nuclear magnetic resonance spectroscopy (NMR). The measured current could then be used in order to calculate the FE for the measured products. Besides this, the change in the current over time gives information on the stability of the system within the measured time span. Amperometry was generally performed for one hour using a VSP-300 (biologic) potentiostat. The current was measured every 0.100s. A voltage of -1.6 V vs Ag/Cl was applied in order to make the results comparable to the pristine materials as measured by Yu Bi [85]. Using the formula $E_{SHE} = E_{SCE} + 0.241$ this can be equated to -1.36 V vs SHE. The pH of 1 M $KHCO_3$ solution during CO_2 reduction at a copper surface with an applied voltage of -1.37 V vs SHE is about 7.8 during the first hour [109]. Thus, Using the formula $E_{RHE} = E_{SHE} + 0.059 * pH$, it can be shown that -1.36 V vs SHE is equal to -0.90 V vs RHE.

4.7. Gas Chromatography (GC)

During chromatography, a sample is physically separated into its different components. This is achieved by distributing the components over two different phases, one that remains stationary (the stationary phase) and one that moves in a specific direction (the mobile phase). In gas chromatography (GC) the mobile phase is a carrier gas. This gas is prevented from escaping by a leakproof glass or metal tube called the column. In this column, the stationary phase is positioned, which can either be a solid or a liquid, although the latter is more commonly used. When GC is performed the sample is transported by the carrier gas through a column. Here the sample goes in and out of the stationary phase based on its solubility in that phase. The components then separate based on their affinity for the stationary phase [110]. An illustration of how this interaction between sample, mobile phase and stationary phase results in a separated signal output can be seen in Figure 4.14.

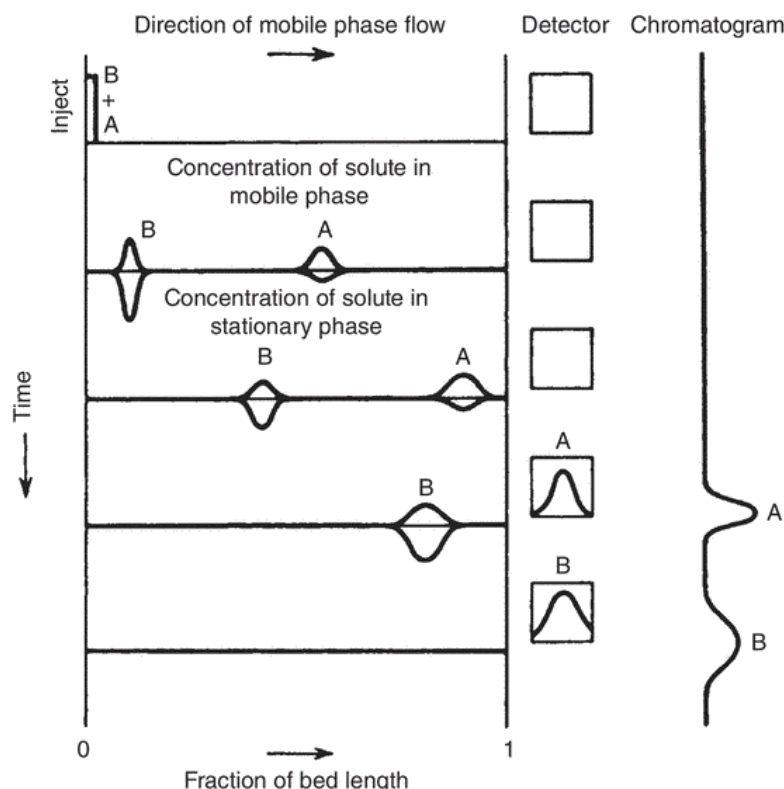


Figure 4.14: Schematic representing the flow of the sample components over time through the mobile and stationary phases. Eventually resulting in their separate detection. Reproduced from [111].

GC has fast analysis of typically minutes, it is sensitive up to ppm detection, reliable and relatively simple [110]. Especially the low detection limit is useful for detecting as many products as possible in this study. A Global analyzer solutions, compact GC 4.0 gas chromatograph was used for measuring the gaseous products. This GC has 3 different columns for product separation. Column 1 uses He as carrier gas and uses a flame ionization detector (FID). Column 2 also uses He as carrier gas and, while column 3 uses Ar as carrier gas. Both columns 2 and 3 use a thermal conductivity detector (TCD). In this study CH_4 and C_2H_4 are mainly detected in column 1, CO is detected in column 2 and H_2 is detected in column 3. The earlier described flow cell was used to perform the CO_2RR for the GC measurements. After filling it with 1.8 mL 1 M $KHCO_3$ the electrolyte was saturated with CO_2 for 10 minutes using a 10 mL/min gas flow. This flow was then retained for the rest of the experiment. First, a 5-minute OCV was performed to check the stability of the system. If the system was suitably stable, GC measurements lasting 1 hour were performed. During this hour the product was sampled and measured every 5 minutes. The calibration plots for the GC measurements can be found in Appendix A in Figures A.1 and A.2.

4.8. High-Performance Liquid Chromatography (HPLC)

After the CA + GC measurement, the electrolyte was collected for liquid products analysis performed by HPLC.

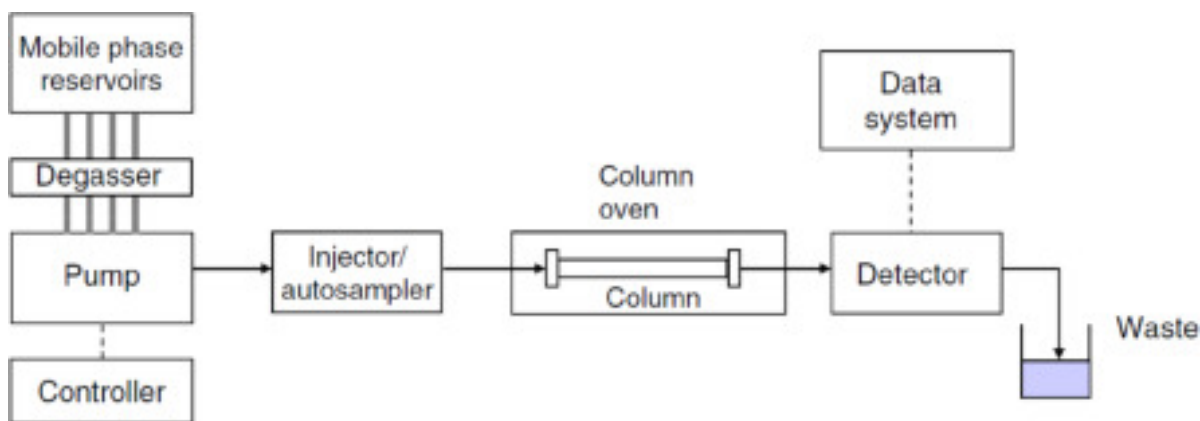


Figure 4.15: Schematic showing the different components present in an HPLC. Reproduced from [112].

In liquid chromatography, a liquid is used as the mobile phase. If the chromatography happens in a reusable high-pressure column then it is generally referred to as high-performance liquid chromatography (HPLC) [112].

An autosampler takes a couple of microliters of sample and introduces it to the HPLC. It is carried by the liquid mobile phase to the columns, where it is separated into its separate components. A number of different detectors are then used to differentiate between the different products and the background noise made by the liquid phase [112].

In this study an Agilent 1260 Infinity II LC System is used. It uses a diode array detector, otherwise known as the photodiode array detector. This is a type of UV-visible detector, in which the sample is irradiated with monochromatic light and the transmitted light is measured. It measures analytes that absorb certain wavelengths in the UV spectrum like alkenes, aromatics and analytes with multiple bonds between S, N, O and C [112]. The calibration plots for the HPLC measurements can be found in appendix A Figure A.3.

HPLC is useful as it is very quick when using simple mixtures, only requires microliters of material [113] and has good accuracy [114]. Unfortunately, its UV-visual detectors are only able to detect materials that absorb UV light. This coupled with its sometimes imperfect separation of analytes makes it so that HPLC can have difficulty with detecting certain materials present in the mixture [114].

4.9. Nuclear Magnetic Resonance Spectroscopy (NMR)

Nuclear Magnetic Resonance works by bringing the nuclei in resonance. The isotopes of certain nuclei like, 1H , ^{13}C , ^{19}F and ^{31}P are magnetic in nature. This means that when a strong magnetic field is applied, the nucleus travels in the field direction with a frequency proportional to the field strength. If the nucleus is then simultaneously bombarded by electromagnetic waves with similar frequency as the nuclei and which are traveling perpendicular to the magnetic field, resonance of the nuclei oc-

curs. This frequency is dependent on the chemical bonds present in the material and its environment. Comparing this to reference spectra and the characteristic frequencies for different bonds, the materials present can be discovered [94].

For one of the CA measurements instead of using HPLC, the electrolyte was investigated using NMR. The goal was to investigate if there were any liquid products that were difficult to detect with HPLC but could be detected using NMR. Besides this, it was used to verify the results obtained by HPLC. For this study, a Bruker Ascend 500 ($B_0 = 11.7$ T) magnet equipped with a NEO console NMR machine was used. MestreNova software was used to deconvolute the peaks.

Results and Discussion

In this chapter, the results obtained by the different measurement techniques are discussed. First, the different variations of carbonized Cu-BTC are considered. Their SEM, EDS and EC results are discussed. This is followed by the SEM and LSV measurements of the carbonized 2D-MOFs. Finally the FEs and partial current densities of $Cu@C - (BTC)_{1000C}$, $Cu@C - (BTC)_{650C-SPS}$, $Cu@C - (THQ)_{1000C}$ and $Cu@C - (HAB)_{550C}$ are compared.

5.1. Characterization

5.1.1. Thermal Characterization

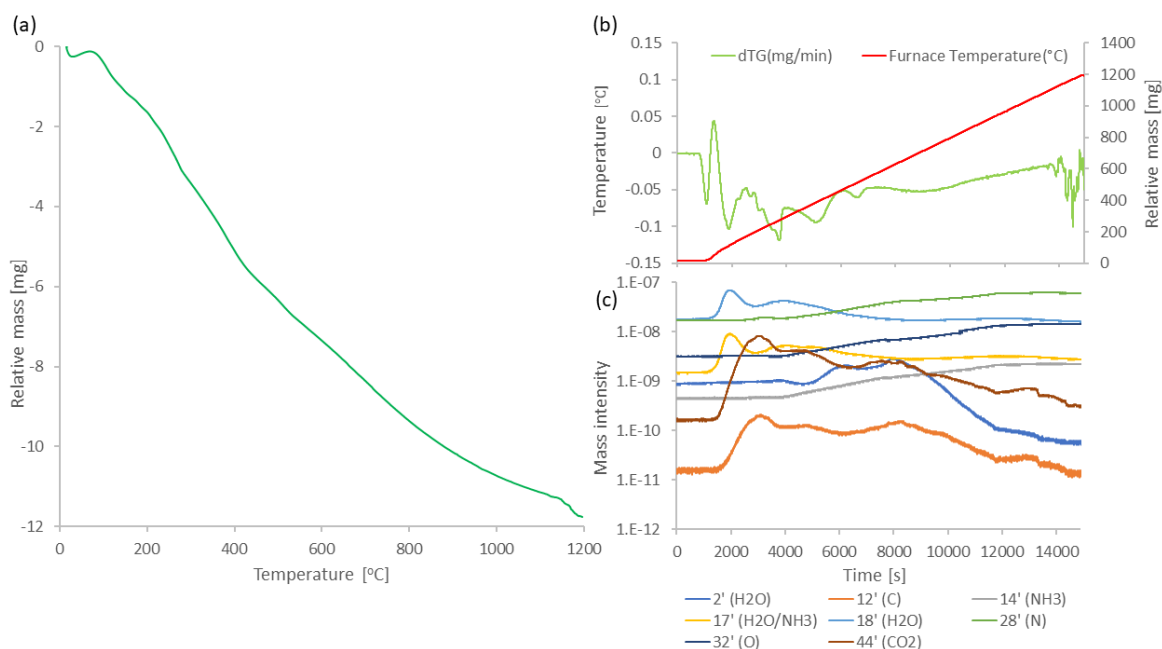


Figure 5.1: Simultaneous TGA and MS measurements performed on 20,78 mg Cu-THQ. (a) TGA, showing weight loss and furnace temperature, (b) TGA, showing weight loss derivative and furnace temperature and (c) mass spectroscopy of the gasses emitted during the TGA measurement.

To investigate the influence of carbonization of a 2D-MOF on their CO_2RR catalytic performance, Cu-THQ was carbonized. First, combined TGA and MS measurements were performed to gain more insight into the decomposition process of the THQ linker. Fast loss of mass in a TGA usually indicates some form of evaporation or reaction occurring. As can be seen in Figure 5.1, the peaks in the mass loss ratio all occur below 400 °C. The MS results in Figure 5.1c also show that most of the H_2O and CO_2 trapped in or attached to the MOF leave the material below 400 °C, suggesting that most of the linker decomposition occurs below this temperature. This is similar to the results as found by J. Lisha et al. [115], who showed that most of the mass loss in Cu-THQ occurred below 400 °C.

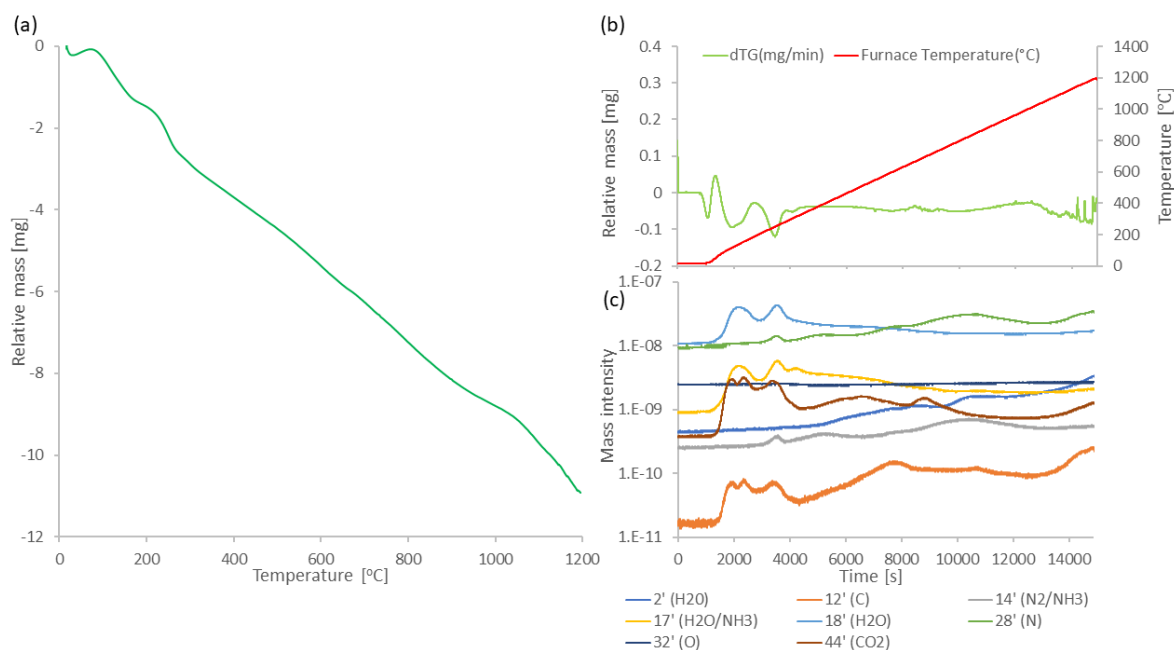


Figure 5.2: Results of simultaneous TGA and MS measurements performed on 15.68mg Cu-HAB. (a) TGA, showing weight loss and furnace temperature, (b) TGA, showing weight loss derivative and furnace temperature and (c) mass spectroscopy of the gasses emitted during the TGA measurement.

To further understand the effects of carbonization on CO_2RR catalytic capabilities of 2D-MOFs containing nitrogen, Cu-HAB was carbonized. Since nitrogen can be lost during carbonization at high temperatures, first a combined TGA and MS measurement was performed to gain insight into the linker decomposition process of Cu-HAB. As can be seen in Figure 5.2, the main peaks in the mass loss ratio all occur below 400 °C. Similarly as for Cu-THQ, it can be observed from the MS results that these peaks are mainly due to the evaporation of trapped water and other gasses like CO_2 and not nitrogen. In the same MS results, it can be seen that the slope of the amount of nitrogen being detected significantly decreases from about 550 °C and upwards. This was therefore deemed to be the temperature to carbonize Cu-HAB. In this way, carbonization occurs well above the linker decomposition and loss of attached hydrogen but low enough to retain most of the nitrogen.

Some large fluctuations also occur close to the peak temperature of 1200 °C for both materials. This can be attributed to the TGA machine adapting its heating rate in order to ensure enable the sharp transition from a constant heating rate to a constant cooling rate.

5.1.2. Surface Characterization

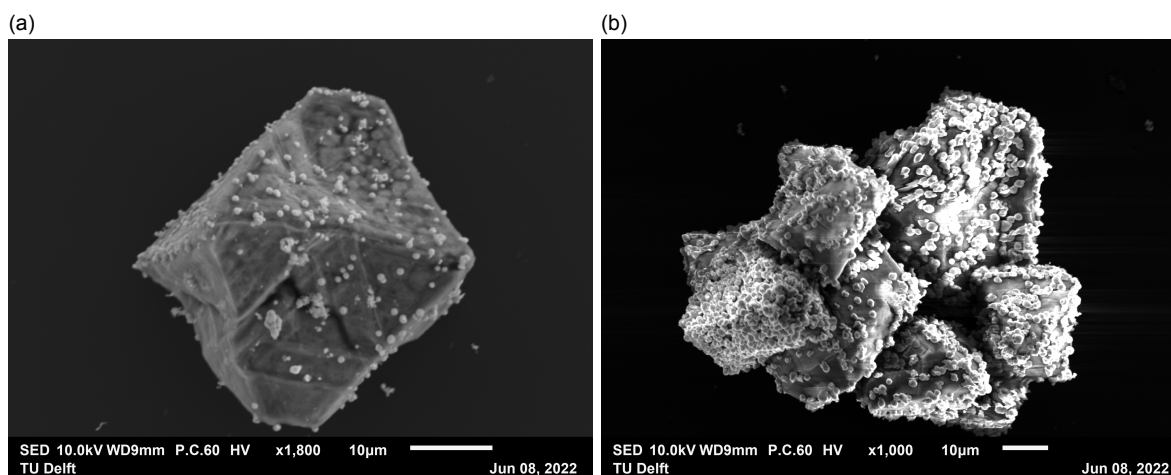


Figure 5.3: SEM images of carbonized Cu-BTC at 300 °C for 3 h in a tubular furnace under Ar atmosphere with a heating rate of 20 °C/min ($Cu@C - (BTC)_{300C}$). (a) particle containing a relatively low amount of Cu clusters and (b) particle containing a relatively high amount of Cu clusters.

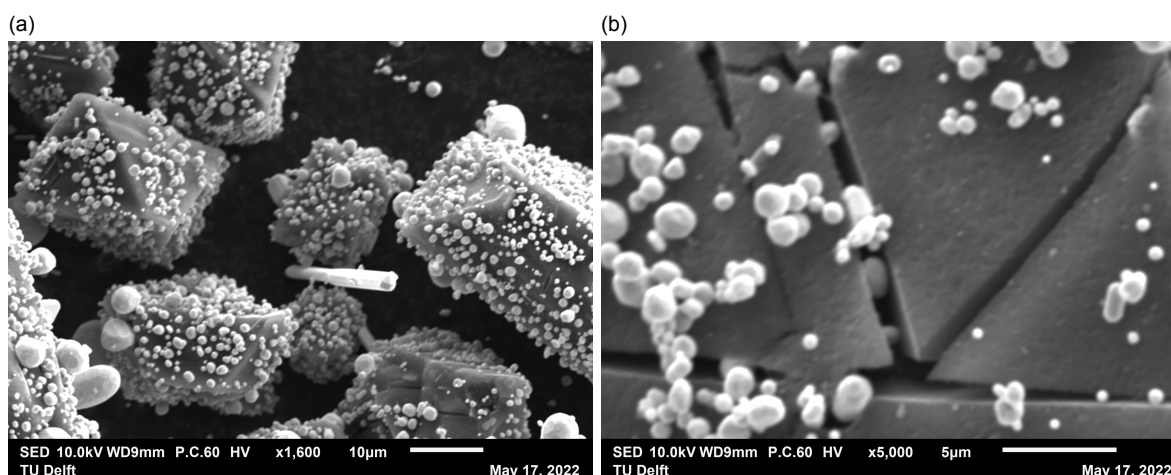


Figure 5.4: SEM images of Cu-BTC grains carbonized at 1000 °C for 6 h in a tubular furnace under Ar atmosphere with a heating rate of 5 °C/min ($Cu@C - (BTC)_{1000C}$). (a) overview of particles with Cu clusters and (b) surface of a particle with Cu clusters.

After carbonization SEM images for both $Cu@C - (BTC)_{300C}$ and $Cu@C - (BTC)_{1000C}$ were made in order to investigate changes in their morphology, which can be seen in Figures 5.3 and 5.4. Comparing these to the images for pristine Cu-BTC as seen

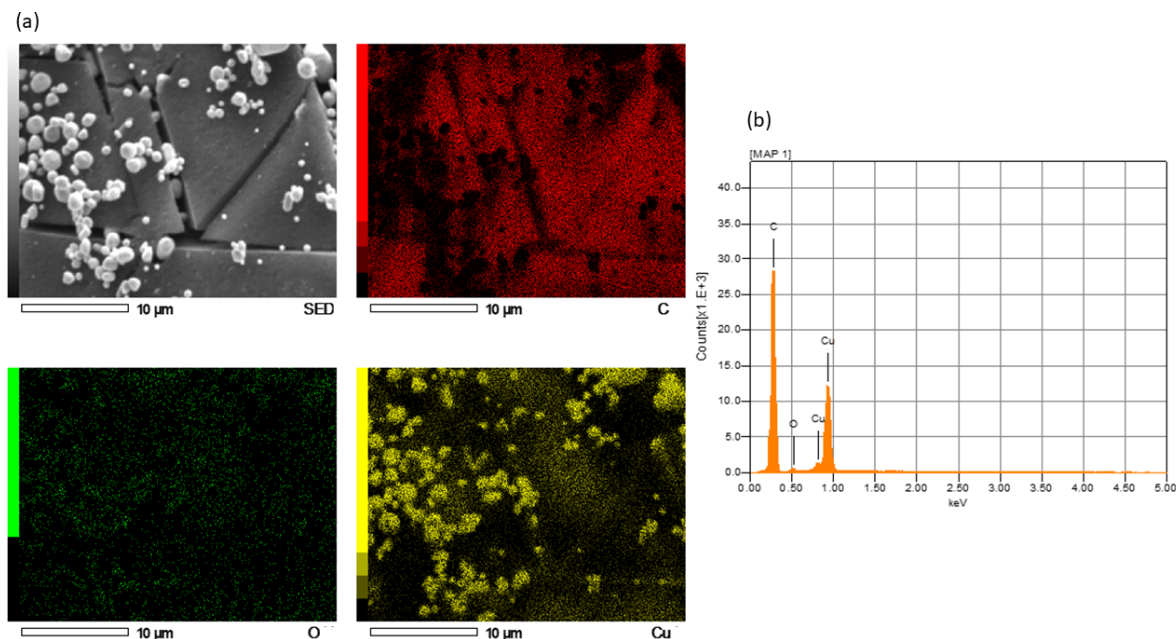


Figure 5.5: EDS analysis of the surface of a single $Cu@C - (BTC)_{1000C}$ particle. (a) mapping (b) spectrum.

in Figure 4.4, it can be observed that for both carbonization settings, white particles are formed on the surface of the framework crystal. Similar aggregation behavior was also observed in several other works, being identified as Cu-clusters [23, 78, 79]. The presence of large amounts of Cu in these particles was confirmed using the EDS analysis that can be seen in Figures 5.5 and 5.6.

EDS results also indicate the presence of more oxygen in $Cu@C - (BTC)_{300C}$ than in $Cu@C - (BTC)_{1000C}$. This is in line with the expectation that partial linker decomposition occurs in $Cu@C - (BTC)_{300C}$, resulting in a significant amount of oxygen remaining attached to the linkers. It is important to note that EDS is only semi-quantitative and thus no concrete conclusions can be made about the amount of oxygen left behind. However, the large difference in oxygen content between the two materials indicates that there is a difference in the amount of linker decomposition between the two materials.

As discussed before, the goal of using the SPS machine was to limit the growth of these Cu-clusters. $Cu@C - (BTC)_{500C-SPS}$ and $Cu@C - (BTC)_{650C-SPS}$ have significantly smaller Cu-clusters than $Cu@C - (BTC)_{1000C}$ and $Cu@C - (BTC)_{300C}$, as can be seen in Figures 5.7 and 5.8. In the former two materials, most grains contain only a small amount of clusters of about 500 nm in diameter. Compared to the 1-5 μm diameter Cu-particles which are present in much larger numbers in $Cu@C - (BTC)_{1000C}$ and $Cu@C - (BTC)_{300C}$, it can be concluded that the materials produced by SPS have a significantly lower amount of Cu-clusters.

The goal when making $Cu@C - (BTC)_{650C-SPS}$ was to make a MOF using the SPS

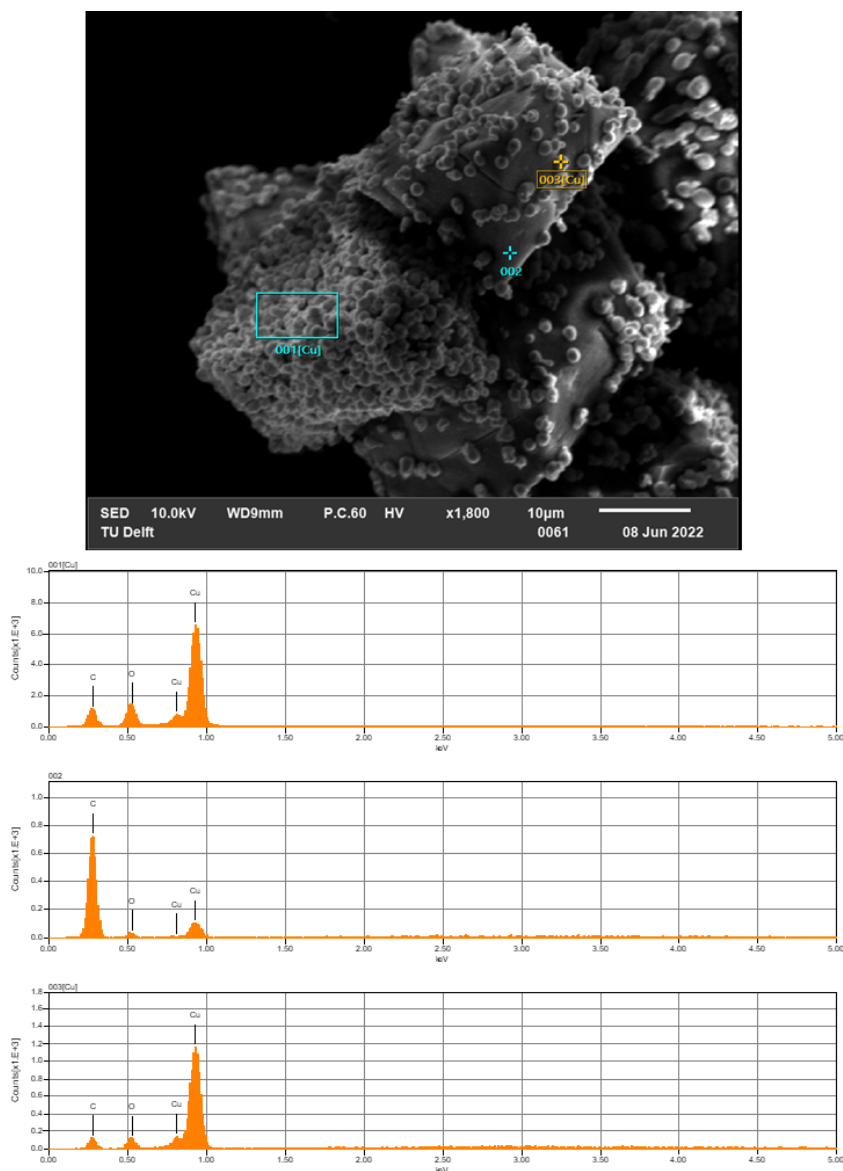


Figure 5.6: EDS analysis of $Cu@C - (BTC)_{300C}$ grain for 2 points and 1 area. Point 1 is positioned on a white cluster, point 2 on grain surface without white clusters, area 3 analyzes a region covered with white clusters. Corresponding atom% of these measurements can be found in Table 5.1.

Table 5.1: elemental composition of three different measurement points on $Cu@C - (BTC)_{300C}$ grains, obtained using EDS. Position and signal output graphs of the corresponding measurement points can be seen in Figure 5.6.

element	atom% area 1	atom% point 2	atom% point 3
C	46.19	91.30	42.00
O	22.17	5.07	13.27
Cu	42.00	3.63	44.72

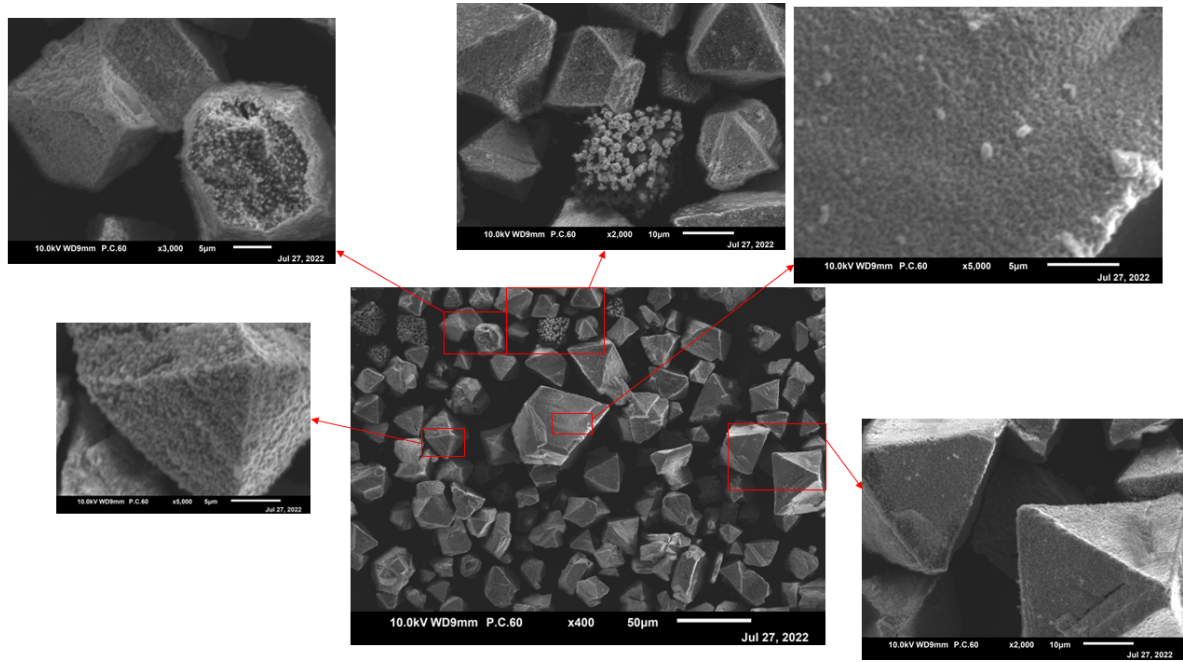


Figure 5.7: SEM images of $Cu@C - (BTC)_{500C-SPS}$.

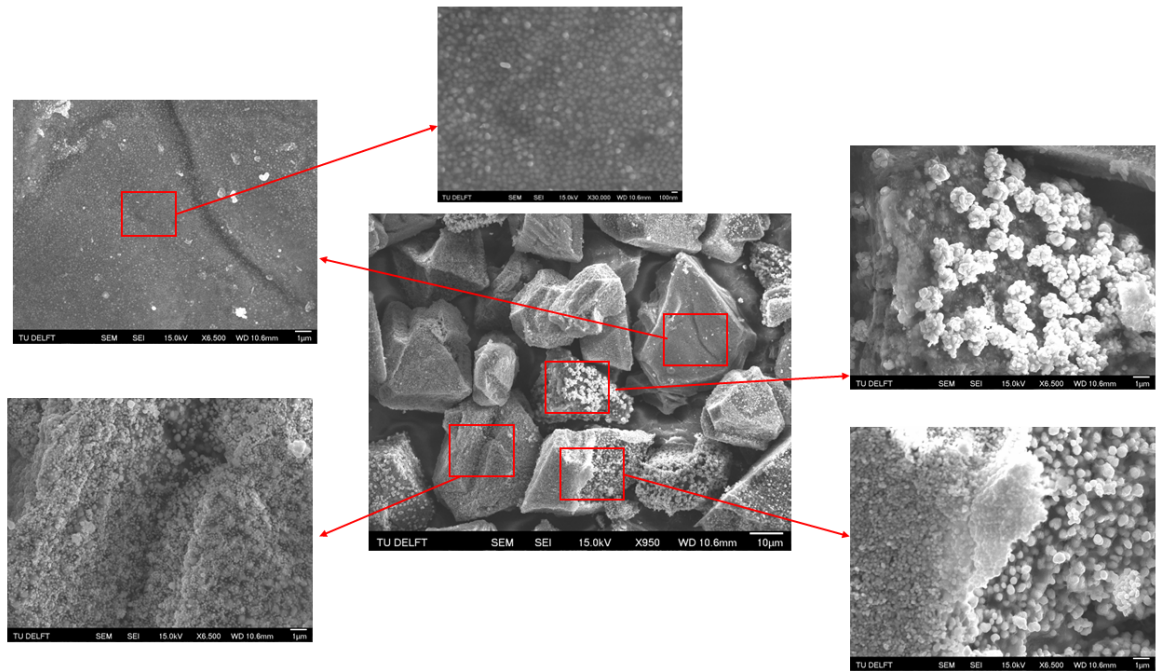


Figure 5.8: SEM images of $Cu@C - (BTC)_{650C-SPS}$.

machine which has better catalytic capabilities than $Cu@C - (BTC)_{500C-SPS}$, but which still has similar small Cu-clusters. Figures 5.7 and 5.8 show that the size of Cu-clusters in $Cu@C - (BTC)_{650C-SPS}$ is generally similar to that of $Cu@C - (BTC)_{500C-SPS}$, with the bulk of the grains in the former showing Cu-clusters similar in size and amount to the latter. Thus, the goal of maintaining a Cu-cluster growth similar to $Cu@C - (BTC)_{500C-SPS}$ was achieved.

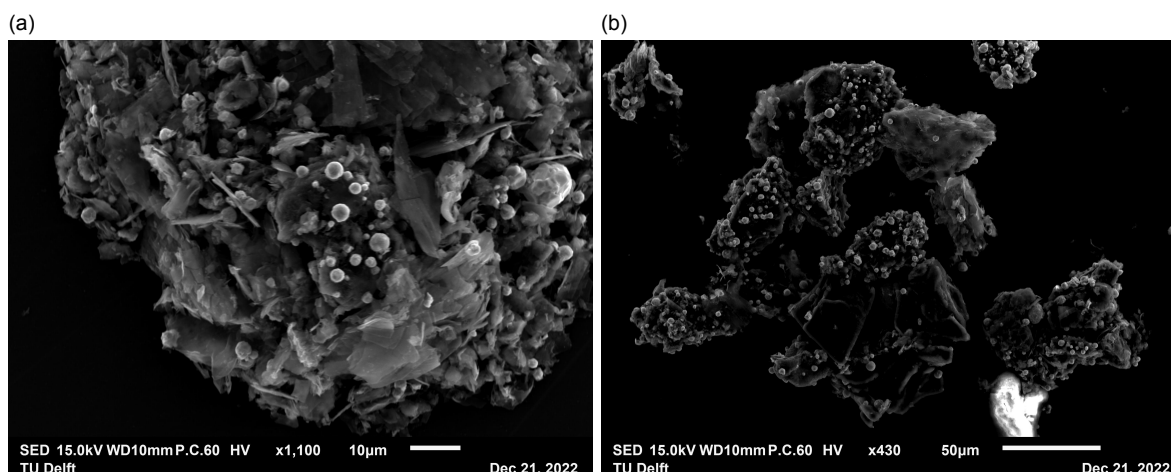


Figure 5.9: SEM images Cu-THQ at 1000 °C for 5 h in a tubular furnace under Ar atmosphere with a heating rate of 5 °C/min ($Cu@C - (THQ)_{1000C}$). (a) particle showing 2D-sheets and Cu-clusters and (b) overview of a number of grains clustered together.

It is interesting to note that there is a small amount of grains that do have a large number of Cu-clusters of about 2-3 μm in diameter. The reason for this is unknown, suspected causes are defects, Ar gas flow and dispersion (as outside grains get more heat). Another option is the SPS current flow goes through to powder particles in direct contact with the die, heating them more than those further away from the die.

After carbonization $Cu@C - (THQ)_{1000C}$ was investigated using SEM. In Figure 5.9 it can be observed that the beneficial sheetlike 2D-morphology is still present in the material. Besides, similar Cu-clusters as were found on carbonized Cu-BTC can be observed. Furthermore, more grains have clumped together creating larger agglomerations of grains, than before carbonization.

$Cu@C - (HAB)_{550C}$ morphology after carbonization was investigated using SEM. As can be seen in Figure 5.10, 2D-shape of the grains is retained. Some grains can be observed to have a rougher surface, but as shown in Figure 4.5 grains with both rougher and smoother surfaces were also present in the pristine material. The EDS analysis as can be seen in Figure 5.12 shows that there seems to be no significant difference in elemental composition between the different kinds of grains that are formed.

Cu-clusters as observed in a similar manner as in the other carbonized MOFs are not immediately observed. However, plate-like clusters can be observed to have grown on a number of grains. EDS analysis in Figure 5.11 shows that these plate-like clusters have a significantly larger Cu-content than the underlying grain. It can be seen in Figure 5.12 that the Cu-content is also significantly higher than grains without these plate-like clusters. The reason behind the formation of these plate-like clusters can be due to the nitrogen within the material. As the remaining nitrogen may have been able to form bonds between the carbon and the copper, making it easier for the Cu to cluster together on the surface of the MOF. These plate-like structures allow for

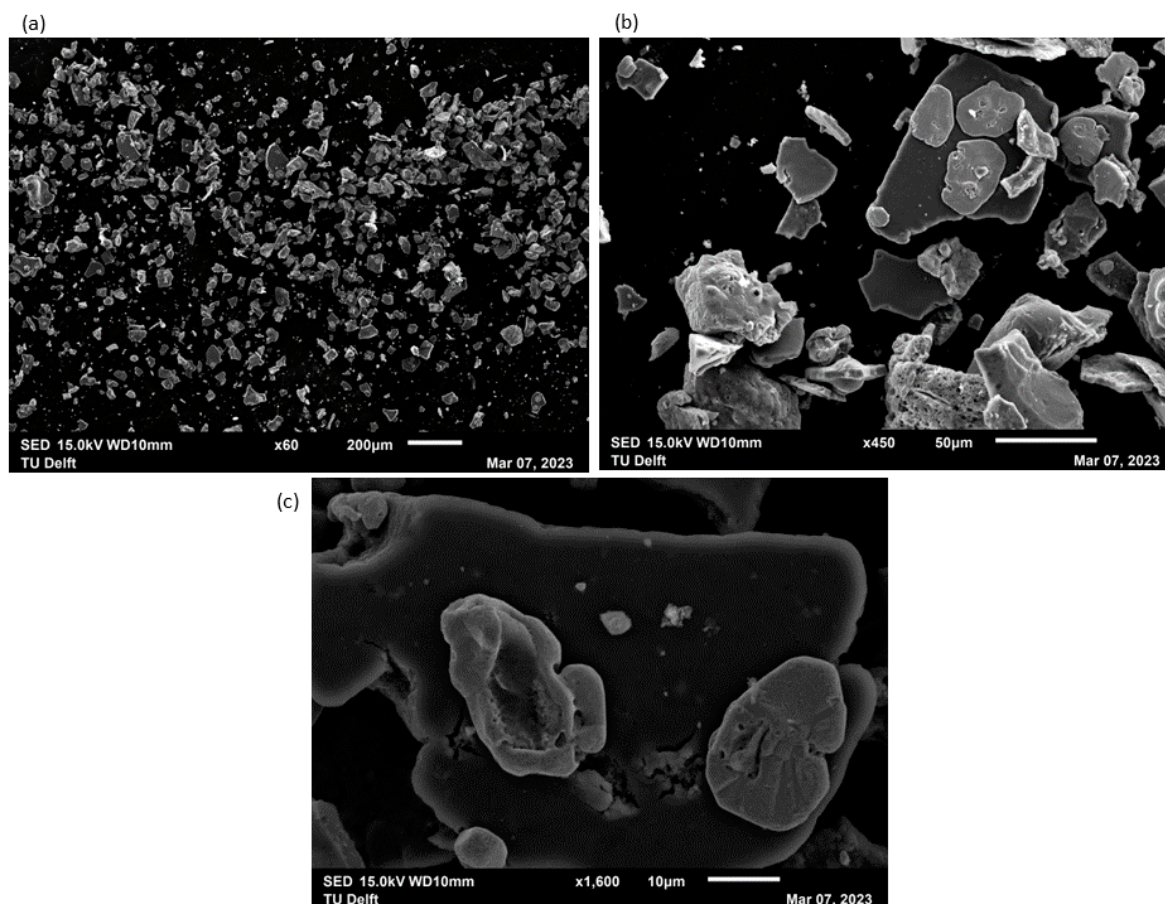


Figure 5.10: SEM images Cu-HAB at 550 °C for 6 h in a tubular furnace under Ar atmosphere with a heating rate of 5 °C/min ($Cu@C - (HAB)_550C$). (a) overview of a larger number of particles. (b) Some of the average particles formed shown together. (c) close-up of a single 2D-grain.

a much larger surfaces area to volume ratio than round Cu-clusters would achieve. This means that the loss of catalytic surface area due to these plate-like formations may be lower than for the round Cu-clusters as formed in the other carbonized MOFs. Furthermore, the shape of nano-particles can have an influence on selectivity during catalytic processes by for example exposing certain reactive facets [116, 117].

Figure 5.12 also shows that in all grains there is between 14 and 20 atom% nitrogen left behind in the material. As Yu Bi [85] found 30 atom% nitrogen in the pristine material using EDS, this means that more than 50 % of the nitrogen in the material is maintained after carbonization.

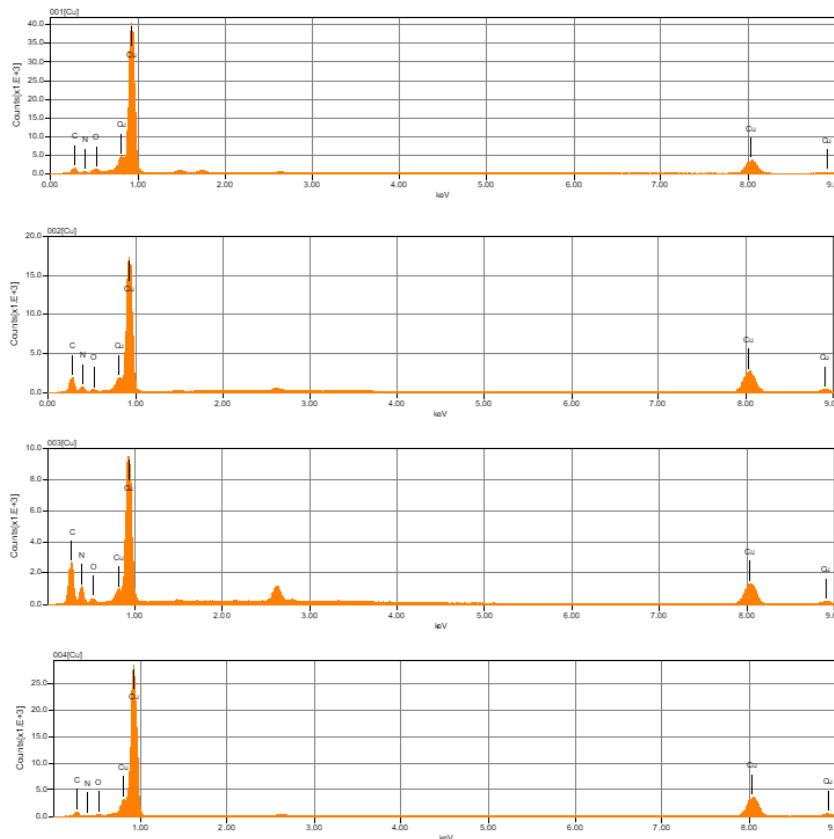
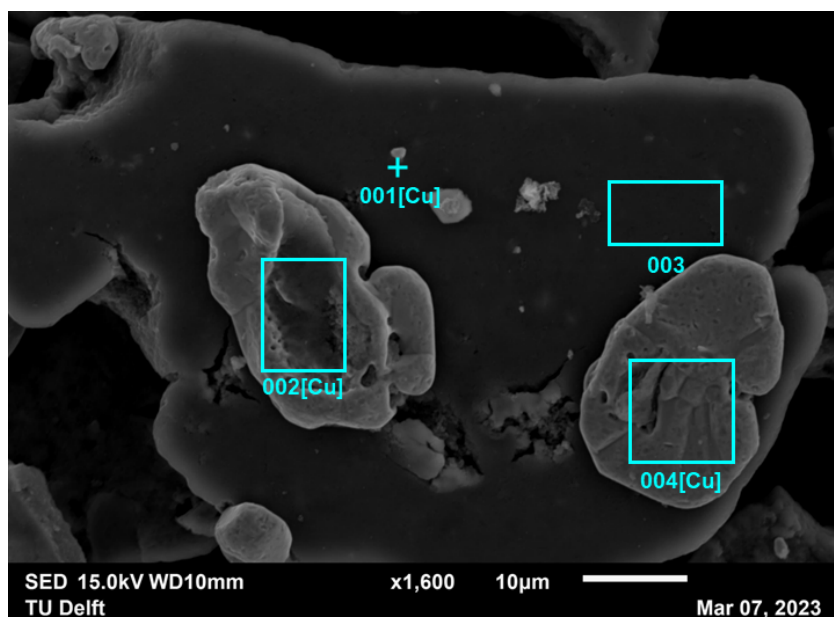


Figure 5.11: EDS analysis of $Cu@C - (HAB)_{550C}$ grain for 1 point and 3 areas. point 1 is placed upon a suspected Cu-cluster. Area 2 on a flat particle on top of the main grain. Area 3 is positioned on part of the grain itself. Area 4 is positioned on a flat particle on top of the grain. Corresponding atom% of these measurements can be found in Table 5.2.

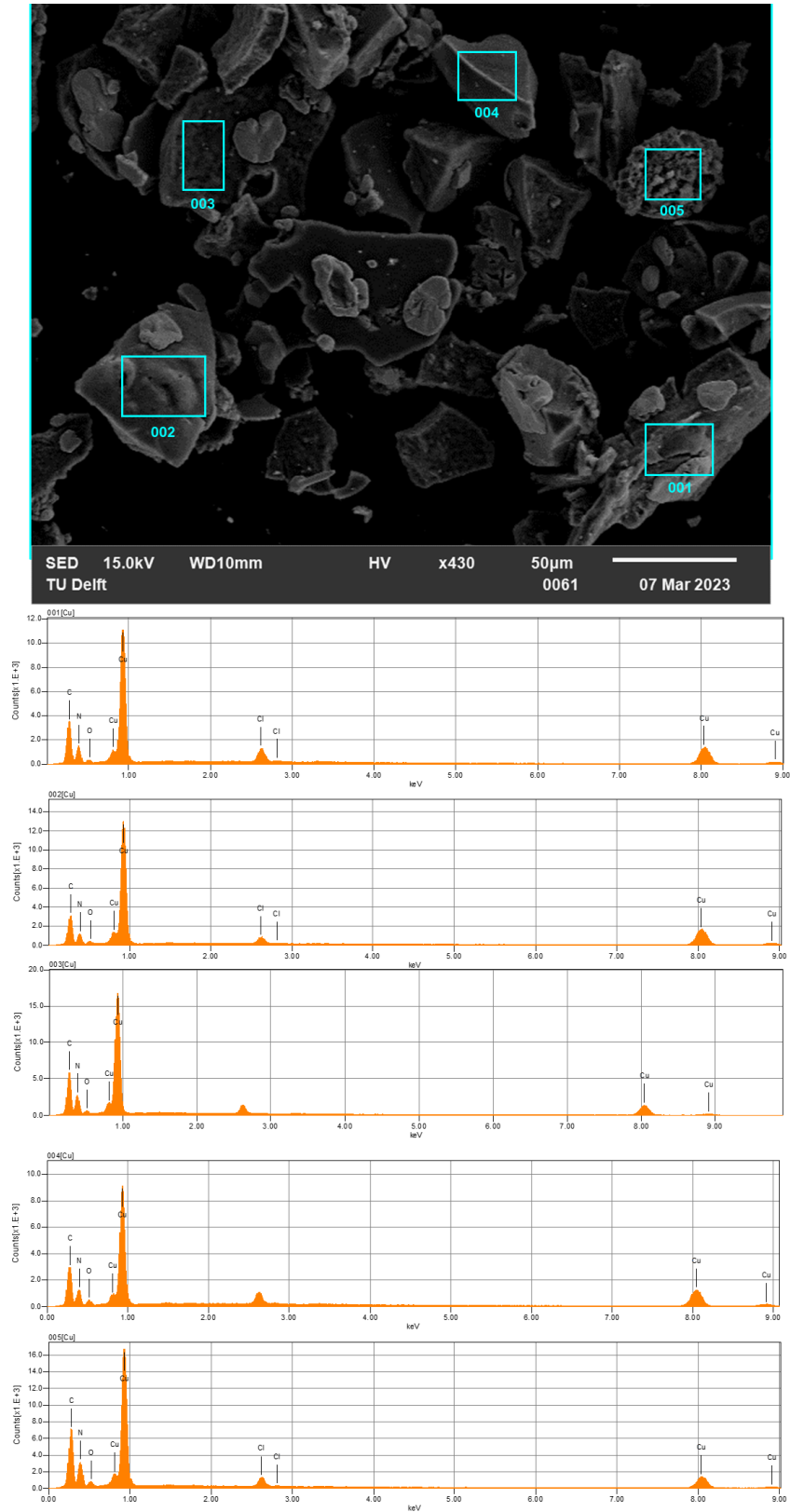


Figure 5.12: EDS analysis of multiple $Cu@C - (HAB)_{550C}$ grains. each of the 5 areas represents a single sort of grain found in the material. Corresponding atom% of these measurements can be found in Table 5.3.

Table 5.2: Elemental composition at 5 different measurement points or areas on the surface of a single $Cu@C - (HAB)_{550C}$ grain, which can be seen in Figure 5.11. Obtained using EDS.

element	atom% point 1	atom% area 2	atom% area 3	atom% area 4
C	30.23	40.96	56.52	20.89
N	6.42	11.13	16.40	4.02
O	4.65	1.75	2.77	1.22
Cu	58.70	46.16	24.32	73.86

Table 5.3: Elemental composition of 5 different measurement areas representing 5 different $Cu@C - (HAB)_{550C}$ grains, which can be seen in Figure 5.12. Obtained using EDS.

element	atom% area 1	atom% area 2	atom% area 3	atom% area 4	atom% area 5
C	60.17	57.01	62.62	58.26	64.43
N	16.79	14.50	20.00	16.39	19.16
O	1.85	1.91	2.53	3.47	3.19
Cl	1.96	1.24	1.40	1.78	1.13
Cu	19.22	25.34	13.45	20.11	12.09

5.2. Electrochemical Measurements

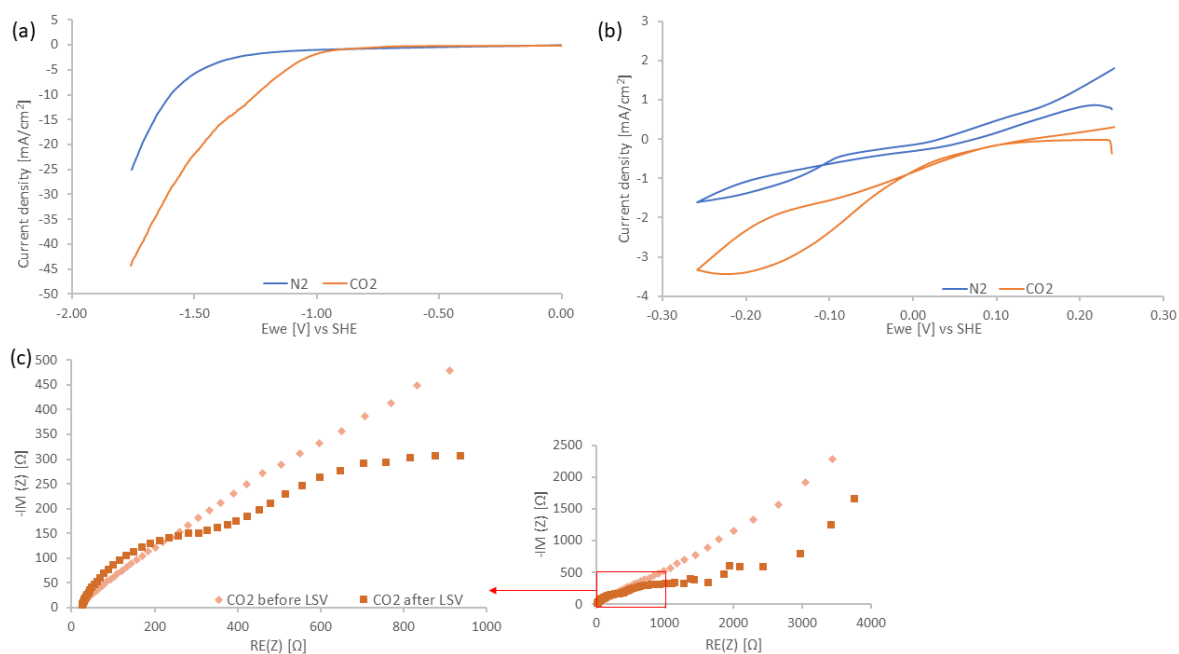


Figure 5.13: (a) LSV figure, (b) CV and (c) EIS measurements for $Cu@C - (BTC)_{300C}$ in a one container electrochemical cell containing 1 M $KHCO_3$.

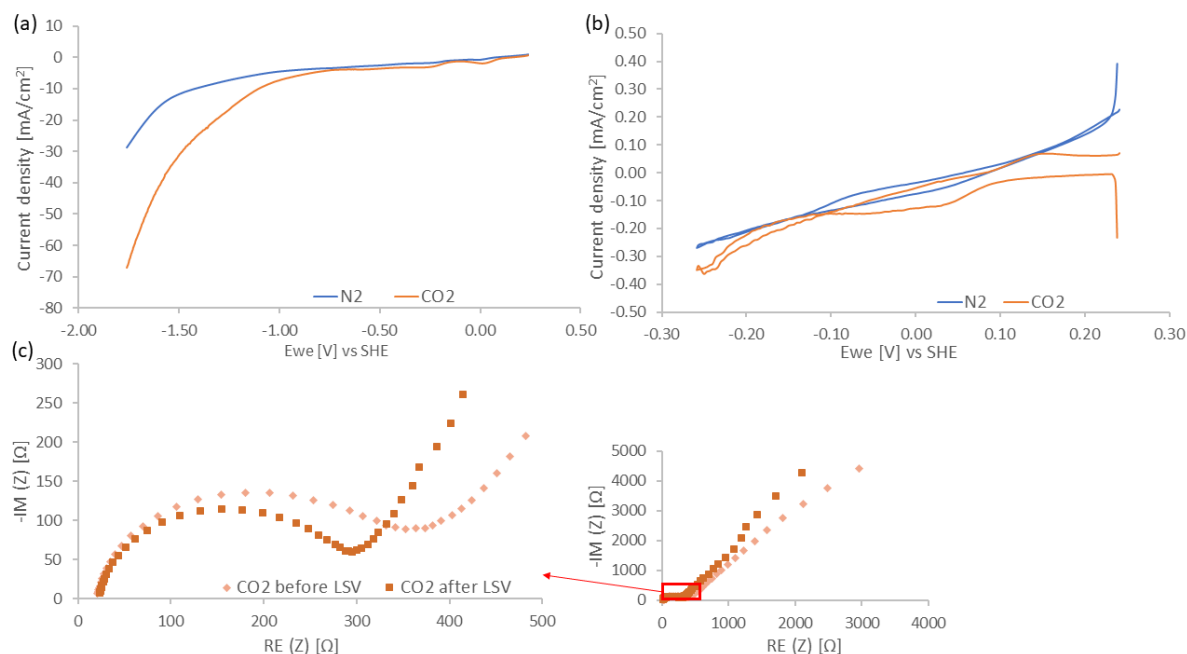


Figure 5.14: (a) LSV, (b) CV and (c) EIS measurements for $Cu@C - (BTC)_{1000C}$ conducted in a one container electrochemical cell containing 1 M $KHCO_3$.

To further understand the differences in the catalytic performance of the carbonized MOFs, varying electrochemical experiments were performed.

As can be seen in Figures 5.13a and 5.14a, the LSV curves for both $Cu@C - (BTC)_{300C}$ and $Cu@C - (BTC)_{1000C}$ have a lower onset potential in CO_2 saturated electrolyte than in N_2 saturated electrolyte. Since the onset potential for hydrogen production is higher than for most CO_2RR products, this indicates activity towards CO_2RR . In addition to this, a clear increase in current density when performed in CO_2 saturated electrolyte can be observed. Since the current density in N_2 saturated electrolyte can only be caused by hydrogen evolution reaction (HER), the additional current density achieved in CO_2 saturated electrolyte is due to CO_2RR activity. Thus, both materials show signs of activity towards CO_2 reduction [118, 119].

Figure 5.15a shows that the gap between the current density in CO_2 saturated electrolyte and N_2 saturated electrolyte is the relatively smaller amount of $5 mA/cm^2$ for the $Cu@C - (BTC)_{500C-SPS}$ electrode. This can indicate that this material has a lower affinity for CO_2RR than the previous two. However, the current density remains higher in CO_2 saturated electrolyte while the onset potential remains lower. This indicates that there still is some affinity for CO_2RR .

For $Cu@C - (BTC)_{650C-SPS}$ both current densities and onset potentials are very similar. This could indicate that most of this material mainly has activity towards HER instead of CO_2RR . It is important to note that some of the LSV measurements for $Cu@C - (BTC)_{650C-SPS}$, which can be seen in appendix B Figure B.1, did show more current density in CO_2 saturated electrolyte than in N_2 saturated electrolyte. Although

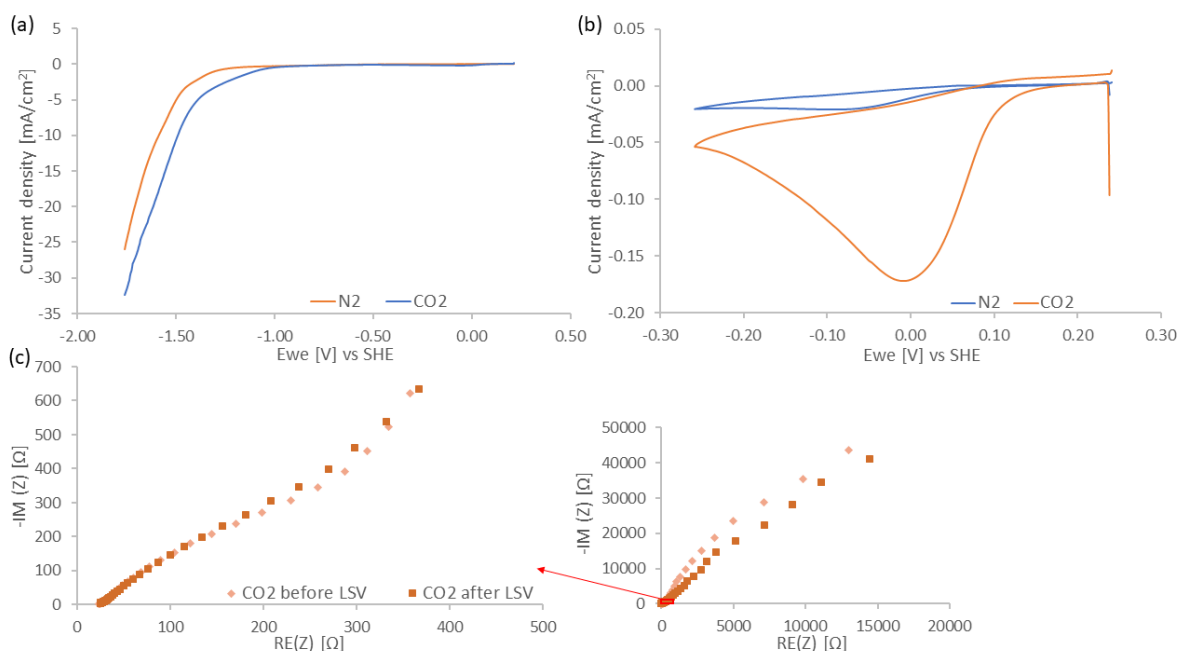


Figure 5.15: (a) LSV, (b) CV and (c) EIS measurements for $Cu@C - (BTC)_{500C-SPS}$. conducted in a one container electrochemical cell containing 1 M $KHCO_3$.

these measurements reached lower potentials overall, the fact that they show a difference means that there can be potential for $Cu@C - (BTC)_{650C-SPS}$ to perform CO_2RR .

Aside from showing an increased activity in CO_2 saturated electrolyte, suggesting their activity as CO_2RR catalysts, the CV-curves for $Cu@C - (BTC)_{300C}$ and $Cu@C - (BTC)_{1000C}$ in Figures 5.13b and 5.14b reveal no new information. The CV-curves for $Cu@C - (BTC)_{500C-SPS}$ and $Cu@C - (BTC)_{650C-SPS}$ show a clear increase in current density around 0 V vs SHE. This can be linked to ethane or ethanol production, which have a half reaction potential of 0.06 V vs SHE and 0.08 V vs SHE respectively. On the return sweep this same increase did not occur, showing that the increase was due to a non-reversible reaction [118]. Since most CO_2RR products leave the catalyst surface after reacting, these reactions behave as non-reversible reactions. Thus, the non-reversibility suggests that the current density increase is indeed caused by a CO_2RR reaction product. The affinity for ethane or ethanol production of $Cu@C - (BTC)_{650C-SPS}$ further enforces that this material is still suitable for CO_2RR even though its LSV results give less indication of this.

EIS measurements were performed in order to gain insights into the charge transport resistance of the electrochemical systems. A fast charge transfer reaction at a planar electrode like CO_2RR is expected to behave like a Randles equivalent circuit [118]. Both this circuit and the shape of the resulting EIS curve can be seen in Figure 4.13. The EIS graphs of all four of the materials are similar to this curve as can be seen in Figure 5.13c, 5.14c, 5.14c and 5.15c. As this means they behave as expected of a CO_2RR system, they are eligible for further use in obtaining resulting parameters.

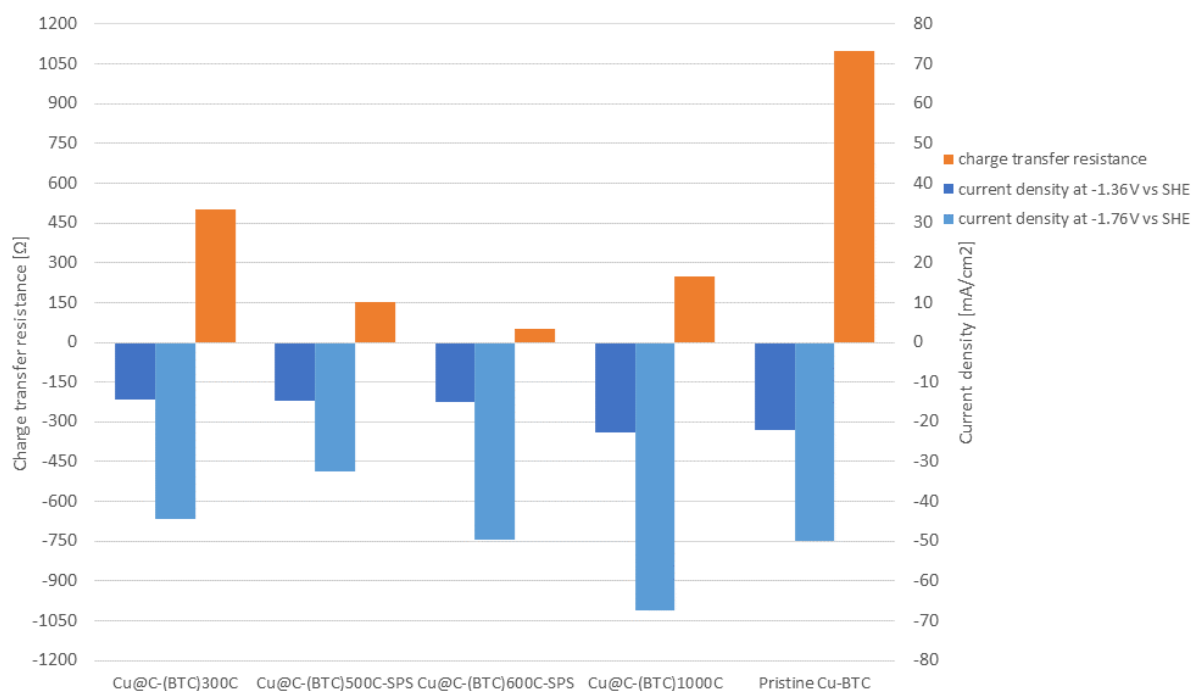


Figure 5.16: Comparison of the most important parameters of all the different versions of carbonized Cu-BTC used in this study, pristine Cu-BTC data as obtained by Yu Bi [85] was also included.

Figure 5.16 shows an overview of the most important results obtained from the EC data. The current densities are given at -1.36 V vs SHE and -1.76 V vs SHE. -1.36 V vs SHE is the voltage at which the products generated by the different materials will be investigated. The current density at this voltage can be used as an indication of the production rates that can be expected during these tests [105]. The highest achieved current densities are also included, as the current density range for the measured voltage range can be used as an indication of the number of active sites in the material. Finally, the charge transfer resistance obtained from the EIS curves is shown. As a lower charge transfer resistance allows electrons to be supplied to reactants more quickly, indicating potential for higher reaction rates [118].

Figure 5.16 shows that all carbonized Cu-BTC materials have a significantly lower charge transfer resistance compared to the pristine material. This is in accordance with the expectation that carbonization will improve the conductivity of the material, which in turn lowers the charge transfer resistance [120, 121].

It was expected that higher holding temperatures lead to more complete decomposition of the linkers. Entirely decomposed linkers exist out of pure carbon, which results in higher conductivity for the MOF-derived material. This higher conductivity then leads to a lower lowering charge transfer resistance. Thus, $Cu@C - (BTC)_{1000C}$ having a lower charge transfer resistance than $Cu@C - (BTC)_{300C}$ is in line with the expectation that the former should have a higher conductivity than the latter.

The charge transfer resistance of the materials produced with the SPS machine can be observed to be lower than the charge transfer resistance of the other materi-

als. This can be due to them having smaller Cu-clusters leading to a larger catalytic-surface area and thus lower charge transfer resistance [122].

$Cu@C-(BTC)_{1000C}$ achieves significantly higher current densities and lower charge transfer resistance compared to $Cu@C-(BTC)_{300C}$. This indicates that the CO_2RR performance of $Cu@C-(BTC)_{1000C}$ is expected to be better than that of $Cu@C-(BTC)_{300C}$. This suggests that full carbonization is more beneficial than partial carbonization for the catalytic capabilities of CO_2RR .

$Cu@C-(BTC)_{650C-SPS}$ was an attempt to improve $Cu@C-(BTC)_{500C-SPS}$. As can be seen, their results are similar with a main difference in current densities. $Cu@C-(BTC)_{650C-SPS}$ appears to have higher current densities at -1.76 V vs SHE. Thus, $Cu@C-(BTC)_{650C-SPS}$ was perceived to be better as a CO_2RR catalyst than $Cu@C-(BTC)_{500C-SPS}$.

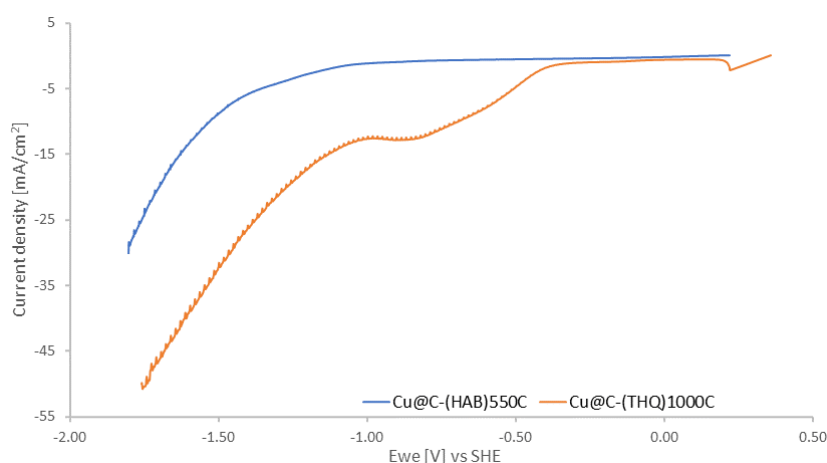


Figure 5.17: LSV measurements of the carbonized 2D-MOFs: $Cu@C-(THQ)_{1000C}$ and $Cu@C-(HAB)_{550C}$. Both LSV measurements were performed in a dual chamber flow cell, under 10 mL/min CO_2 gas flow, containing 1 M $KHCO_3$ electrolyte.

To further analyze the catalytic indications of the MOF-derived materials, it is important to measure their selectivity and production rates towards CO_2RR . $Cu@C-(BTC)_{1000C}$ was selected for this, due to its relatively high current densities and low charge transfer resistance compared to pristine Cu-BTC. $Cu@C-(BTC)_{650C-SPS}$ was also selected as it exhibits the lowest charge transfer resistance, as well as having the highest current densities out of the two materials created using SPS.

To gain further insights into the CO_2RR catalytic capabilities of 2D-MOF derived materials, LSV measurements were performed for both $Cu@C-(THQ)_{1000C}$ and $Cu@C-(HAB)_{550C}$. Figure 5.17 shows that of these two materials, Cu-THQ achieves the higher current density of $-50 mA/cm^2$ at -1.76 V vs SHE. This is a similar current density achieved by $Cu@C-(BTC)_{650C-SPS}$ and pristine Cu-BTC as can be seen in Figure 5.16. Besides, Figure $Cu@C-(THQ)_{1000C}$ shows a sudden increase in current between -0.50 V vs SHE and -1.00 V vs SHE, whereas Figure $Cu@C-(HAB)_{550C}$ does not. This current increase can be attributed to the production of formate, which

is produced at -0.61 V vs SHE. These LSV curves indicate that $Cu@C - (THQ)_{1000C}$ seems more suitable than $Cu@C - (HAB)_{550C}$ as a CO_2RR catalyst.

5.3. Reaction Products

To further understand the catalytic selectivity, potential CO_2RR products created at -1.36 V vs SHE using $Cu@C - (BTC)_{650C-SPS}$, $Cu@C - (BTC)_{1000C}$, $Cu@C - (THQ)_{1000C}$ and $Cu@C - (HAB)_{550C}$ catalysts were investigated. The voltage required for this product generation was applied by performing an amperometric measurement for 1 hour. This also allowed the current through the system to be measured. A representative curve showing such an amperometric measurement can be seen in Figure 5.18 for each respective material. It can be observed that all of the materials experience an increase of current density over time during the CO_2RR . A decrease in current density over time would indicate poor stability of the material. However, a slight increase in current density shows that the materials remain functional catalysts for at least 1 hour.

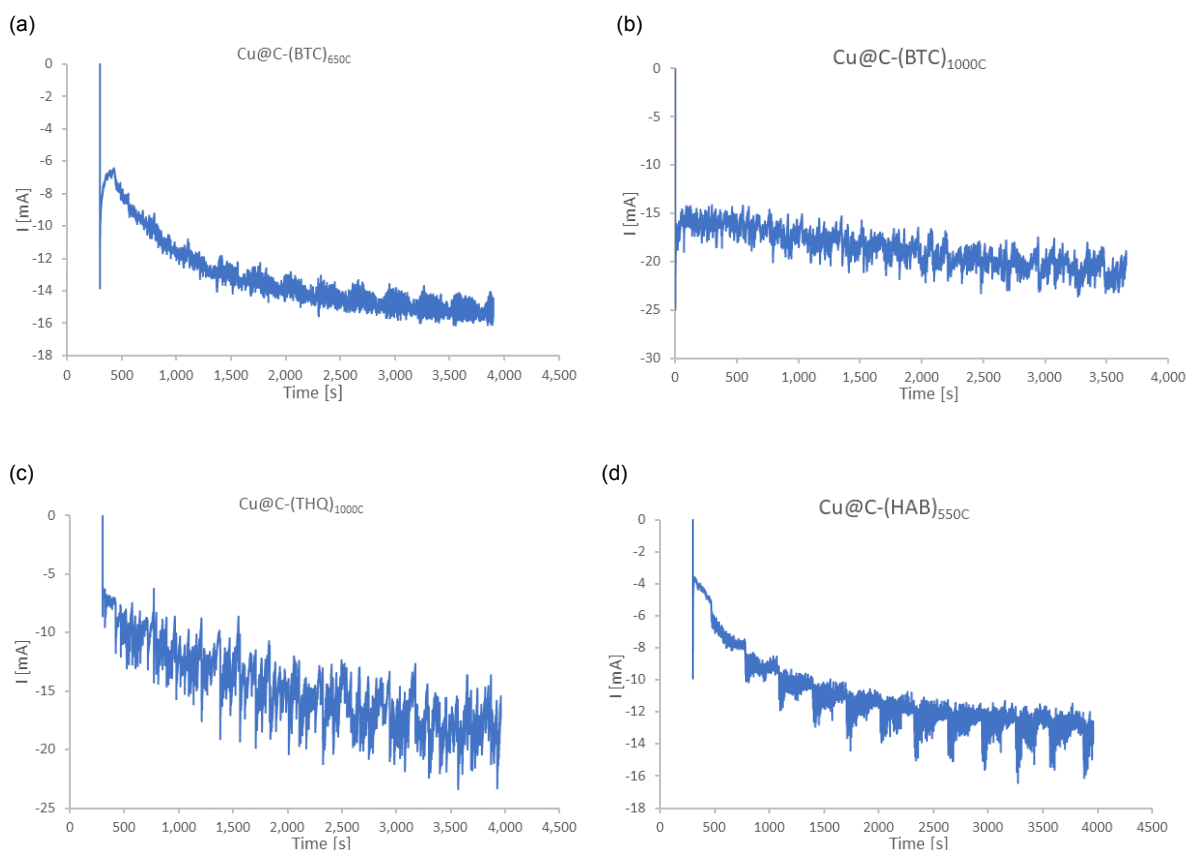


Figure 5.18: One hour CA measurements performed in a dual chamber flow cell, containing 1 M $KHCO_3$ electrolyte under constant 10 mL/min CO_2 gas flow. (a) $Cu@C - (BTC)_{650C-SPS}$, (b) $Cu@C - (BTC)_{1000C}$, (c) $Cu@C - (THQ)_{1000C}$, (d) $Cu@C - (HAB)_{550C}$.

The gas products produced during these CA measurements were measured during the experiment using GC, whereas the liquid products were extracted afterward

and measured using HPLC. The resulting FEs and partial current densities can be seen in Figure 5.19.

A baseline measurement was performed using a catalyst made by drop casting 95 wt% PTFE and 5 wt% carbon black soluted in 2.5 mL water and 2.5 mL isopropanol on a glassy carbon substrate. This was done to be able to differentiate gas products created by the active material from gasses present in the CO_2 gas supplied to the system and gas products made by the ink and substrate. The resulting GC spectra can be seen in Appendix B Figure B.8. To show the difference with the GC spectra of an experiment in which active material is used as the catalyst, the GC spectra of a single $Cu@C - (THQ)_{1000C}$ measurement are included in Appendix B Figure B.9.

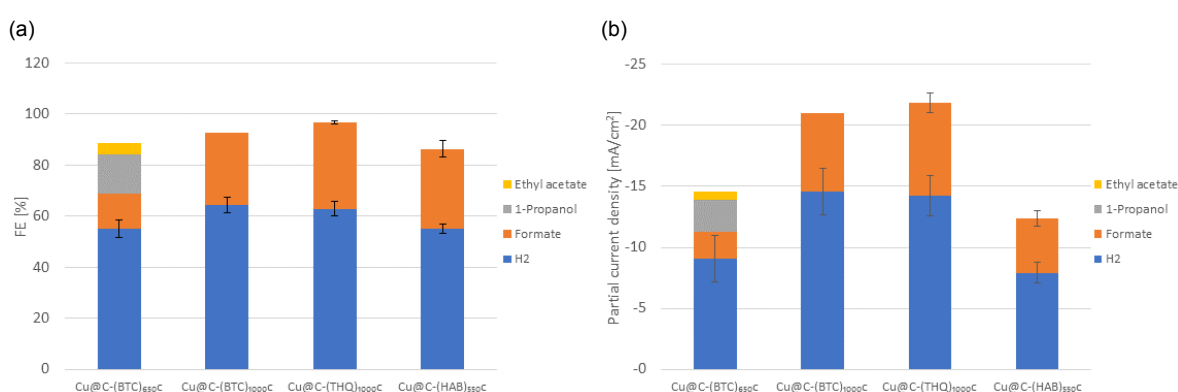


Figure 5.19: Products created at an applied potential of -1.36 V vs SHE. H₂, formate, 1-propanol and ethyl acetate data was found using GC, formate, NMR and NMR respectively. (a) Overview of the faradaic efficiencies for different catalyst materials. (b) Partial current densities for different catalyst materials.

First, it can be noted that most of the materials perform selectively towards formate production. $Cu@C-(BTC)_{1000C}$, $Cu@C-(THQ)_{1000C}$ and $Cu@C-(HAB)_{550C}$ reached FEs of around 30 % with only $Cu@C-(BTC)_{650C-SPS}$ having a lower FE for formate of 14 %. It is worth mentioning that the pristine materials have not been reported to be particularly selective for formate. Pristine Cu-BTC has been reported to mainly produce oxalic acid [123]. Pristine Cu-HAB was shown by Yu Bi [85] to not produce any formate using the same setup as used in this report. Cu-THQ has been shown to have some capability for production of formate by J. Lisha et al [115]. However, they found a FE of less than 10 % for formate at -0.5 V vs RHE with a total current density of 4 mA/cm^2 . As they applied a lower voltage and used 0.1 M $NaHCO_3$ as electrolyte instead 1 M $KHCO_3$ this could have an impact on their lower selectivity.

The answer to this may lay in the formation of the Cu-clusters, as $Cu@C-(BTC)_{650C-SPS}$ was the only one of these materials with lower amounts of cluster generated. However, it is well known that bulk copper tends to generate varying different products and is thus not considered selective [124]. Therefore, it can be said that copper clusters derived from a MOF can lead to selective catalysis toward the production of formate. This was also seen in a study by Mun Kyong Kim et al. [125], nano-sized Cu-clusters

were synthesized from Cu-MOFs using electroreduction methods. These synthesized Cu-clusters were used as CO_2RR catalysts resulting in significantly more selectivity towards CH_4 production than for commercial Cu-nanoparticles. This was attributed to an increased distance between the MOF derived Cu-clusters in comparison to the commercially obtained Cu-nanoparticles. It was speculated that this increase in distance suppressed C-C coupling leading to the formation of CH_4 instead of C_2H_4 . As there is significant distance between the Cu-clusters formed on the MOF in the case of the present study it is possible that similar suppression has happened towards the formation of C_2 -products. The CV curves of both materials without large Cu-clusters ($Cu@C - (BTC)_{500C-SPS}$ and $Cu@C - (BTC)_{650C-SPS}$) indicate an affinity for the multi-carbon products ethane and ethanol at around 0.06 V vs SHE and 0.08 V vs SHE respectively. While the CV curves for the materials which did form large Cu-clusters ($Cu@C - (BTC)_{300C}$ and $Cu@C - (BTC)_{1000C}$) do not show this affinity for methanol production. This is in line with the theory that the Cu-nanoparticles in combination with the carbonized MOF, support the desorption of intermediates leading to the formation of formate over methanol.

Although this excludes C_2 -products, there still needs to be a reason behind the generation of formate as the main product over other C_1 -products. One of the proposed pathways for methanol production is the progressive hydrogenation of the $HCOO^*$ intermediate [126, 127]. An overview of this pathway can be seen in Figure 5.20. F. Jiang et al. [128] found that the size of Cu-nanoparticles influences their affinity for a certain reaction pathway. Smaller Cu particles promote CO formation via the $*COOH$ pathway, whereas the $HCOO^*$ pathway becomes more favorable for larger particles. This is mainly attributed to the stronger and more present H-Cu bond on smaller Cu particles. This could explain why $Cu@C - (BTC)_{1000C}$ and $Cu@C - (THQ)_{1000C}$ have increased affinity for the $HCOO^*$ pathway, as both of these materials contained larger Cu clusters. $Cu@C - (BTC)_{650C-SPS}$ had a lot smaller Cu-clusters leading to a significantly lower FE for formate produced via the $*HCOO$ intermediate. Instead, the $*COOH$ intermediate could be promoted more, leading to the formation of a number of different products.

The reason why this pathway did not result in methanol formation, in this case, may be related to the adsorption of the intermediates to the Cu surface. The desorption of $HCOO^*$ is the rate-limiting step in the creation of formate on Cu surfaces [129]. J.J.Wang et al. [130] showed this by embedding Cu-nanoparticles into 2D-pyrenyl-graphdiyne, enabling electron exchange with the Cu-nanoparticles. This allowed for easier desorption of $HCOO^*$ leading to a FE of 95 % for formate production of 95 %.

This can explain why formate is produced by the materials which formed significant Cu-particles in this study. The distance between the particles enabled the selection of C_1 -products over C_2 -products. The larger size of the Cu-particles limits the $*COOH$ pathway and thereby the formation of CO, which leaves room for $HCOO^*$ intermediates to form. Due to the fact that Cu-particles are attached to the pure carbon MOF, this allows for electron exchange which enables easy desorption of the $HCOO^*$ intermediates resulting in formate production. However, this theory requires further

investigation and confirmation.

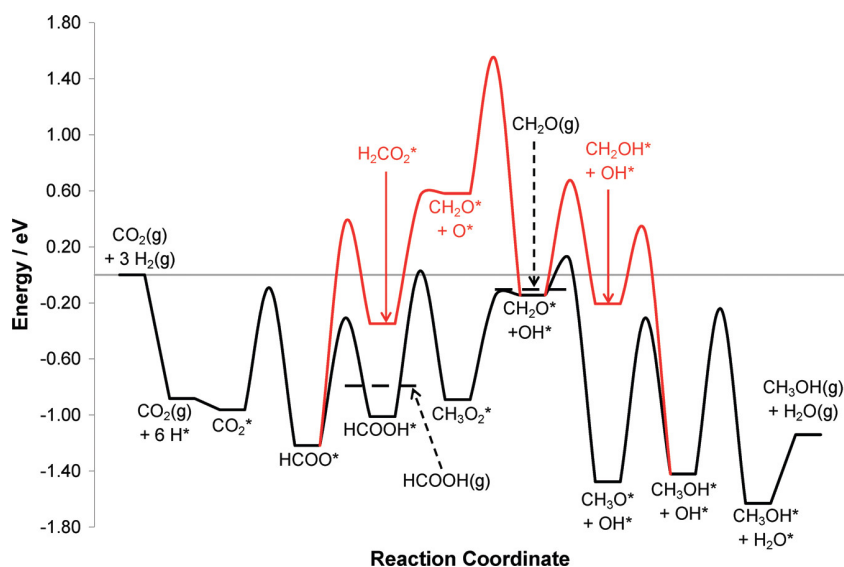


Figure 5.20: The energy levels involved in the pathway for methanol creation via the HCOO^* intermediate. It also shows the nearby energy level for formate production. Reproduced from [126].

Figure 5.19b shows that the Materials which combine good selectivity for formate with high current densities are $\text{Cu}@C - (\text{BTC})_{1000C}$ and $\text{Cu}@C - (\text{THQ})_{1000C}$. Since both of these materials were carbonized using the same parameters, this suggests that the carbonization parameters are more influential than the MOF structure. Besides their good performance, both the FEs and the partial current densities of these materials are very similar. This combined with the SEM results showing that both of these materials had similarly sized Cu-clusters further suggests that the Cu-clusters are the key factor influencing the selectivity and production rate of the MOF-derived catalysts.

Since 31 % of the FE of $\text{Cu}@C - (\text{BTC})_{650C-SPS}$ was still unaccounted for, NMR measurements were performed to find the missing products. $\text{Cu}@C - (\text{BTC})_{1000C}$, $\text{Cu}@C - (\text{THQ})_{1000C}$ and $\text{Cu}@C - (\text{HAB})_{550C}$ were also investigated using NMR to verify the HPLC measurements and identify any significant other missed products. As can be seen in Figure 5.21, the formate peaks for $\text{Cu}@C - (\text{BTC})_{1000C}$ and $\text{Cu}@C - (\text{THQ})_{1000C}$ are significantly higher than for $\text{Cu}@C - (\text{BTC})_{650C-SPS}$ and $\text{Cu}@C - (\text{HAB})_{550C}$. This is in agreement with the results obtained using HPLC, as those results showed that the former two materials had higher formate partial current densities than the latter two. This means that the formate peak for $\text{Cu}@C - (\text{HAB})_{550C}$ is expected to be higher than the one for $\text{Cu}@C - (\text{BTC})_{650C-SPS}$, however this was not the case. This can be due to variance in the measurements.

Aside from this Figure 5.21a, a number of additional products were discovered for $\text{Cu}@C - (\text{BTC})_{650C-SPS}$. The additional FE for the products are 15.5 % for 1-propanol, 4.38 % for ethyl acetate, 1.238 % for acetaldehyde, 0.7 % for ethanol, 0.5 % for acetone and 0.1415 % for methanol. Figures 5.21b, 5.21c and 5.21d show that

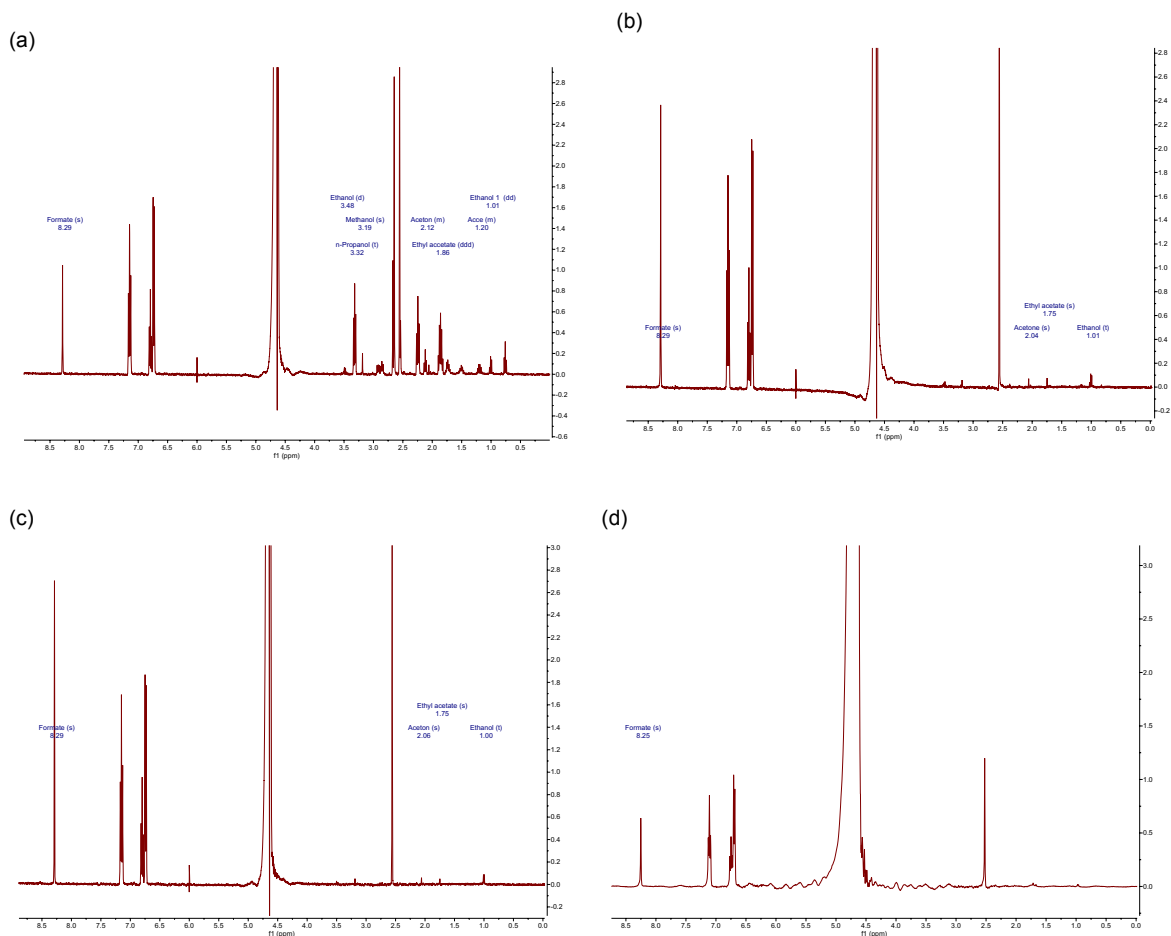


Figure 5.21: NMR measurements signal spectra. (a) $Cu@C - (BTC)_{650C-SPS}$, (b) $Cu@C - (BTC)_{1000C}$, (c) $Cu@C - (THQ)_{1000C}$, (d) $Cu@C - (HAB)_{550C}$. The four unlabeled large peaks are from right to left: DMSO, water, Phenol and something unknown. These are due to the carrier liquid and can thus be ignored.

the other three materials obtained significantly smaller peaks for all of these products. Thus, no significant amount of additional products were produced by these materials. Most of the products produced by $Cu@C - (BTC)_{650C-SPS}$ which were not produced by the other materials are multi-carbon products. Since $Cu@C - (BTC)_{650C-SPS}$ was the only one of these materials without Cu-clusters, this further suggests that the formation of these Cu-clusters changes the selectivity of the material from multi-carbon to single-carbon products.

6

Conclusions

In summary, this thesis investigates the effects of carbonization on the catalytic capabilities for CO_2RR of three different MOFs. First, the effects on the catalytic capabilities of different ways of carbonizing were compared by using different sets of parameters while carbonizing Cu-BTC. These parameters were selected to study the difference between partial and full linker composition as well as the effect of limiting Cu-cluster formations. The catalytic capabilities of the resulting MOF derived materials were then looked into using electrochemical measurements. The CO_2RR products created by the two best-performing Cu-BTC derived materials were further investigated. Besides this, the 2D-MOFs Cu-THQ and Cu-HAB were carbonized and the CO_2RR products of the resulting materials were studied. Characterization techniques were used on all of the MOF derived materials mentioned above in order to understand the changes that carbonization had on their morphology.

This led to the following conclusions. First, that carbonization above the linker decomposition temperature results in higher current densities in CO_2 saturated electrolyte as well as lower charge transfer resistance, indicating that this is more suitable for CO_2RR than carbonization below the linker decomposition temperature.

Furthermore, we were able to produce Cu-BTC derived materials that did not contain Cu-clusters by heating them in a modified SPS machine. These materials showed lower charge transfer resistance, but also lower current densities than the material created in a tubular furnace under full linker decomposition conditions. This shows that carbonizing in this way may both have advantages and disadvantages.

The CO_2RR products formed show that carbonization can influence both selectivity and productivity. The specific carbonization parameters used can further affect these properties. This occurs mainly through the formation of Cu-clusters, the presence of which appears to be a main influencer on selectivity and productivity. Materials derived from different MOFs, yet containing similar Cu-clusters, primarily produce hydrogen and formate at similar production rates. The materials with the largest Cu-clusters, $Cu@C - (BTC)_{1000C}$ and $Cu@C - (THQ)_{1000C}$, reached a FE of up to 33.7 % for formate with a formate partial current density of $-7.9 mA/cm^2$. This formate production

may be linked to the distribution and size of the Cu-clusters in combination with the carbon MOF derivative. The MOF derivative without Cu-clusters also shows affinity for formation of C_2 -products alongside formate production. Cu-HAB derived material contained nitrogen and formed differently shaped Cu-clusters. This did not appear to have an obvious effect on selectivity, but lower current densities were achieved by this catalyst material. These findings show that using different carbonization parameters can change the selectivity of the material, depending on the shape and distribution of the Cu-clusters formed in the process. Thus, it is of importance that the right carbonization settings are selected when trying to create a specific product.

7

Recommendations

Having outlined the conclusions from this work, it is of interest to discuss possibilities that future work may look into.

This study presents a reasoning for formate production on Cu-particles supported on a carbon framework, which is derived through carbonization of Cu-MOFs. Whether this reasoning is correct requires investigation using more experiments and DFT calculations. This could lead to a further understanding of the relations between Cu-clusters size, spacing and catalyst selectivity. Moreover, a comparison could be made between Cu-particles derived via different methods to further understand the way in which differently shaped and spaced Cu-particles impact selectivity and productivity for CO_2RR .

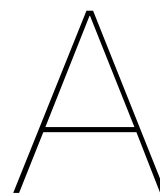
Another aspect that requires further investigation is the stability of the materials. In this study, we were able to show that the catalysts were stable to up to one hour. For practical applications, the material needs to maintain its catalytic capabilities for much longer however. Thus, it is required to do stability tests for larger timescales. This can be done for both the pristine MOFs and the carbonized MOFs to truly understand whether there was an improvement in the stability of the materials.

Something which may in some aspects related to this stability is how the FE for specific products changes during an one-hour measurement. As can be seen in Appendix B Figure B.2-B.5 the FE of methane and ethane production drops significantly after 5 minutes of measurement. This was consistently the case for a multitude of different measurements. As the FEs for methane and ethane were less than one percent during almost all of these measurements, this was not further considered in this thesis. However a single CA+GC measurement was performed using 0.1 M $KHCO_3$ electrolyte with $Cu@C - (BTC)_{650C-SPS}$ as catalyst. As can be seen in Appendix B Figure B.6, this resulted in FEs of 8.4 % ethane and 12.6 % methane during the first 5 minutes after which they dropped to less than 1.0 % each. Future work can investigate why these FEs drop so significantly after five minutes and whether it is possible to maintain them for longer times.

Moreover, further investigation could be led into the effects of combining nitrogen with MOF carbonization. In this study carbonization of Cu-HAB, a MOF that intrinsically contained nitrogen, is investigated. However, it is also possible to nitrogenize MOFs by doping them with nitrogen before pyrolysis [55, 63, 83]. Such techniques can be applied to the MOFs investigated in this study and the resulting materials can be tested as CO_2RR catalysts. Comparing the morphology and performance of these catalysts with the results found in this study could yield further insights into the effects that nitrogen can have on the CO_2RR capabilities of MOF derivatives.

All the CO_2RR product measurements in this study were performed at the same potential of -1.36 V vs SHE, as this made it possible to compare the results. However as shown in Figure 5.17, formate formation was identified to occur already around -0.61 V vs SHE. Therefore, future work could further investigate the effect of applying different potentials. This may lead to better FEs for formate production for $Cu@C - (BTC)_{1000C}$, $Cu@C - (THQ)_{1000C}$ and $Cu@C - (HAB)_{550C}$.

Finally, recently gas diffusion electrodes (GDEs) combined with MOFs or MOF derivatives were used to achieve high current densities compared to other MOF electrodes [131–133]. In order to achieve higher current densities with the materials investigated in this study, it can be of interest to study the effects of combining these materials with a GDE.



Calibration Curves

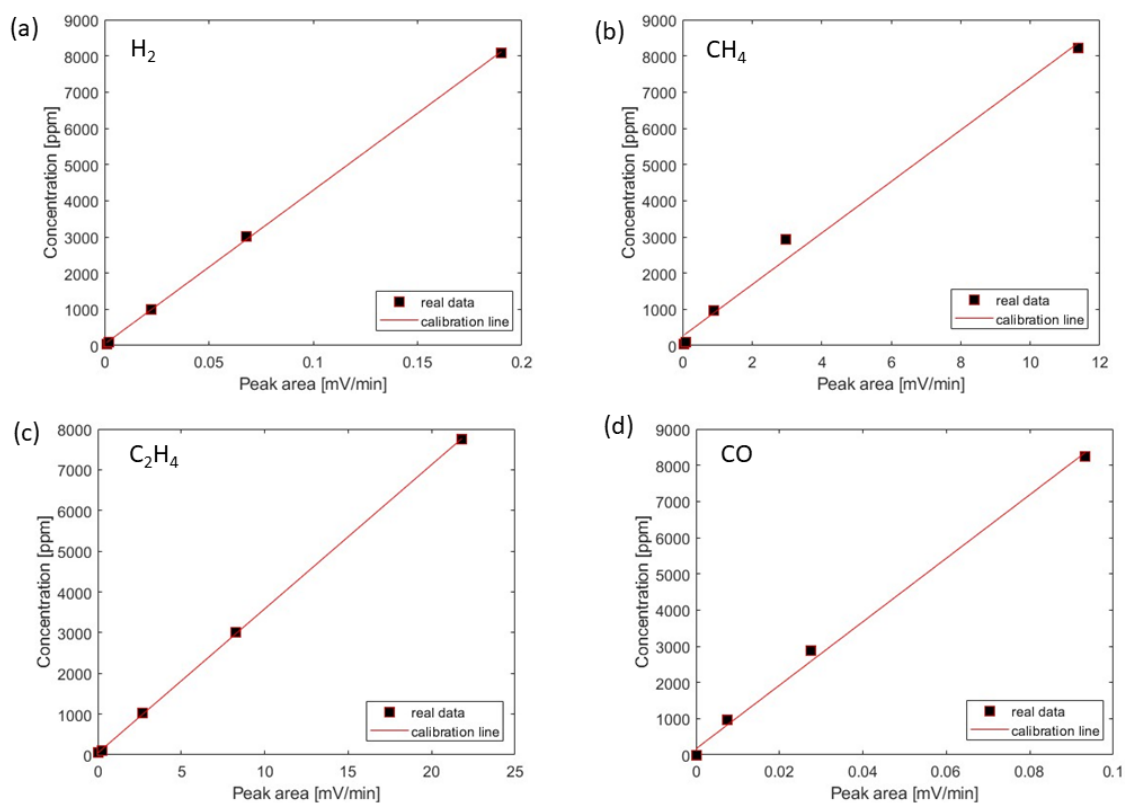


Figure A.1: Calibration plots for GC measurements performed using $Cu@C - (BTC)_{650C-SPS}$, $Cu@C - (BTC)_{1000C}$ and $Cu@C - (THQ)_{1000C}$ catalysts. (a) Hydrogen, (b) Methane, (c) Ethane, (d) CO.

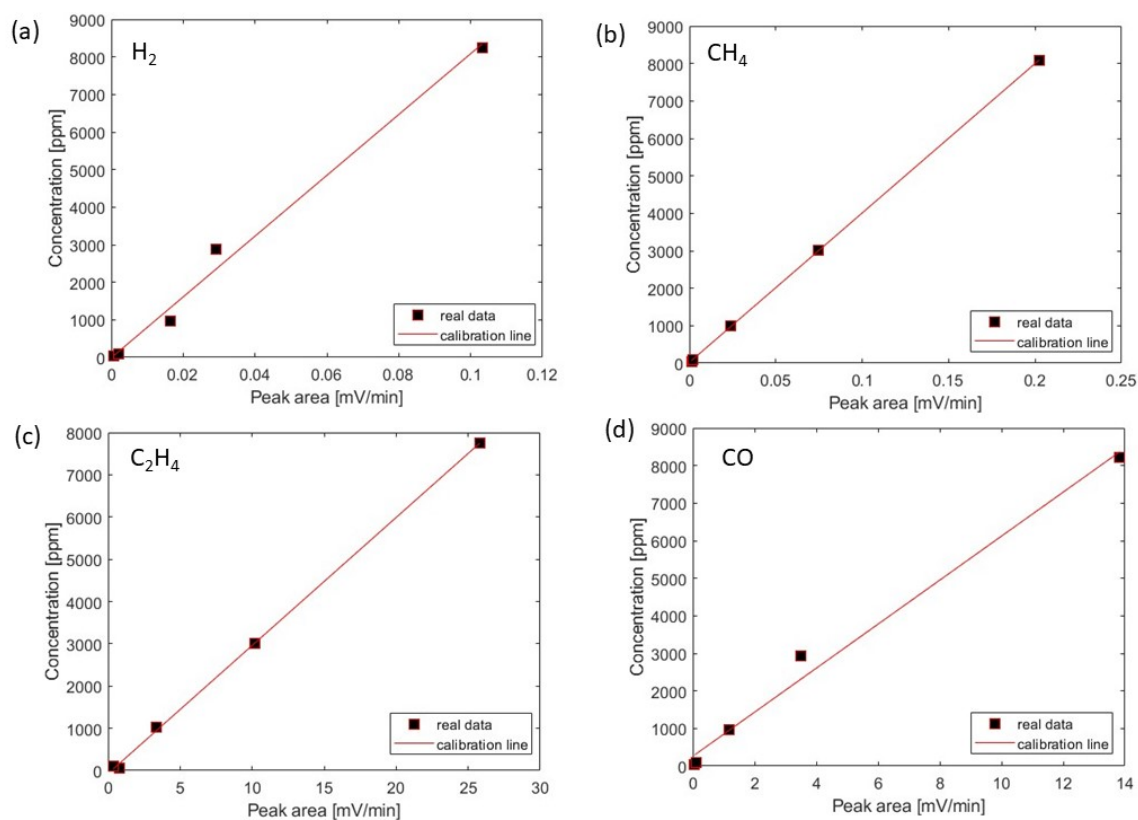


Figure A.2: Calibration plots for GC measurements performed using $Cu@C - (HAB)_{550C}$ catalysts. (a) Hydrogen, (b) Methane, (c) Ethane, (d) CO.

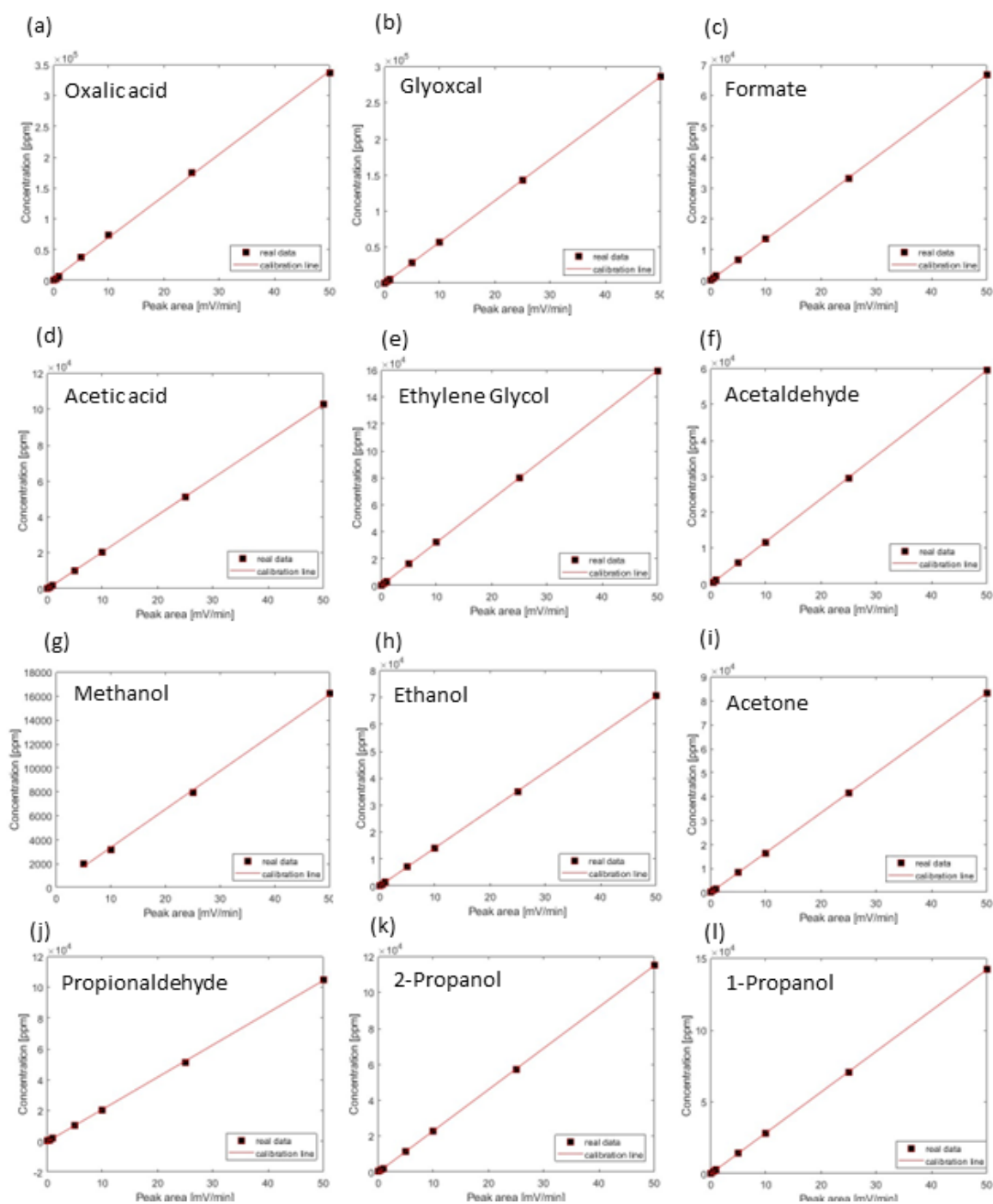


Figure A.3: Calibration plots for HPLC. (a) Oxalic acid, (b) Glyoxal, (c) Formate, (d) Acetic acid, (e) Ethylene Glycol, (f) Acetaldehyde, (g) Methanol, (h) Ethanol, (i) Acetone, (j) Propionaldehyde, (k) 2-Propanol, (l) 1-Propanol.

B

Additional Measurements

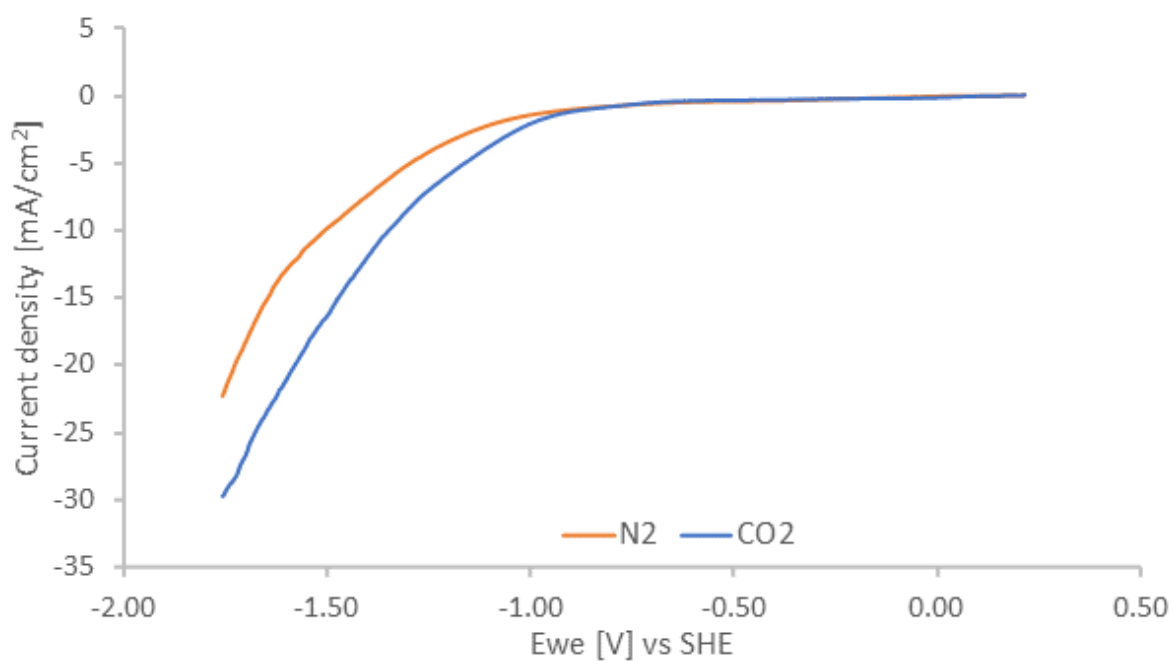


Figure B.1: Different LSV measurement for $Cu@C - (BTC)_{650C-SPS}$, conducted in a one container electrochemical cell containing 1M $KHCO_3$.

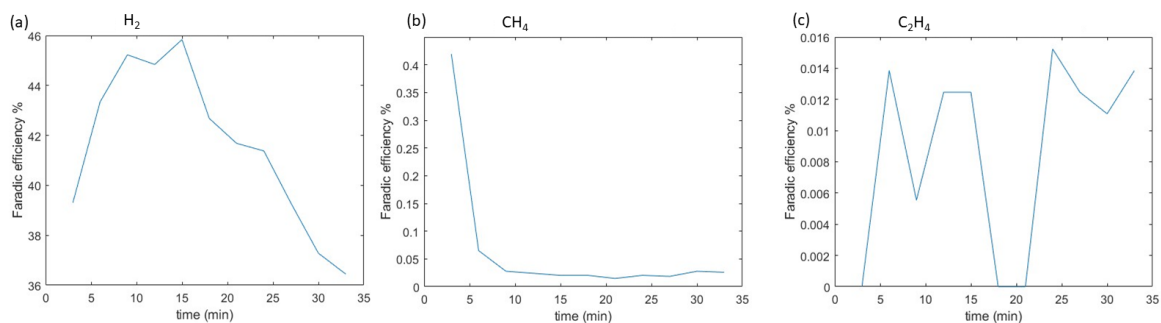


Figure B.2: FE for the $Cu@C - (BTC)_{650C-SPS}$ catalyst during one hour in the flow cell filled with 1M $KHCO_3$ electrolyte with an applied potential of -1.36V vs SHE. (a) H_2 (b) CH_4 (c) C_2H_4 .

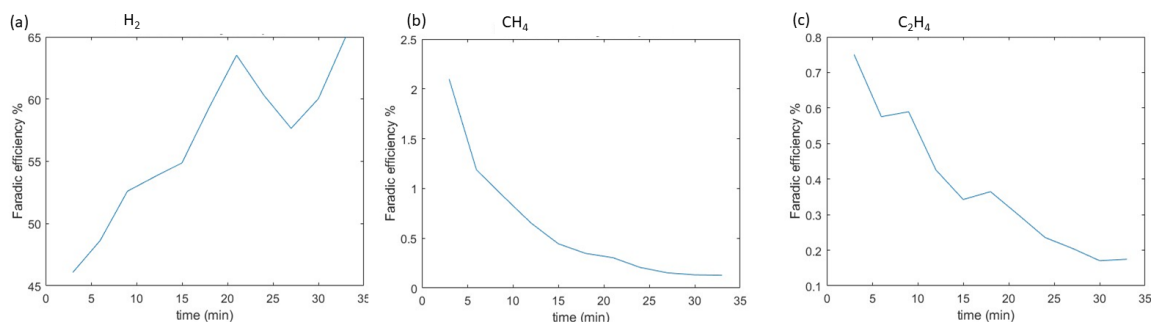


Figure B.3: FE for the $Cu@C - (BTC)_{1000C}$ catalyst during one hour in the flow cell filled with 1M $KHCO_3$ electrolyte with an applied potential of -1.36V vs SHE. (a) H_2 (b) CH_4 (c) C_2H_4 .

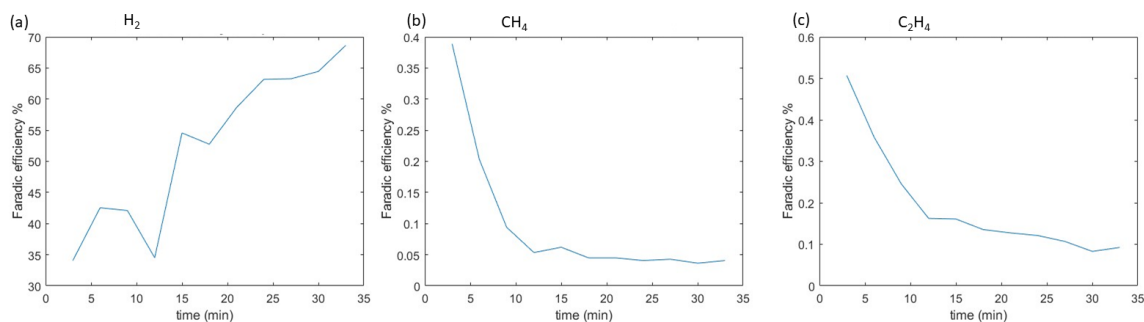


Figure B.4: FE for the $Cu@C - (THQ)_{1000C}$ catalyst during one hour in the flow cell filled with 1M $KHCO_3$ electrolyte with an applied potential of -1.36V vs SHE. (a) H_2 (b) CH_4 (c) C_2H_4 .

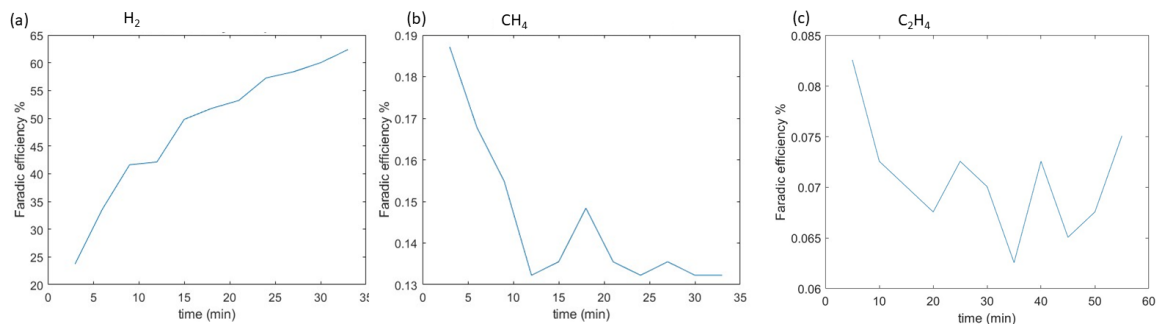


Figure B.5: FE for the $Cu@C - (HAB)_{550C}$ catalyst during one hour in the flow cell filled with 1M $KHCO_3$ electrolyte with an applied potential of -1.36V vs SHE. (a) H_2 (b) CH_4 (c) C_2H_4 .

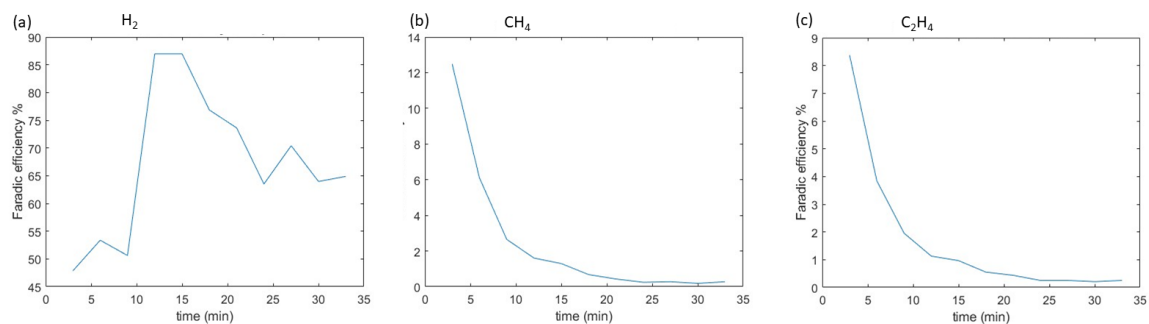


Figure B.6: FE for the $Cu@C - (BTC)_{650C-SPS}$ catalyst during one hour in the flow cell filled with 0.1M $KHCO_3$ electrolyte with an applied potential of -1.36V vs SHE. (a) H_2 (b) CH_4 (c) C_2H_4 .

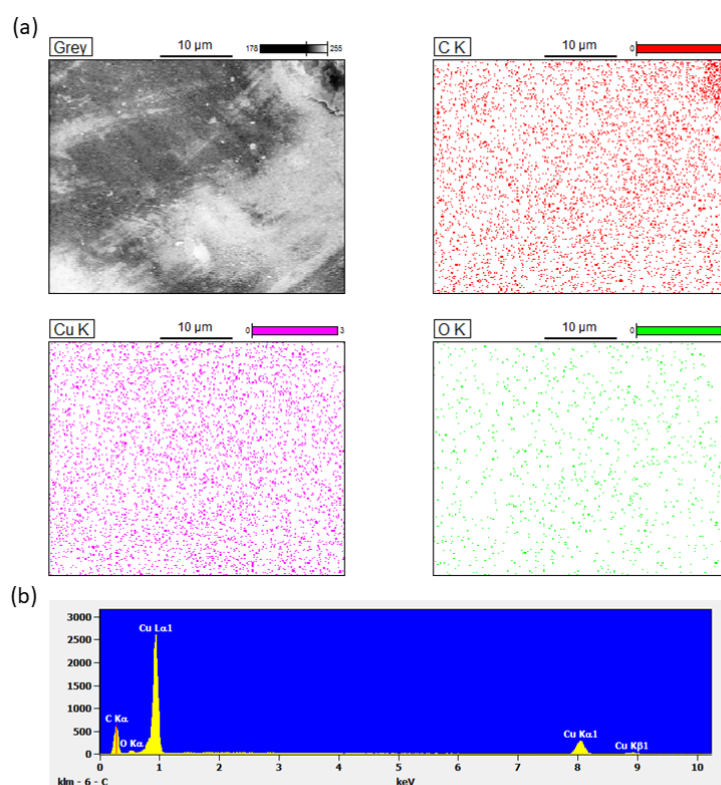
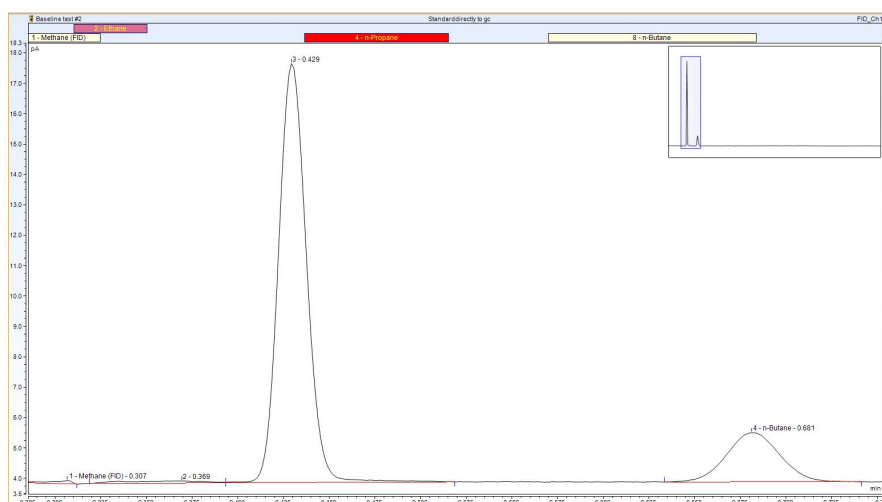


Figure B.7: EDS analysis of a material created by placing Cu-BTC in an SPS machine and heating it up to 500°C under 4 MPa pressure. (a) element map (b) spectrum. Corresponding atom% of these measurements can be found in Table B.1.

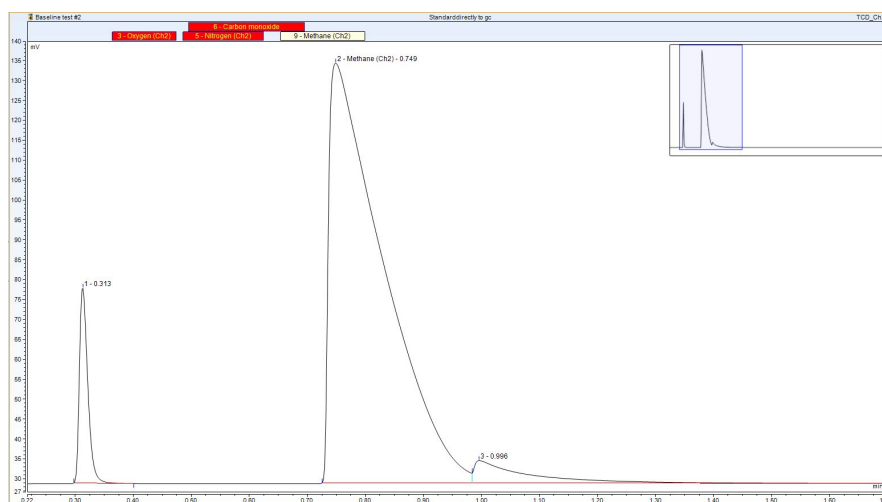
Table B.1: elemental composition as found by the EDS analysis which can be seen in Figure B.7.

element	atom%
C	60.97
O	3.15
Cu	35.87

(a)



(b)



(c)

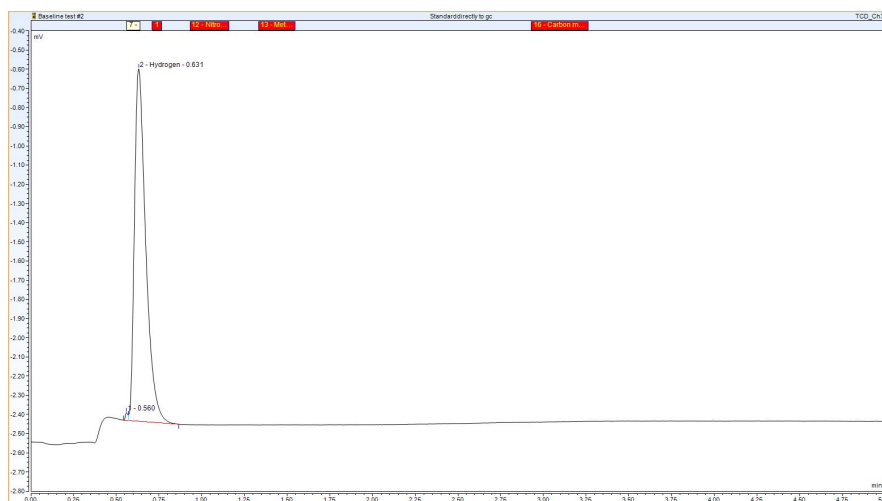
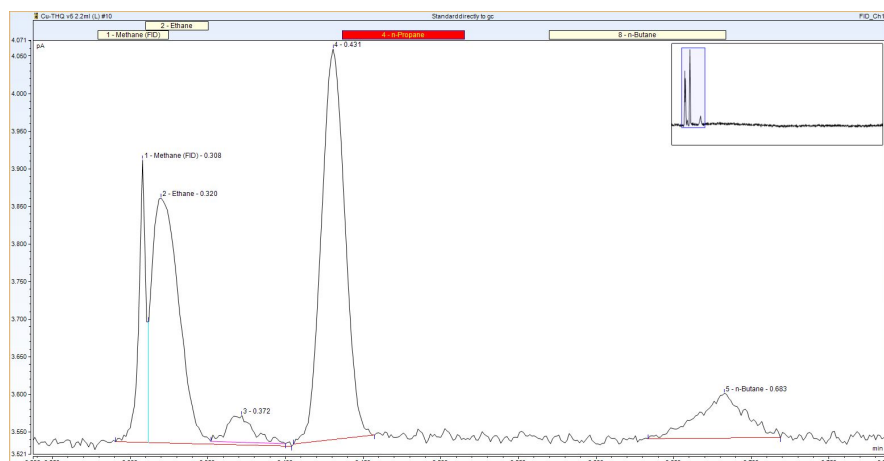
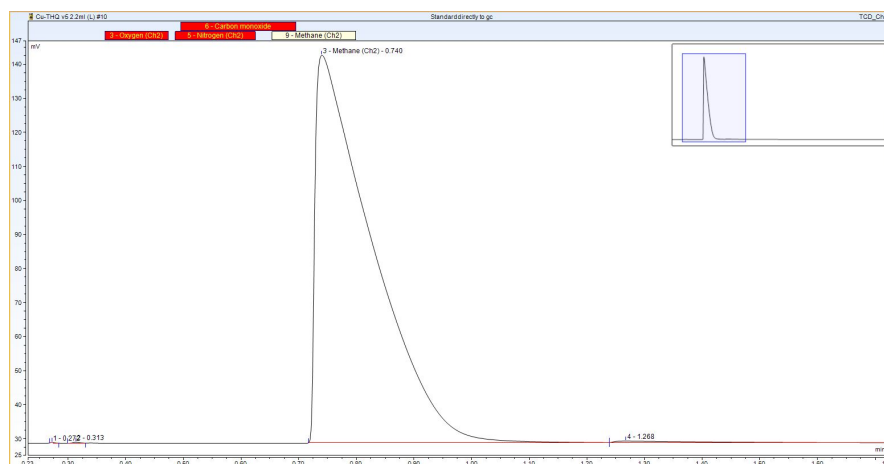


Figure B.8: GC spectra of a baseline test run using a catalyst made by drop casting 95 wt% PTFE and 5 wt% carbon black soluted in 2.5 mL water and 2.5 mL isopropanol on a glassy carbon substrate. The measurement was performed in the flow cell with an applied potential of -1.36 V vs SHE under a constant CO_2 gas flow of 10 mL/min. (a) GC column 1 (b) GC column 2 (c) GC column 3.

(a)



(b)



(c)

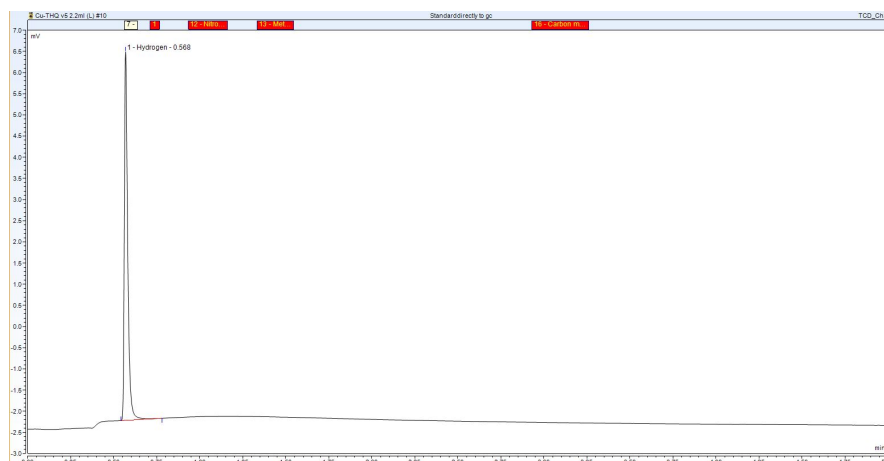


Figure B.9: GC spectra of a $Cu@C - (THQ)_{1000C}$ test run using a catalyst made by drop casting 20 wt% PTFE, 5 wt% carbon black and 75 wt% $Cu@C - (THQ)_{1000C}$ soluted in 2.5 mL water and 2.5 mL isopropanol on a glassy carbon substrate. The measurement was performed in the flow cell with an applied potential of -1.36 V vs SHE under a constant CO_2 gas flow of 10 mL/min. (a) GC column 1 (b) GC column 2 (c) GC column 3.

Bibliography

- [1] C. Beer, Markus Reichstein, Enrico Tomelleri, Philippe Ciais, Martin Jung, Nuno Carvalhais, Christian Rödenbeck, M. Altaf Arain, Dennis Baldocchi, Gordon B. Bonan, Alberte Bondeau, Alessandro Cescatti, Gitta Lasslop, Anders Lindroth, Mark Lomas, Sebastiaan Luysaert, Hank Margolis, Keith W. Oleson, Olivier Rouspard, Elmar Veenendaal, Nicolas Viovy, Christopher Williams, F. Ian Woodward, and Dario Papale. “Terrestrial Gross Carbon Dioxide Uptake: Global Distribution and Covariation with Climate”. In: *Science* 329.5993 (2010), pp. 834–838.
- [2] H. Wang, B.W. Ang, and Bin Su. “A Multi-region Structural Decomposition Analysis of Global CO2 Emission Intensity”. In: *Ecological Economics* 142 (2017), pp. 163–176.
- [3] R. Lindsey and E. Dlugokencky. *Climate Change: Atmospheric Carbon Dioxide*. 2022. URL: <https://www.climate.gov/news-features/understanding-climate/climate-change-atmospheric-carbon-dioxide> (visited on 11/17/2022).
- [4] A. Stips, D. Macias, C. Coughlan, E. Garcia-Gorri, and X.S. Liang. “On the causal structure between CO2 and global temperature”. In: *Scientific Reports* 6 (1 2016).
- [5] United Nations. *Causes and Effects of Climate Change*. URL: <https://www.un.org/en/climatechange/science/causes-effects-climate-change> (visited on 11/17/2022).
- [6] N. Choucri and V. Ferraro. *International politics of energy interdependence: the case of petroleum*. Massachusetts Institute of Technology, 1976.
- [7] M. Kivinen and B. Humphreys. *Russian Modernization: A new Paradigm*. Routledge, 2020, pp. 25–26.
- [8] C. Ang’u, N. Muthama, C. Oludhe, and L. S. Kong’ani. “Effects of Civil Conflicts on Global Oil Prices and their Impact on the Energy Sector”. In: *Journal of Sustainability, Environment and Peace* 1 (Apr. 2019).
- [9] A. J. Garzon Gordon and L. A. Hierro Recio. “External Effects of the War in Ukraine: The Impact on the Price of Oil in the Short-term”. In: 9 (Feb. 2019), pp. 267–276.
- [10] G. Kharlamova, S. Nate, and O. Chernyak. “Renewable energy and security for Ukraine: Challenge or smart way?” In: *Journal of International Studies* 9 (Mar. 2016), pp. 88–115.
- [11] IEA. *Global Energy Review 2021*. 2021. URL: <https://www.iea.org/reports/global-energy-review-2021> (visited on 08/10/2022).

- [12] William A Braff, Joshua M Mueller, and Jessika E Trancik. "Value of storage technologies for wind and solar energy". In: *Nature Climate Change* 6.10 (2016), pp. 964–969.
- [13] Abdulla Rahil, Rupert Gammon, Neil Brown, Justin Udie, and Muhammad Usman Mazhar. "Potential economic benefits of carbon dioxide (CO₂) reduction due to renewable energy and electrolytic hydrogen fuel deployment under current and long term forecasting of the Social Carbon Cost (SCC)". In: *Energy Reports* 5 (2019), pp. 602–618.
- [14] Qiwen Lai, Yahui Sun, Ting Wang, Poojan Modi, Claudio Cazorla, Umit B. Demirci, Jose Ramon Ares Fernandez, Fabrice Leardini, and Kondo-François Aguey-Zinsou. "How to Design Hydrogen Storage Materials? Fundamentals, Synthesis, and Storage Tanks". In: *Advanced Sustainable Systems* 3.9 (2019), p. 1900043.
- [15] Andreas Züttel. "Hydrogen storage methods". In: *Die Naturwissenschaften* 91 (Apr. 2004), pp. 157–72.
- [16] Puru Jena. "Materials for Hydrogen Storage: Past, Present, and Future". In: *The Journal of Physical Chemistry Letters* 2.3 (2011), pp. 206–211.
- [17] Oleksandr S. Bushuyev, Phil De Luna, Cao Thang Dinh, Ling Tao, Genevieve Saur, Jao van de Lagemaat, Shana O. Kelley, and Edward H. Sargent. "What Should We Make with CO₂ and How Can We Make It?" In: *Joule* 2.5 (2018), pp. 825–832.
- [18] Gabriele Centi, Elsje Alessandra Quadrelli, and Siglinda Perathoner. "Catalysis for CO₂ conversion: a key technology for rapid introduction of renewable energy in the value chain of chemical industries". In: *Energy Environ. Sci.* 6 (6 2013), pp. 1711–1731.
- [19] Xiaolong Zhang, Si-Xuan Guo, Karl Gandionco, Alan Bond, and Jie Zhang. "Electrocatalytic carbon dioxide reduction: from fundamental principles to catalyst design". In: *Materials Today Advances* 7 (Sept. 2020), p. 100074.
- [20] Hitoshi Ishida. "Electrochemical/Photochemical CO₂ Reduction Catalyzed by Transition Metal Complexes". In: *Carbon Dioxide Chemistry, Capture and Oil Recovery*. Ed. by Iyad Karamé, Janah Shaya, and Hassan Srour. Rijeka: In-techOpen, 2018. Chap. 2.
- [21] Wan-Hui Wang, Yuichiro Himeda, James T. Muckerman, Gerald F. Manbeck, and Etsuko Fujita. "CO₂ Hydrogenation to Formate and Methanol as an Alternative to Photo- and Electrochemical CO₂ Reduction". In: *Chemical Reviews* 115.23 (2015), pp. 12936–12973.
- [22] Yuhou Pei, Heng Zhong, and Fangming Jin. "A brief review of electrocatalytic reduction of CO₂—Materials, reaction conditions, and devices". In: *Energy Science & Engineering* 9.7 (2021), pp. 1012–1032.
- [23] Kun Zhao, Yanming Liu, Xie Quan, Shuo Chen, and Hongtao Yu. "CO₂ Electroreduction at Low Overpotential on Oxide-Derived Cu/Carbons Fabricated from Metal Organic Framework". In: *ACS Applied Materials & Interfaces* 9.6 (2017), pp. 5302–5311.

- [24] Xiaowa Nie, Monica R. Esopi, Michael J. Janik, and Aravind Asthagiri. "Selectivity of CO₂ Reduction on Copper Electrodes: The Role of the Kinetics of Elementary Steps". In: *Angewandte Chemie International Edition* 52.9 (2013), pp. 2459–2462.
- [25] Qi Lu and Feng Jiao. "Electrochemical CO₂ reduction: Electrocatalyst, reaction mechanism, and process engineering". In: *Nano Energy* 29 (2016). Electrocatalysis, pp. 439–456.
- [26] Ermete Antolini. "Carbon supports for low-temperature fuel cell catalysts". In: *Applied Catalysis B: Environmental* 88.1 (2009), pp. 1–24.
- [27] Md Golam Kibria, Jonathan P. Edwards, Christine M. Gabardo, Cao-Thang Dinh, Ali Seifitokaldani, David Sinton, and Edward H. Sargent. "Electrochemical CO₂ Reduction into Chemical Feedstocks: From Mechanistic Electrocatalysis Models to System Design". In: *Advanced Materials* 31.31 (2019), p. 1807166.
- [28] Da-Ming Feng, Yun-Pei Zhu, Ping Chen, and Tian-Yi Ma. "Recent Advances in Transition-Metal-Mediated Electrocatalytic CO₂ Reduction: From Homogeneous to Heterogeneous Systems". In: *Catalysts* 7.12 (2017).
- [29] Shengnan Sun, Haiyan Li, and Zhichuan J. Xu. "Impact of Surface Area in Evaluation of Catalyst Activity". In: *Joule* 2.6 (2018), pp. 1024–1027.
- [30] Roger Lin, Jiaxun Guo, Xiaojia Li, Poojan Patel, and Ali Seifitokaldani. "Electrochemical Reactors for CO₂ Conversion". In: *Catalysts* 10.5 (2020).
- [31] Hefei Li, Tianfu Liu, Pengfei Wei, Long Lin, Dunfeng Gao, Guoxiong Wang, and Xinhe Bao. "High-Rate CO₂ Electroreduction to C₂+ Products over a Copper-Copper Iodide Catalyst". In: *Angewandte Chemie International Edition* 60 (Apr. 2021), pp. 14329–14333.
- [32] Dunfeng Gao, Yi Zhang, Zhiwen Zhou, Fan Cai, Xinfei Zhao, Wugen Huang, Yangsheng Li, Junfa Zhu, Ping Liu, Fan Yang, Guoxiong Wang, and Xinhe Bao. "Enhancing CO₂ Electroreduction with the Metal–Oxide Interface". In: *Journal of the American Chemical Society* 139.16 (2017), pp. 5652–5655.
- [33] Xinyue Ma, Jianjun Du, Hao Sun, Fenghui Ye, Xin Wang, Pengfei Xu, Chuangang Hu, Lipeng Zhang, and Dong Liu. "Boron, nitrogen co-doped carbon with abundant mesopores for efficient CO₂ electroreduction". In: *Applied Catalysis B: Environmental* 298 (2021), p. 120543.
- [34] Xi-Qing Wang, Qin Chen, Ya-Jiao Zhou, Hong-Mei Li, Jun-Wei Fu, and Min Liu. "Cu-based bimetallic catalysts for CO₂ reduction reaction". In: *Advanced Sensor and Energy Materials* 1.3 (2022), p. 100023.
- [35] Song Liu, Hongbin Yang, Xiong Su, Jie Ding, Qing Mao, Yanqiang Huang, Tao Zhang, and Bin Liu. "Rational design of carbon-based metal-free catalysts for electrochemical carbon dioxide reduction: A review". In: *Journal of Energy Chemistry* 36 (2019), pp. 95–105.
- [36] Recep Kas, Ruud Kortlever, Alexander Milbrat, Marc T. M. Koper, Guido Mul, and Jonas Baltrusaitis. "Electrochemical CO₂ reduction on Cu₂O-derived copper nanoparticles: controlling the catalytic selectivity of hydrocarbons". In: *Phys. Chem. Chem. Phys.* 16 (24 2014), pp. 12194–12201.

- [37] Chansol Kim, Kyeong Min Cho, Kangho Park, Ju Ye Kim, Geun-Tae Yun, Francesca M. Toma, Issam Gereige, and Hee-Tae Jung. "Cu/Cu₂O Interconnected Porous Aerogel Catalyst for Highly Productive Electrosynthesis of Ethanol from CO₂". In: *Advanced Functional Materials* 31.32 (2021), p. 2102142.
- [38] Liping Zhao, Bingquan Wang, and Rui Wang. "A Critical Review on New and Efficient 2D Materials for Catalysis". In: *Advanced Materials Interfaces* 9.29 (2022), p. 2200771.
- [39] Zhenyu Sun, Tao Ma, Hengcong Tao, Qun Fan, and Buxing Han. "Fundamentals and Challenges of Electrochemical CO₂ Reduction Using Two-Dimensional Materials". In: *Chem* 3.4 (2017), pp. 560–587.
- [40] Lei Dai, Qing Qin, Pei Wang, Xiaojing Zhao, Chengyi Hu, Pengxin Liu, Ruixuan Qin, Mei Chen, Daohui Ou, Chaofa Xu, Shiguang Mo, Binghui Wu, Gang Fu, Peng Zhang, and Nanfeng Zheng. "Ultrastable atomic copper nanosheets for selective electrochemical reduction of carbon dioxide". In: *Science Advances* 3.9 (2017), e1701069.
- [41] Xiaorong Zhu and Yafei Li. "Review of two-dimensional materials for electrochemical CO₂ reduction from a theoretical perspective". In: *WIREs Computational Molecular Science* 9.6 (2019), e1416.
- [42] Jingjie Wu, Mingjie Liu, Pranav P. Sharma, Ram Manohar Yadav, Lulu Ma, Yingchao Yang, Xiaolong Zou, Xiao-Dong Zhou, Robert Vajtai, Boris I. Yakobson, Jun Lou, and Pulickel M. Ajayan. "Incorporation of Nitrogen Defects for Efficient Reduction of CO₂ via Two-Electron Pathway on Three-Dimensional Graphene Foam". In: *Nano Letters* 16.1 (2016), pp. 466–470.
- [43] Hui Zhang, Ying Ma, Fengjiao Quan, Jiajin Huang, Falong Jia, and Lizhi Zhang. "Selective electro-reduction of CO₂ to formate on nanostructured Bi from reduction of BiOCl nanosheets". In: *Electrochemistry Communications* 46 (2014), pp. 63–66.
- [44] Sisi He, Fenglou Ni, Yujin Ji, Lie Wang, Yunzhou Wen, Haipeng Bai, Gejun Liu, Ye Zhang, Youyong Li, Bo Zhang, and Huisheng Peng. "The p-Orbital Delocalization of Main-Group Metals to Boost CO₂ Electroreduction". In: *Angewandte Chemie International Edition* 57.49 (2018), pp. 16114–16119.
- [45] Ebrahim Tayyebi, Javed Hussain, Younes Abghoui, and Egill Skúlason. "Trends of Electrochemical CO₂ Reduction Reaction on Transition Metal Oxide Catalysts". In: *The Journal of Physical Chemistry C* 122.18 (2018), pp. 10078–10087.
- [46] Shan Gao, Zhongti Sun, Wei Liu, Xingchen Jiao, Xiaolong Zu, Qitao Hu, Yongfu Sun, Tao Yao, Wenhua Zhang, Shiqiang Wei, and Yi Xie. "Atomic layer confined vacancies for atomic-level insights into carbon dioxide electroreduction". In: *Nature Communications* 8 (Feb. 2017), p. 14503.
- [47] Shan Gao, Xingchen Jiao, Zhongti Sun, Wenhua Zhang, Yongfu Sun, Chengming Wang, Qitao Hu, Xiaolong Zu, Fan Yang, Shuyang Yang, Liang Liang, Ju Wu, and Yi Xie. "Ultrathin Co₃O₄ Layers Realizing Optimized CO₂ Electroreduction to Formate". In: *Angewandte Chemie International Edition* 55.2 (2016), pp. 698–702.

- [48] Mohammad Asadi, Bijandra Kumar, Amirhossein Behranginia, Brian Rosen, Artem Baskin, Nikita Reprnin, Davide Pisasale, Patrick Phillips, Wei Zhu, Richard Haasch, R. Klie, Petr Král, Jeremiah Abiade, and Amin Salehi-Khojin. "Robust carbon dioxide reduction on molybdenum disulphide edges". In: *Nature communications* 5 (July 2014), p. 4470.
- [49] Guodong Shi, Luo Yu, Xin Ba, Xiaoshu Zhang, Jianqing Zhou, and Ying Yu. "Copper nanoparticle interspersed MoS₂ nanoflowers with enhanced efficiency for CO₂ electrochemical reduction to fuel". In: *Dalton Trans.* 46 (32 2017), pp. 10569–10577.
- [50] Albertus D. Handoko, Hetian Chen, Yanwei Lum, Qianfan Zhang, Babak Anasori, and Zhi Wei Seh. "Two-Dimensional Titanium and Molybdenum Carbide MXenes as Electrocatalysts for CO₂ Reduction". In: *iScience* 23.6 (2020), p. 101181.
- [51] Neng Li, Xingzhu Chen, Wee-Jun Ong, Douglas R. MacFarlane, Xiujian Zhao, Anthony K. Cheetham, and Chenghua Sun. "Understanding of Electrochemical Mechanisms for CO₂ Capture and Conversion into Hydrocarbon Fuels in Transition-Metal Carbides (MXenes)". In: *ACS Nano* 11.11 (2017), pp. 10825–10833.
- [52] Nuwan H. Attanayake, Huta R. Banjade, Akila C. Thenuwara, Babak Anasori, Qimin Yan, and Daniel R. Strongin. "Electrocatalytic CO₂ reduction on earth abundant 2D Mo₂C and Ti₃C₂ MXenes". In: *Chem. Commun.* 57 (13 2021), pp. 1675–1678.
- [53] Tayebeh Khosravi and Mohammadreza Omidkhah. "Preparation of CO₂ selective composite membranes using Pebax/CuBTC/PEG-ran-PPG ternary system". In: *Journal of Energy Chemistry* 26 (Dec. 2016).
- [54] Stuart L. James. "Metal-organic frameworks". In: *Chem. Soc. Rev.* 32 (5 2003), pp. 276–288.
- [55] Anxiang Guan, Zheng Chen, Yueli Quan, Chen Peng, Zhiqiang Wang, Tsun-Kong Sham, Chao Yang, Yali Ji, Linping Qian, Xin Xu, and Gengfeng Zheng. "Boosting CO₂ Electroreduction to CH₄ via Tuning Neighboring Single-Copper Sites". In: *ACS Energy Letters* 5.4 (2020), pp. 1044–1053.
- [56] Charles W. Machan, Steven A. Chabolla, Jian Yin, Michael K. Gilson, F. Akif Tezcan, and Clifford P. Kubiak. "Supramolecular Assembly Promotes the Electrocatalytic Reduction of Carbon Dioxide by Re(I) Bipyridine Catalysts at a Lower Overpotential". In: *Journal of the American Chemical Society* 136.41 (2014), pp. 14598–14607.
- [57] Xiaofang Li and Qi-Long Zhu. "MOF-based materials for photo- and electrocatalytic CO₂ reduction". In: *EnergyChem* 2.3 (2020), p. 100033.
- [58] Idan Hod, Matthew D. Sampson, Pravas Deria, Clifford P. Kubiak, Omar K. Farha, and Joseph T. Hupp. "Fe-Porphyrin-Based Metal–Organic Framework Films as High-Surface Concentration, Heterogeneous Catalysts for Electrochemical Reduction of CO₂". In: *ACS Catalysis* 5.11 (2015), pp. 6302–6309.

- [59] Reiko Hinogami, Satoshi Yotsuhashi, Masahiro Deguchi, Yuji Zenitani, Hiroshi Hashiba, and Yuka Yamada. "Electrochemical Reduction of Carbon Dioxide Using a Copper Rubenate Metal Organic Framework". In: *ECS Electrochemistry Letters* 1.4 (Aug. 2012), H17.
- [60] R. Kumar, S. Kumar, and Anbu Kulandainathan. "Highly selective electrochemical reduction of carbon dioxide using Cu based metal organic framework as an electrocatalyst". In: *Electrochemistry Communications* 25 (Nov. 2012), pp. 70–73.
- [61] Jonathan Albo, Daniel Vallejo, Garikoitz Beobide, Oscar Castillo, Pedro Castaño, and Angel Irabien. "Copper-Based Metal–Organic Porous Materials for CO₂ Electrocatalytic Reduction to Alcohols". In: *ChemSusChem* 10.6 (2017), pp. 1100–1109.
- [62] Dae-Hyun Nam, Oleksandr S. Bushuyev, Jun Li, Phil De Luna, Ali Seifitokaldani, Cao-Thang Dinh, F. Pelayo García de Arquer, Yuhang Wang, Zhiqin Liang, Andrew H. Proppe, Chih Shan Tan, Petar Todorović, Osama Shekhah, Christine M. Gabardo, Jea Woong Jo, Jongmin Choi, Min-Jae Choi, Se-Woong Baek, Junghwan Kim, David Sinton, Shana O. Kelley, Mohamed Eddaoudi, and Edward H. Sargent. "Metal–Organic Frameworks Mediate Cu Coordination for Selective CO₂ Electroreduction". In: *Journal of the American Chemical Society* 140.36 (2018), pp. 11378–11386.
- [63] Da Li, Tongtong Liu, Zhengyu Yan, Liang Zhen, Jia Liu, Jing Wu, and Yujie Feng. "MOF-Derived Cu₂O/Cu Nanospheres Anchored in Nitrogen-Doped Hollow Porous Carbon Framework for Increasing the Selectivity and Activity of Electrochemical CO₂-to-Formate Conversion". In: *ACS Applied Materials & Interfaces* 12.6 (2020), pp. 7030–7037.
- [64] Eric M. Johnson, Stefan Ilic, and Amanda J. Morris. "Design Strategies for Enhanced Conductivity in Metal–Organic Frameworks". In: *ACS Central Science* 7.3 (2021), pp. 445–453.
- [65] Dawei Feng, Ting Lei, Maria Lukatskaya, Jihye Park, Zhehao Huang, Minah Lee, Leo Shaw, Shucheng Chen, Andrey Yakovenko, Ambarish Kulkarni, Jianping Xiao, Kurt Fredrickson, Jeffrey Tok, Xiaodong Zou, Yi Cui, and Zhenan Bao. "Robust and conductive two-dimensional metal–organic frameworks with exceptionally high volumetric and areal capacitance". In: *Nature Energy* 3 (Jan. 2018).
- [66] Cunrong Zhang, Qi Zhang, Kai Zhang, Zhenyu Xiao, Yu Yang, and Lei Wang. "Facile synthesis of a two-dimensional layered Ni-MOF electrode material for high performance supercapacitors". In: *RSC Advances* 8 (May 2018), pp. 17747–17753.
- [67] Leily Majidi, Alireza Ahmadiparidari, Nannan Shan, Saurabh N. Misal, Khagesh Kumar, Zhehao Huang, Sina Rastegar, Zahra Hemmat, Xiaodong Zou, Peter Zapol, Jordi Cabana, Larry A. Curtiss, and Amin Salehi-Khojin. "2D Copper Tetrahydroxyquinone Conductive Metal–Organic Framework for Selective CO₂ Electrocatalysis at Low Overpotentials". In: *Advanced Materials* 33.10 (2021), p. 2004393.

- [68] Fan Yang, Aling Chen, Pei Lin Deng, Yinzhen Zhou, Zaman Shahid, Hongfang Liu, and Bao Yu Xia. "Highly efficient electroconversion of carbon dioxide into hydrocarbons by cathodized copper–organic frameworks". In: *Chem. Sci.* 10 (34 2019), pp. 7975–7981.
- [69] Jingjuan Liu, Dan Yang, Yi Zhou, Guang Zhang, Guolong Xing, Yunpeng Liu, Yanhang Ma, Osamu Terasaki, Shubin Yang, and Long Chen. "Tricycloquinazoline-Based 2D Conductive Metal–Organic Frameworks as Promising Electrocatalysts for CO₂ Reduction". In: *Angewandte Chemie International Edition* 60.26 (2021), pp. 14473–14479.
- [70] Tingting Zhan, Yingbing Zou, Ying Yang, Xiuling Ma, Zhangjing Zhang, and Shengchang Xiang. "Two-dimensional Metal-organic Frameworks for Electrochemical CO₂ Reduction Reaction". In: *ChemCatChem* 14.3 (2022), e202101453.
- [71] Ming-Hua Zeng, Qiang-Xin Wang, Yan-Xi Tan, Sheng Hu, Hai-Xia Zhao, La-Sheng Long, and Mohamedally Kurmoo. "Rigid Pillars and Double Walls in a Porous Metal-Organic Framework: Single-Crystal to Single-Crystal, Controlled Uptake and Release of Iodine and Electrical Conductivity". In: *Journal of the American Chemical Society* 132.8 (2010), pp. 2561–2563.
- [72] Yoji Kobayashi, Benjamin Jacobs, Mark D. Allendorf, and Jeffrey R. Long. "Conductivity, Doping, and Redox Chemistry of a Microporous Dithiolene-Based Metal–Organic Framework". In: *Chemistry of Materials* 22.14 (2010), pp. 4120–4122.
- [73] F. James Claire, Marina A Solomos, Jungkil Kim, Gaoqiang Wang, Maxime A. Siegler, Michael F. Crommie, and Thomas J. Kempa. "Structural and electronic switching of a single crystal 2D metal-organic framework prepared by chemical vapor deposition". In: *Nature Communications* 11 (1 2020).
- [74] Subhadip Goswami, Idan Hod, Jiabin Dawn Duan, Chung-Wei Kung, Martino Rimoldi, Christos D Malliakas, Rebecca H. Palmer, Omar K. Farha, and Joseph T. Hupp. "Anisotropic Redox Conductivity within a Metal–Organic Framework Material". In: *Journal of the American Chemical Society* 141.44 (2019), pp. 17696–17702.
- [75] Ru-Min Wang, Shui-Rong Zheng, and Yaping Zheng. "Reinforced materials". In: Dec. 2011, pp. 56–60.
- [76] Biswa Nath Bhadra, Ajayan Vinu, Christian Serre, and Sung Hwa Jhung. "MOF-derived carbonaceous materials enriched with nitrogen: Preparation and applications in adsorption and catalysis". In: *Materials Today* 25 (2019), pp. 88–111.
- [77] "Carbon-based electrocatalysts for CO₂ electroreduction produced via MOF, biomass, and other precursors carbonization: A review". In: *Journal of CO₂ Utilization* 42 (2020), p. 101350.
- [78] Junyu Liu, Luwei Peng, Yue Zhou, Li Lv, Jing Fu, Jia Lin, Daniel Guay, and Jinli Qiao. "Metal–Organic-Frameworks-Derived Cu/Cu₂O Catalyst with Ultrahigh Current Density for Continuous-Flow CO₂ Electroreduction". In: *ACS Sustainable Chemistry and Engineering* 7.18 (2019), pp. 15739–15746.

- [79] Changting Wei, Xia Li, Fugang Xu, Hongliang Tan, Zhuang Li, Lanlan Sun, and Yonghai Song. "Metal organic framework-derived anthill-like Cu@carbon nanocomposites for nonenzymatic glucose sensor". In: *Anal. Methods* 6 (5 2014), pp. 1550–1557.
- [80] Qing Tao Wang, Rong Yang, Jian Li, Yaoxia Yang, Yanxia Wu, Xiaozhong Zhou, Guofu Ma, and Ren Shufang. "2D DUT-8(Ni)-derived Ni@C nanosheets for efficient hydrogen evolution". In: *Journal of Solid State Electrochemistry* 24 (Oct. 2020), pp. 1–7.
- [81] Lin He, Florian Weniger, Helfried Neumann, and Matthias Beller. "Synthesis, Characterization, and Application of Metal Nanoparticles Supported on Nitrogen-Doped Carbon: Catalysis beyond Electrochemistry". In: *Angewandte Chemie International Edition* 55.41 (2016), pp. 12582–12594.
- [82] Ana Sofia Varela, Nastaran Ranjbar Sahraie, Julian Steinberg, Wen Ju, Hyung-Suk Oh, and Peter Strasser. "Metal-Doped Nitrogenated Carbon as an Efficient Catalyst for Direct CO₂ Electroreduction to CO and Hydrocarbons". In: *Angewandte Chemie International Edition* 54.37 (2015), pp. 10758–10762.
- [83] Yuan-Sheng Cheng, Xin-Ping Chu, Min Ling, Na Li, Kong-Lin Wu, Fang-Hui Wu, Hong Li, Guozan Yuan, and Xian-Wen Wei. "An MOF-derived copper@nitrogen-doped carbon composite: the synergistic effects of N-types and copper on selective CO₂ electroreduction". In: *Catal. Sci. Technol.* 9 (20 2019), pp. 5668–5675.
- [84] Graham Smith and Edmund J. F. Dickinson. "Error, reproducibility and uncertainty in experiments for electrochemical energy technologies". In: *Nature Communications* 13 (2022), p. 6832.
- [85] Yu Bi. "Two-dimensional Cu-based Metal–Organic Frameworks as electrochemical catalysts for CO₂ reduction". PhD thesis. 2022.
- [86] Neeraj Kumar Bhoi, Harpreet Singh, and Saurabh Pratap. "Chapter 1 - Futuristic synthesis strategies for aluminum-based metal-matrix composites". In: *Composite Materials*. Ed. by It-Meng Low and Yu Dong. Elsevier, 2021, pp. 3–23.
- [87] Masao Tokita. "Chapter 11.2.3 - Spark Plasma Sintering (SPS) Method, Systems, and Applications". In: *Handbook of Advanced Ceramics (Second Edition)*. Ed. by Shigeyuki Somiya. Second Edition. Oxford: Academic Press, 2013, pp. 1149–1177.
- [88] N. Sharma, S. N. Alam, and B. C. Ray. "Fundamentals of Spark Plasma Sintering (SPS): An Ideal Processing Technique for Fabrication of Metal Matrix Nanocomposites". In: *Spark Plasma Sintering of Materials: Advances in Processing and Applications*. Ed. by Pasquale Cavaliere. Cham: Springer International Publishing, 2019, pp. 21–59.
- [89] Jun Cheng, Xiaoxu Xuan, Xiao Yang, Junhu Zhou, and Kefa Cen. "Selective reduction of CO₂ to alcohol products on octahedral catalyst of carbonized Cu(BTC) doped with Pd nanoparticles in a photoelectrochemical cell". In: *Chemical Engineering Journal* 358 (2019), pp. 860–868.

- [90] S. Najafi Nobar. "Cu-BTC synthesis, characterization and preparation for adsorption studies". In: *Materials Chemistry and Physics* 213 (2018), pp. 343–351.
- [91] *Cu-THQ*. URL: <https://www.cd-bioparticles.net/p/8958/cu-thq> (visited on 01/11/2023).
- [92] Dawei Feng, Ting Lei, Maria Lukatskaya, Jihye Park, Zhehao Huang, Minah Lee, Leo Shaw, Shucheng Chen, Andrey Yakovenko, Ambarish Kulkarni, Jianping Xiao, Kurt Fredrickson, Jeffrey Tok, Xiaodong Zou, Yi Cui, and Zhenan Bao. "Robust and conductive two-dimensional metal–organic frameworks with exceptionally high volumetric and areal capacitance". In: *Nature Energy* 3 (Jan. 2018).
- [93] Dawei Feng, Ting Lei, Maria Lukatskaya, Jihye Park, Zhehao Huang, Minah Lee, Leo Shaw, Shucheng Chen, Andrey Yakovenko, Ambarish Kulkarni, Jianping Xiao, Kurt Fredrickson, Jeffrey Tok, Xiaodong Zou, Yi Cui, and Zhenan Bao. "Robust and conductive two-dimensional metal–organic frameworks with exceptionally high volumetric and areal capacitance". In: *Nature Energy* 3 (Jan. 2018).
- [94] Sina Ebnesajjad. "4 - Surface and Material Characterization Techniques". In: *Handbook of Adhesives and Surface Preparation*. Ed. by Sina Ebnesajjad. Plastics Design Library. Oxford: William Andrew Publishing, 2011, pp. 31–48.
- [95] *Thermal gravimetric analysis*. 2023. URL: <https://www.tue.nl/en/research/research-groups/transport-in-permeable-media/our-facilities/thermal-gravimetric-analysis/#top> (visited on 01/11/2023).
- [96] Peiqiang Cui, Shaopeng Wu, Fuzhou Li, Yue Xiao, and Honghua Zhang. "Investigation on Using SBS and Active Carbon Filler to Reduce the VOC Emission from Bituminous Materials". In: *Materials* 7 (Sept. 2014), pp. 6130–6143.
- [97] Jürgen H. Gross. *Mass spectrometry: A textbook*. 3rd ed. Springer, 2017.
- [98] Peiqiang Cui, Shaopeng Wu, Fuzhou Li, Yue Xiao, and Honghua Zhang. "Investigation on Using SBS and Active Carbon Filler to Reduce the VOC Emission from Bituminous Materials". In: *Materials* 7 (Sept. 2014), pp. 6130–6143.
- [99] D.C. Joy, Brian J. Ford, and Savile Bradbury. *scanning electron microscope*. *Encyclopedia Britannica*. Oct. 2022. URL: <https://www.britannica.com/technology/scanning-electron-microscope> (visited on 01/10/2023).
- [100] K. Akhtar, S. A. Khan, S. B. Khan, and A. M. Asiri. "Scanning Electron Microscopy: Principle and Applications in Nanomaterials Characterization". In: *Handbook of Materials Characterization*. SPRINGER, 2019, pp. 113–146.
- [101] *Energy dispersive X-ray spectroscopy (EDS)*. 2020. URL: <https://www.mee-inc.com/hamm/energy-dispersive-x-ray-spectroscopyeds/> (visited on 01/10/2023).
- [102] *Energy-dispersive spectroscopy (EDS)*. URL: <https://maf.stanford.edu/applications/energy-dispersive-spectroscopy-eds> (visited on 01/10/2023).

- [103] Peter Lobaccaro, Meenesh R. Singh, Ezra Lee Clark, Youngkook Kwon, Alexis T. Bell, and Joel W. Ager. "Effects of temperature and gas–liquid mass transfer on the operation of small electrochemical cells for the quantitative evaluation of CO₂ reduction electrocatalysts". In: *Phys. Chem. Chem. Phys.* 18 (38 2016), pp. 26777–26785.
- [104] Noémie Elgrishi, Kelley J. Rountree, Brian D. McCarthy, Eric S. Rountree, Thomas T. Eisenhart, and Jillian L. Dempsey. "A Practical Beginner's Guide to Cyclic Voltammetry". In: *Journal of Chemical Education* 95.2 (2018), pp. 197–206.
- [105] David Harvey. *25.3: Linear Sweep Voltammetry*. Oct. 2022.
- [106] Hend S. Magar, Rabeay Y. A. Hassan, and Ashok Mulchandani. "Electrochemical Impedance Spectroscopy (EIS): Principles, Construction, and Biosensing Applications". In: *Sensors* 21.19 (2021).
- [107] Shashi Bhushan Arya and Fredy James Joseph. "Chapter 3 - Electrochemical methods in tribocorrosion". In: *Tribocorrosion*. Ed. by Arpith Siddaiah, Rahul Ramachandran, and Pradeep L. Menezes. Academic Press, 2021, pp. 43–77.
- [108] Bhavik A. Patel. "Chapter 2 - Amperometry and potential step techniques". In: *Electrochemistry for Bioanalysis*. Ed. by Bhavik Patel. Elsevier, 2020, pp. 9–26.
- [109] Michael Schatz, Sven Jovanovic, Rüdiger-A Eichel, and Josef Granwehr. "Quantifying Local pH Changes in Carbonate Electrolyte during Copper-Catalysed CO₂ Electroreduction Using In Operando ¹³C NMR". In: *Scientific Reports* 12 (1 Feb. 2022), pp. 2045–2322.
- [110] Harold Monroe McNair. "Introduction". In: *Basic gas chromatography*. 3rd ed. Wiley, 2019, pp. 1–14.
- [111] James M. Miller. *Chromatography: Concepts and contrasts*. 2nd ed. Wiley, 2009.
- [112] Kevin Robards and Danielle Ryan. "Chapter 5 - High performance liquid chromatography: Instrumentation and techniques". In: *Principles and Practice of Modern Chromatographic Methods (Second Edition)*. Ed. by Kevin Robards and Danielle Ryan. Second Edition. Academic Press, 2022, pp. 247–282.
- [113] Carl Brännhammar. *What are the limitations of HPLC?* Jan. 2023. URL: <https://labioanalytics.com/what-are-the-limitations-of-hplc/> (visited on 01/13/2023).
- [114] Y. V. Timchenko. "Advantages and Disadvantages of High-Performance Liquid Chromatography (HPCL)". In: *Journal of Environmental Analytical Chemistry* 8 (10 2021), p. 335.
- [115] Lisha Jia, Klaudia Wagner, Jamie Smyth, David Officer, Jun Chen, and Pawel Wagner. "Cu-THQ-EFG Composite for Highly Selective Electrochemical CO₂ Reduction to Formate at Low Overpotentials". In: *Polymers* 14.23 (2022).
- [116] Ugur Ulusoy. "A Review of Particle Shape Effects on Material Properties for Various Engineering Applications: From Macro to Nanoscale". In: *Minerals* 13.1 (2023).

- [117] Michele Melchionna, Paolo Fornasiero, and Matteo Cargnello. "Chapter 1 - Opportunities and Challenges in the Synthesis, Characterization, and Catalytic Properties of Controlled Nanostructures". In: *Morphological, Compositional, and Shape Control of Materials for Catalysis*. Ed. by Paolo Fornasiero and Matteo Cargnello. Vol. 177. Studies in Surface Science and Catalysis. Elsevier, 2017, pp. 1–56.
- [118] J Qiao, Y Liu, and J. Zhang. *Electrochemical reduction of carbon dioxide : Fundamentals and technologies*. 1st ed. Vol. 11. Taylor & Francis Group, 2016, pp. 281–302.
- [119] Jing Lin, Shenglin Yan, Chunxiao Zhang, Qing Hu, and Zhenmin Cheng. "Electroreduction of CO₂ toward High Current Density". In: *Processes* 10.5 (2022).
- [120] Mohamed Mamlouk. "4.19 - Alkaline Anion Exchange Membrane (AEM) Water Electrolysers—Current/Future Perspectives in Electrolysers for Hydrogen". In: *Comprehensive Renewable Energy (Second Edition)*. Ed. by Trevor M. Letcher. Second Edition. Oxford: Elsevier, 2022, pp. 473–504.
- [121] "A flexible carbon counter electrode for dye-sensitized solar cells". In: *Carbon* 47.11 (2009), pp. 2704–2708.
- [122] Ferry Iskandar, Oktaviardi Bityasmawan Abdillah, Erythrina Stavila, and Akfiny Hasdi Aimon. "The influence of copper addition on the electrical conductivity and charge transfer resistance of reduced graphene oxide (rGO)". In: *New J. Chem.* 42 (19 2018), pp. 16362–16371.
- [123] R. Senthil Kumar, S. Senthil Kumar, and M. Anbu Kulandainathan. "Highly selective electrochemical reduction of carbon dioxide using Cu based metal organic framework as an electrocatalyst". In: *Electrochemistry Communications* 25 (2012), pp. 70–73.
- [124] Kendra P. Kuhl, Etosha R. Cave, David N. Abram, and Thomas F. Jaramillo. "New insights into the electrochemical reduction of carbon dioxide on metallic copper surfaces". In: *Energy Environ. Sci.* 5 (5 2012), pp. 7050–7059.
- [125] Mun Kyoung Kim, Hyeok Joo Kim, Hyungseob Lim, Youngkook Kwon, and Hyung Mo Jeong. "Metal–organic framework-mediated strategy for enhanced methane production on copper nanoparticles in electrochemical CO₂ reduction". In: *Electrochimica Acta* 306 (2019), pp. 28–34.
- [126] L. C. Grabow and M. Mavrikakis. "Mechanism of Methanol Synthesis on Cu through CO₂ and CO Hydrogenation". In: *ACS Catalysis* 1.4 (2011), pp. 365–384.
- [127] Feng Jiang, Shanshan Wang, Bing Liu, Jie Liu, Li Wang, Yang Xiao, Yuebing Xu, and Xiaohao Liu. "Insights into the Influence of CeO₂ Crystal Facet on CO₂ Hydrogenation to Methanol over Pd/CeO₂ Catalysts". In: *ACS Catalysis* 10.19 (2020), pp. 11493–11509.
- [128] Feng Jiang, Yu Yang, Li Wang, Yufeng Li, Zhihao Fang, Yuebing Xu, Bing Liu, and Xiaohao Liu. "Dependence of copper particle size and interface on methanol and CO formation in CO₂ hydrogenation over Cu@ZnO catalysts". In: *Catal. Sci. Technol.* 12 (2 2022), pp. 551–564.

- [129] Zixu Tao, Zishan Wu, Yueshen Wu, and Hailiang Wang. “Activating Copper for Electrocatalytic CO₂ Reduction to Formate via Molecular Interactions”. In: *ACS Catalysis* 10.16 (2020), pp. 9271–9275.
- [130] Jing-Jing Wang, Hong-Juan Wang, Chao Zhang, Yun-Nan Gong, Ya-Li Bai, and Tong-Bu Lu. “Graphdiyne enables Cu nanoparticles for highly selective electroreduction of CO₂ to formate”. In: *2D Materials* 8 (Oct. 2021), p. 044008.
- [131] Dae-Hyun Nam, Osama Shekhah, Adnan Ozden, Christopher McCallum, Feng-wang Li, Xue Wang, Yanwei Lum, Taemin Lee, Jun Li, Joshua Wicks, Andrew Johnston, David Sinton, Mohamed Eddaoudi, and Edward H. Sargent. “High-Rate and Selective CO₂ Electrolysis to Ethylene via Metal–Organic-Framework-Augmented CO₂ Availability”. In: *Advanced Materials* 34.51 (2022), p. 2207088.
- [132] Yan-Ling Qiu, He-Xiang Zhong, Tao-Tao Zhang, Wen-Bin Xu, Pan-Pan Su, Xian-Feng Li, and Hua-Min Zhang. “Selective Electrochemical Reduction of Carbon Dioxide Using Cu Based Metal Organic Framework for CO₂ Capture”. In: *ACS Applied Materials & Interfaces* 10.3 (2018), pp. 2480–2489.
- [133] Nivedita Sikdar, João R. C. Junqueira, Stefan Dieckhöfer, Thomas Quast, Michael Braun, Yanfang Song, Harshitha B. Aiyappa, Sabine Seisel, Jonas Weidner, Denis Öhl, Corina Andronesco, and Wolfgang Schuhmann. “A Metal–Organic Framework derived Cu_xO_yC_z Catalyst for Electrochemical CO₂ Reduction and Impact of Local pH Change”. In: *Angewandte Chemie International Edition* 60.43 (2021), pp. 23427–23434.